

AD-A092 420

AIR FORCE INST OF TECH WRIGHT-PATTERSON AFB OH

F/G 4/2

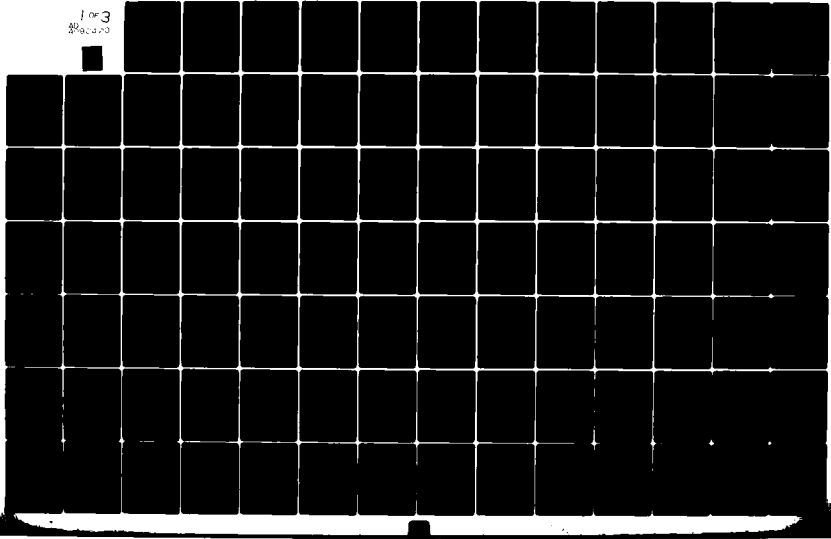
DYNAMIC INTERACTIONS BETWEEN THE TROPOSPHERE AND STRATOSPHERE. (U)

1980 J P KOERMER

UNCLASSIFIED AFIT-CI-80-310

for 3
209020

NL



BUC FILE COPY, AD A092420

UNCLASS

SECURITY CLASSIFICATION OF THIS PAGE (When Data Entered)

LEVEL II

REPORT DOCUMENTATION PAGE			READ INSTRUCTIONS BEFORE COMPLETING FORM
1. REPORT NUMBER I-80-31D	2. GOVT ACCESSION NO. AD-A092 430	3. RECIPIENT'S CATALOG NUMBER	
4. TITLE (and Subtitle) Dynamic Interactions Between the Troposphere and Stratosphere		5. TYPE OF REPORT & PERIOD COVERED THESIS/DISSERTATION	
6. PERFORMING ORG. REPORT NUMBER James Paul Koerner		7. CONTRACT OR GRANT NUMBER(s) H-319	
8. PERFORMING ORGANIZATION NAME AND ADDRESS AFIT STUDENT AT: The University of Utah		9. PROGRAM ELEMENT PROJECT, TASK AREA & WORK UNIT NUMBERS	
10. CONTROLLING OFFICE NAME AND ADDRESS AFIT/NR WPAFB OH 45433		11. REPORT DATE 1980	
12. MONITORING AGENCY NAME & ADDRESS (if different from Controlling Office)		13. NUMBER OF PAGES 180	
14. SECURITY CLASS. (of this report) UNCLASS		15. DECLASSIFICATION DOWNGRADING SCHEDULE S E	
16. DISTRIBUTION STATEMENT (of this Report) APPROVED FOR PUBLIC RELEASE; DISTRIBUTION UNLIMITED			
17. DISTRIBUTION STATEMENT (of the abstract entered in Block 20, if different from Report) DEC 04 1980			
18. SUPPLEMENTARY NOTES APPROVED FOR PUBLIC RELEASE: IAW AFR 190-17 FREDRIC C. LYNCH, Major, USAF Director of Public Affairs			
19. KEY WORDS (Continue on reverse side if necessary and identify by block number)			
20. ABSTRACT (Continue on reverse side if necessary and identify by block number) ATTACHED			

DD FORM 1 JAN 73 EDITION OF 1 NOV 65 IS OBSOLETE

UNCLASS

SECURITY CLASSIFICATION OF THIS PAGE (When Data Entered)

80 11 24 126

1, C 1

DYNAMIC INTERACTIONS BETWEEN THE TROPOSPHERE
AND STRATOSPHERE

by

James Paul Koerner

An abstract of a dissertation submitted to the faculty of The
University of Utah in partial fulfillment of the requirements
for the degree of

Doctor of Philosophy

Shih-Kung Kao

Chairman, Supervisory Committee

Professor of Meteorology

Department of Meteorology

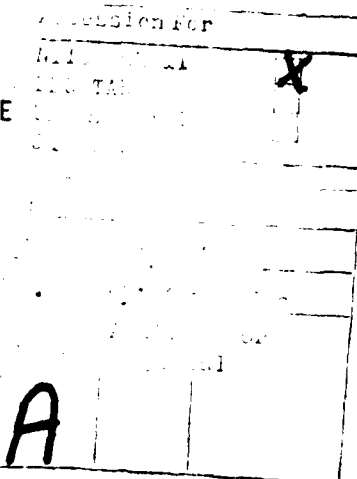
The University of Utah

August 1980

DYNAMIC INTERACTIONS BETWEEN THE TROPOSPHERE
AND STRATOSPHERE

by

James Paul Koerner



An abstract of a dissertation submitted to the faculty of The
University of Utah in partial fulfillment of the requirements
for the degree of

Doctor of Philosophy

Shih-Kung Kao

Chairman, Supervisory Committee

Professor of Meteorology

Department of Meteorology

The University of Utah

August 1980

AFIT RESEARCH ASSESSMENT

The purpose of this questionnaire is to ascertain the value and/or contribution of research accomplished by students or faculty of the Air Force Institute of Technology (ATC). It would be greatly appreciated if you would complete the following questionnaire and return it to:

AFIT/NR
Wright-Patterson AFB OH 45433

Research Title: Dynamic Interactions Between the Troposphere and Stratosphere

Author: James Paul Koermer

Research Assessment Questions:

1. Did this research contribute to a current Air Force project?

2. Do you believe this research topic is significant enough that it would have been researched (or contracted) by your organization or another agency if AFIT had not?

3. The benefits of AFIT research can often be expressed by the equivalent value that your agency achieved/received by virtue of AFIT performing the research. Can you estimate what this research would have cost if it had been accomplished under contract or if it had been done in-house in terms of manpower and/or dollars?

a. Man-years . b. \$

4. Often it is not possible to attach equivalent dollar values to research, although the results of the research may, in fact, be important. Whether or not you were able to establish an equivalent value for this research (3 above), what is your estimate of its significance?

2. Highly Significant b. Significant c. Slightly Significant d. Of No Significance

5. AFIT welcomes any further comments you may have on the above questions, or any additional details concerning the current application, future potential, or other value of this research. Please use the back of this questionnaire for your statement(s).

NAME **GRADE** **POSITION**

ORGANIZATION **LOCATION**

USAF SCN 75-20B

Copyright © James Paul Koerner 1980
All Rights Reserved

THE UNIVERSITY OF UTAH GRADUATE SCHOOL

SUPERVISORY COMMITTEE APPROVAL

of a dissertation submitted by

JAMES PAUL KOERMER

I have read this dissertation and have found it to be of satisfactory quality for a doctoral degree.

June 20, 1980
Date

S. K. Kao
S. K. Kao
Chairman, Supervisory Committee

I have read this dissertation and have found it to be of satisfactory quality for a doctoral degree.

June 20, 1980
Date

Norihiro Fukuta
Norihiro Fukuta
Member, Supervisory Committee

I have read this dissertation and have found it to be of satisfactory quality for a doctoral degree.

June 20, 1980
Date

Jan Paegle
Jan Paegle
Member, Supervisory Committee

I have read this dissertation and have found it to be of satisfactory quality for a doctoral degree.

June 20, 1980
Date

Robert E. Stephenson
Robert E. Stephenson
Member, Supervisory Committee

I have read this dissertation and have found it to be of satisfactory quality for a doctoral degree.

June 20, 1980
Date

Akira Kasahara
Akira Kasahara
Member, Supervisory Committee

THE UNIVERSITY OF UTAH GRADUATE SCHOOL

FINAL READING APPROVAL

To the Graduate Council of The University of Utah:

I have read the dissertation of JAMES PAUL KOERMER in its final form and have found that (1) its format, citations, and bibliographic style are consistent and acceptable; (2) its illustrative materials including figures, tables, and charts are in place; and (3) the final manuscript is satisfactory to the Supervisory Committee and is ready for submission to the Graduate School.

Date

June 20, 1980

S. K. Kao

Member, Supervisory Committee

Approved for the Major Department

S. K. Kao

S. K. Kao

Chairman Dean

Approved for the Graduate Council

James L. Clayton
Dean of The Graduate School

REFERENCES

Arakawa, A., and V. R. Lamb, Computational design of the basic dynamical processes of the UCLA general circulation model, Methods in Comp. Phys., 17, 173-265 (1977).

Bourke, W., A multi-level spectral model. I. Formulation and hemispheric integrations, Mon. Wea. Rev., 102, 687-701 (1974).

Bourke, W., B. McAvaney, K. Puri, and R. Thuring, Global modeling of the atmospheric flow by spectral methods, Methods in Comp. Phys., 17, 267-334 (1977).

Charney, J. G., and P. G. Drazin, Propagation of planetary scale disturbances from the lower into the upper atmosphere, J. Geophys. Res., 66, 83-109 (1961).

Corby, G. A., A Gilchrist, and R. Newson, A general circulation model of the atmosphere, suitable for long period integrations, Quart. J. R. Meteorol. Soc., 98, 809-832 (1972).

Craig, R. A., The Upper Atmosphere, Meteorology and Physics (Academic Press, New York, 1965).

Eliassen, A., and E. Palm, On the transfer of energy in stationary mountain waves, Geofysiske Publikasjoner, 12, No. 3, 1-23 (1961).

Haltiner, G. J., Numerical Weather Prediction (John Wiley and Sons, New York, 1971).

Hirota, I., Planetary waves in the upper stratosphere in early 1966, J. Meteorol. Soc. Jap. 6, 418-430 (1968).

Hirota, I., and J. J. Barnett, Planetary waves in the winter mesosphere --Preliminary analysis of Nimbus 6 PMR results, Quart. J. Roy. Meteorol. Soc., 103, 487-498 (1977).

Holton, J. R., The dynamic meteorology of the stratosphere and mesosphere, Meteorol. Mon., No. 37 (1975), 218 pp.

Holton, J. R., A semi-spectral numerical model for wave-mean flow interactions in the stratosphere: application to sudden stratospheric warmings. J. Atmos. Sci., 33, 1639-1649 (1976).

Holton, J. R. and C. Mass, Stratospheric vacillation cycles, J. Atmos. Sci., 33, 2218-2225 (1976).

ABSTRACT

A primitive equation spectral model using spherical harmonics is formulated to study interactions between the troposphere and stratosphere in association with sudden stratospheric warmings. In order to follow vertical wave propagation so important to this process, the model consists of 31 levels with 5 in the troposphere and the other 26 in the stratosphere and mesosphere. Using sigma coordinates for the former and log-pressure coordinates for the latter, separate equations for each system are combined to form single matrix governing equations. The gradual introduction of planetary scale topography to an initially balanced state representative of observed mean winter conditions in the Northern Hemisphere is used to force changes in the initial fields during 40 day time integrations. Utilizing the same initial tropospheric conditions, three cases were run. The first case started with a weak polar night jet in the stratosphere and mesosphere. The second case had a much stronger polar vortex. For the third case, a lid was placed on the troposphere and no interaction was allowed with the atmosphere at higher levels.

Results of these integrations indicate that realistic stratospheric warmings can be simulated by simple orographic forcing; that the strength of the polar night jet can be a determining factor in whether a warming becomes "major" or "minor"; that the stratosphere plays an important role in tropospheric wave evolution; that the indirect cell mechanism is fundamental to the warming process; that

large terms in the momentum and heat budgets tend to cancel, but significant changes in the zonal wind and temperature do occur if there is a slight imbalance between these terms; and that wave to wave interactions are an essential part of sudden stratospheric warmings.

TABLE OF CONTENTS

ABSTRACT	iv
LIST OF FIGURES	ix
ACKNOWLEDGEMENTS	xiv
1. INTRODUCTION	1
2. MODEL FORMULATION	13
2.1 Vertical Coordinate Systems	13
2.2 Governing Equations	15
2.2.1 Vorticity equations	16
2.2.2 Divergent equation	19
2.2.3 Frictional force	21
2.2.4 Vertical velocity expressions	22
2.2.5 Thermodynamic equation	25
2.2.6 Continuity equation	29
2.2.7 Hydrostatic equation	31
2.3 Vertical Differencing	32
2.3.1 Mass conservation	34
2.3.2 Conservation of total energy	35
2.4 Semi-implicit Time Differencing Preliminaries	41
2.5 Spherical Harmonic Representation	50
2.6 Conclusion of Semi-implicit Differencing	53
2.7 Modified Euler Backward Scheme	56

3. SPECIFICATION	57
3.1 Model Initialization	57
3.2 Orographic Forcing	63
3.3 Convective Adjustment	65
3.4 Spectral Truncation and Horizontal Diffusion	68
3.5 Momentum Budget	70
3.6 Heat Budget	71
4. MODEL RESULTS	73
4.1 C1 Results	74
4.1.1 Evolution of zonal mean velocity, temperature, and geopotential	74
4.1.2 Horizontal evolution of geopotential, temperature, and tropospheric jets	79
4.1.3 Evolutions of zonal mean velocity components, temperature, geopotential, and momentum and heat budgets at 68.9 N	81
4.1.4 Evolutions of zonal mean velocities, temperature, geopotential, and momentum and heat budgets at various heights	86
4.2 Case 2 Results	89
4.2.1 Evolution of zonal mean velocity, temperature, and geopotential	89
4.2.2 Horizontal evolution of geopotential, temperature, and tropospheric jet	93
4.2.3 Evolutions of zonal mean velocity components, temperature, geopotential, and momentum and heat budgets at 68.9 N	94
4.2.4 Evolutions of zonal mean velocities, temperature, geopotential, and momentum and heat budgets at various heights	99
4.3 Case 3 Results	103

5. CONCLUSION	106
FIGURES	111
REFERENCES	175
VITA	180

LIST OF FIGURES

Figure 1. Model Schematic. Dashed/solid lines represent prognostic/diagnostic levels respectively. Boundary conditions are specified at top and bottom boundaries 111

Figure 2. Latitude-height sections of initial mean zonal wind ($\times 10 \text{ m s}^{-1}$) for (a) Case 1; and (b) Case 2 112

Figure 3. Latitude-height sections of the initial zonal mean temperature deviations ($\times 10^\circ\text{K}$) for (a) Case 1; and (b) Case 2 113

Figure 4. Maximum longitudinal surface height distribution at 45°N 114

Figure 5. Latitude-height sections of the mean zonal wind ($\times 10 \text{ m s}^{-1}$) for C1 on (a) day 10; (b) day 20; (c) day 30; and (d) day 40 115

Figure 6. Same as Fig. 5 except on (a) day 22; (b) day 24; (c) day 26; and (d) day 28 116

Figure 7. Latitude-height sections of zonal mean temperature deviations ($\times 10^\circ\text{K}$) for C1 on (a) day 10; (b) day 20; (c) day 30; and (d) day 40 117

Figure 8. Same as Fig. 7 except on (a) day 22; (b) day 24; (c) day 26; and (d) day 28 118

Figure 9. C1 latitude-height sections of $|\phi_1|$ ($\times 10^2 \text{ m}^2 \text{ s}^{-2}$) indicated by solid lines (except for $|\phi_1| = 100$ represented by long dashed lines) with the ϕ phase angle (radians) indicated by short dashed lines for (a) day 10; (b) day 20; (c) day 30; and (d) day 40 . 119

Figure 10. Same as Fig. 9 except for ϕ_2 120

Figure 11. Polar stereographic projections of height deviations ($\times 10^2 \text{ m}$) at 40.5 km for C1 on (a) day 10; (b) day 20; (c) day 30; and (d) day 40 121

Figure 12. Same as Fig. 11 except at approximately 6.7 km . . . 122

Figure 13. Polar stereographic projections of temperature deviations ($^{\circ}$ K) at 40.5 km for C1 on (a) day 10; (b) day 20; (c) day 30; and (d) day 40	123
Figure 14. Same as Fig. 13 except at approximately 6.7 km	124
Figure 15. C1 polar stereographic projections of the zonal wind component ($m s^{-1}$) for values greater than or equal to $20 m s^{-1}$ on (a) day 10; (b) day 20; (c) day 30; and (d) day 40	125
Figure 16. C1 height-time sections at 68.9 N of (a) mean zonal wind ($m s^{-1}$); (b) zonal mean meridional velocity component ($m s^{-1}$); (c) zonal mean vertical velocity ($\times 10^{-1} m s^{-1}$); and (d) zonal mean temperature deviation ($^{\circ}$ K)	126
Figure 17. C1 height-time sections at 68.9 N of (a) $ \phi_1 $; (b) $ \phi_2 $; (c) $ \phi_3 $; and (d) $ \phi_4 $. Units are $10^3 m^2 s^{-2}$	127
Figure 18. C1 height-time sections of (a) $\bar{au}/\partial t$; (b) FM; (c) FC; (d) FB; (e) FA; and (f) FE. Units are $10^{-4} m s^{-2}$	128
Figure 19. C1 height-time sections at 68.9 N of (a) $\bar{\partial T}/\partial t$; (b) VTP; (c) HWB; (d) VTB; (e) WTB; (f) WTP; and (g) HNA. Units are $10^{-4} ^{\circ}K s^{-1}$	130
Figure 20. C1 latitude-time section of mean zonal wind ($m s^{-1}$) at (a) 7.5 km; (b) 40.5 km; and (c) 67.5 km	132
Figure 21. C1 latitude-time sections at 40.5 km of (a) the zonal mean meridional velocity component ($m s^{-1}$) and (b) the zonal mean vertical velocity ($\times 10^{-1} m s^{-1}$)	133
Figure 22. C1 latitude-time sections of zonal mean temperature deviation ($^{\circ}$ K) at (a) 7.5 km; (b) 40.5 km; and (c) 67.5 km	134
Figure 23. C1 latitude-time section of $ \phi_1 $ ($\times 10^3 m^2 s^{-2}$) at (a) 7.5 km; (b) 40.5 km; and (c) 67.5 km	135
Figure 24. Same as Fig. 23 except for $ \phi_2 $	136
Figure 25. Same as Fig. 23 except for $ \phi_3 $	137
Figure 26. Same as Fig. 23 except for $ \phi_4 $	138

Figure 27. C1 latitude-time sections at 40.5 km of (a) $\partial u / \partial t$; (b) FM; (c) FC; (d) FB; (e) FA; and (f) FE. Units are 10^{-4} m s^{-2}	139
Figure 28. C1 latitude-time section at 40.5 km of (a) $\partial \bar{T} / \partial t$; (b) VTP; (c) HWB; (d) VTB; (e) WTB; (f) WTP; and (g) HNA. Units are $10^{-4} \text{ }^{\circ}\text{K s}^{-1}$	141
Figure 29. Latitude-height sections of the mean zonal wind ($\times 10 \text{ m s}^{-1}$) for C2 on (a) day 10; (b) day 20; (c) day 30; (d) day 40	143
Figure 30. Same as Fig. 29 except on (a) day 32; (b) day 34; (c) day 36; and (d) day 38	144
Figure 31. Latitude-height sections of zonal mean temperature deviation ($\times 10^{\circ}\text{K}$) for C2 on (a) day 10; (b) day 20; (c) day 30; and (d) day 40	145
Figure 32. Same as Fig. 31 except on (a) day 32; (b) day 34; (c) day 36; and (d) day 40	146
Figure 33. C2 latitude-height sections of $ \phi_1 $ ($\times 10^2 \text{ m}^2 \text{ s}^{-2}$) indicated by solid lines (except for $ \phi_1 = 100$ represented by long dashed lines) with the ϕ_1 phase angle (radians) indicated by short dashed lines for (a) day 10; (b) day 20; (c) day 30; and (d) day 40	147
Figure 34. Same as Fig. 33 except for ϕ_2	148
Figure 35. Polar stereographic projections of height deviations ($\times 10^2 \text{ m}$) at 40.5 km for C2 on (a) day 10; (b) day 20; (c) day 30; and (d) day 40	149
Figure 36. Polar stereographic projections of height deviations ($\times 10^2 \text{ m}$) for C2 at approximately 6.7 km on (a) day 30 and (b) day 40; and at 13.5 km on (c) day 34 and (d) day 38	150
Figure 37. Polar stereographic projections of temperature deviations ($^{\circ}\text{K}$) at 40.5 km on (a) day 30 and (b) day 40; and at approximately 6.7 km on (c) day 30 and (d) day 40	151
Figure 38. C2 height-time sections at 68.9 N of (a) mean zonal wind (m s^{-1}); (b) zonal mean meridional velocity component (m s^{-1}); (c) zonal mean vertical velocity ($\times 10^{-1} \text{ m s}^{-1}$); and (d) zonal mean temperature deviation ($^{\circ}\text{K}$)	152

Figure 39. C2 height-time sections at 68.9 N of (a) $ \phi_1 $; (b) $ \phi_2 $; (c) $ \phi_3 $; and (d) $ \phi_4 $. Units are $10^3 \text{ m}^2 \text{s}^{-2}$	153
Figure 40. C2 height-time sections at 68.9 N of (a) $\bar{u}/\partial t$; (b) FM; (c) FC; (d) FB; (e) FA; and (f) FE. Units are 10^{-4} m s^{-2}	154
Figure 41. C2 height-time sections at 68.9 N of (a) $\bar{\partial T}/\partial t$; (b) VTP; (c) HWB; (d) VTB; (e) WTB; (f) WTP; and (g) HNA. Units are $10^{-4} \text{ }^{\circ}\text{K s}^{-1}$	156
Figure 42. C2 latitude-time sections of mean zonal wind (m s^{-1}) at (a) 7.5 km; (b) 40.5 km; and (c) 67.5 km	158
Figure 43. C2 latitude-time sections at 40.5 km of (a) the zonal mean meridional velocity component (m s^{-1}) and (b) the zonal mean vertical velocity ($\times 10^{-1} \text{ m s}^{-1}$)	159
Figure 44. C2 latitude-time sections of zonal mean temperature deviation ($^{\circ}\text{K}$) at (a) 7.5 km; (b) 40.5 km; and (c) 67.5 km	160
Figure 45. C2 latitude-time sections of $ \phi_1 $ ($\times 10^3 \text{ m}^2 \text{s}^{-2}$) at (a) 7.5 km; (b) 40.5 km; and (c) 67.5 km	161
Figure 46. Same as Fig. 45 except for $ \phi_2 $	162
Figure 47. Same as Fig. 45 except for $ \phi_3 $	163
Figure 48. Same as Fig. 45 except for $ \phi_4 $	164
Figure 49. C2 latitude-time sections at 40.5 km of (a) $\bar{u}/\partial t$; (b) FM; (c) FC; (d) FB; (e) FA; and (f) FE. Units are 10^{-4} m s^{-2}	165
Figure 50. C2 latitude-time sections at 40.5 km of (a) $\bar{\partial T}/\partial t$; (b) VTP; (c) HWB; (d) VTB; (e) WTB; (f) WTP; and (g) HNA. Units are $10^{-4} \text{ }^{\circ}\text{K s}^{-1}$	167
Figure 51. Latitude-height sections of the mean zonal wind (m s^{-1}) for C3 on (a) initial time; (b) day 10; (c) day 20; (d) day 30; and (e) day 40	169
Figure 52. Polar stereographic projections of height deviations ($\times 10^2 \text{ m}$) at approximately 6.7 km for C3 on (a) day 10; (b) day 20; (c) day 30; and (d) day 40	170

Figure 53. Polar stereographic projections of temperature deviations ($^{\circ}$ K) at approximately 6.7 km for C3 on (a) day 10; (b) day 20; (c) day 30; and (d) day 40 171

Figure 54. C3 polar stereographic projections of the zonal wind component ($m s^{-1}$) for values greater than or equal to $20 m s^{-1}$ on (a) day 10; (b) day 20; (c) day 30; (d) day 40 172

Figure 55. C3 latitude-time sections at 7.5 km of (a) mean zonal velocity ($m s^{-1}$) and (b) zonal mean temperature deviation ($^{\circ}$ K) 173

Figure 56. C3 latitude-time sections at 7.5 km of (a) $|\phi_1|$; (b) $|\phi_2|$; (c) $|\phi_3|$; and (d) $|\phi_4|$. Units are $10^3 m^2 s^{-2}$ 174

ACKNOWLEDGEMENTS

I wish to express my sincere gratitude to Dr. Shih-Kung Kao, chairman of my supervisory committee, for his guidance, encouragement, and support during my graduate study. His ideas and expertise were fondly appreciated. His overall direction of my research program from igniting my interest in wave-wave interactions and stratospheric warming phenomena to overseeing the final preparation of this manuscript will always be kindly remembered.

My deepest and heartfelt thanks also go to Dr. Akira Kasahara of the National Center for Atmospheric Research, who devoted so much of his valuable time in guiding me through the most difficult aspects of this research. By providing a wealth of knowledge and experience from which to draw, he made this effort not only possible but also enjoyable. It has truly been a privilege to work so closely with men of such stature as Dr. Kao and Dr. Kasahara and I hope I will be able to do so in the future.

I also am deeply indebted to Drs. Nick Lordi and Jim Hatch, who so graciously passed on many fruits of their own research efforts to me. These gentlemen have so willingly given me their time, advice, and support. Their expertise has saved me an immense amount of time and allowed me to tackle an otherwise impossible research topic.

I also would like to thank Dr. Fukata, Dr. Paegle, and Dr. Stephenson for serving on my supervisory committee. My gratitude is also extended to the Air Force Institute of Technology for providing

me with such a valuable educational opportunity; the Air Force Logistics Command for providing computer support at Hill Air Force Base during the early stages of my research; and the National Center for Atmospheric Research, which is sponsored by the National Science Foundation, for providing an unbelievable computer capability and for the use of their facilities during my extended visits there. Part of this research was supported by the National Aeronautics and Space Administration under contract No. NAS5-25373.

Finally, I wish to express my love for my wife, Joanne, and four children, Janice, Jimmy, Jeanne, and Jenny, for persevering, understanding, and supporting me during my graduate study and tolerating the family disruptions that resulted from my frequent and extended absences from home. Despite the separations, I thank God that we not only survived, but also in many ways became closer. I dedicate this effort to my loving family with deepest love and appreciation.

CHAPTER 1

INTRODUCTION

Since the discovery of the sudden stratospheric warming by Scherhag (1952), this remarkable phenomenon has been the focal point of numerous observational studies and more recently the objective of several modeling efforts. Although our understanding of these warming occurrences has been greatly improved by these research efforts, many questions still remain unanswered. This is particularly true of the nature of interactions between the troposphere and stratosphere in connection with these warming regimes. The purpose of this thesis is to explore this area through numerical simulation with a sophisticated prognostic model particularly well suited for studying these processes.

Sudden stratospheric warnings are characterized by rapid polar temperature increases, sometimes exceeding 50°K (within a deep stratospheric level over the period of one week (McIntruff, 1978). Warmings have been classified by the World Meteorological Organization (WMO) in two categories. The warming classification is major if the temperature gradient and mean zonal wind direction reverses poleward of 60° latitude. A minor warming is one characterized by a large temperature increase anywhere in the stratosphere with the change occurring over a short period, but not meeting the conditions of a major warming. A major warming is a sporadic phenomenon that occurs about once every other year. Minor warmings occur more frequently with sometimes as

many as three during a winter season (Schoeberl, 1978).

In absence of warming activity, the winter stratosphere has a relatively large meridional temperature gradient with cold polar temperatures due to decreasing ozone absorption of solar radiation during the long polar night (Schoeberl, 1978). As a result, strong westerlies develop in response to the thermal wind relationship and form a cyclonic vortex around the pole. The core of these westerlies is known as the polar night jet. The jet maximum lies near the stratopause and is actually located in middle latitudes further south than the boundary of the polar night (Craig, 1965). At lower levels, the jet extends northward down to the tropopause. During sudden warmings, the polar night jet undergoes tremendous upheaval and, as in the case of major warming, is replaced by easterlies over much of the polar stratosphere. In some instances, as the major warming of 1976-1977 (Taylor and Perry, 1977; Quiroz, 1977), the warming and wind reversal may extend all the way to the surface through the entire troposphere.

Teweles and Finger (1958) first began to recognize from the 1957-1958 major warming that planetary scale waves played an important role in the warming process. This has been verified by nearly every observational study since then. Charney and Drazin (1961) presented the theoretical evidence that the only vertical propagating waves that can penetrate the stratosphere from the troposphere are those whose phase speeds are westward relative to the mean zonal wind, but less than a critical velocity inversely proportional to wavelength. The planetary

waves, those with zonal wavenumbers 1-4, are usually the only waves that meet this criterion and then only during the winter months when the upper atmospheric flow is westerly. Stratospheric easterly flow, as in the summer months and as may develop after a strong warming, tends to trap most wave activity in the troposphere. According to Houghton (1978), if this upward propagation of wave energy is prevented, radiative processes prevail. After a major warming, this means a re-intensification of the polar night jet.

Of the planetary waves, wave 1 has the easiest time of penetrating the winter stratosphere, followed by wave 2. Waves 3 and 4 have a much more difficult time propagating upward into the stratosphere, but according to Perry (1967), wave 3 does grow in the stratosphere from non-linear interactions probably involving waves 1 and 2. Stratospheric warmings and their associated planetary wave activity have been attributed to radiation effects, instability, and/or forcing from below (Trenberth, 1973). However, all but the latter appear to be insufficient to cause the large changes in such a short time scale as with the observed warming. McIntyre (1972) essentially disproved the instability as the cause for the stratospheric warmings. Observed changes in radiation during major warming occurrences (Trenberth, 1973) also tend to discount their role in the process. Tropospheric forcing, however, has received support from energetics studies (Julian and Labitzke, 1965; Perry, 1967; Miller and Johnson, 1970; Iwashima, 1974), observational studies (Labitzke, 1977 and 1978; O'Neill and Taylor, 1979), and from numerical simulations (Matsuno, 1971; Holton,

1976; Schoeberl and Strobel, 1980a and 1980b).

Eliassen and Palm (1961) have indicated that flow over mountains produces gravity waves, inertia-gravity waves, and planetary waves. The latter results from flow over ranges continental in scale (e.g. the Rockies). Land masses also radiatively can force large scale wave patterns. Because of the greater topography and nonzonal heat contrasts, the planetary waves 1 and 2 are the most important at mid-latitudes in the Northern Hemisphere (van Loon et al., 1973). On the other hand, quasi-stationary wave 1 and 2 components cannot be readily coupled with orography in mid-latitudes in the Southern Hemisphere, where the surface is essentially oceanic (van Loon and Jenne, 1972). It is interesting to note that a major sudden warming according to WMO standards has never been observed in the Southern Hemisphere (Schoeberl, 1978), which certainly implies the importance of topography in the warming process, but then begs the question why are the phenomena so sporadic in the Northern Hemisphere. Another unanswered question is why pre-1964 major warmings were considered wave 2 occurrences and every warming since then has been predominantly associated with wave 1 (McIntruff, 1978). Perhaps this latter question can be explained away by saying that the data acquisition by satellites and better rocket and balloon observations have given us a more accurate description of the phenomena (Labitzke, 1977), but the doubt will remain unless in the future a strong wave 2 warming does occur. Atmospheric models (e.g. Lordi, 1978) have easily produced wave 2 warmings adding to this doubt. On the other hand, Labitzke (1977, 1978) has tied major warmings directly to wave 1 enhancement with minimal wave 2 activity

and minor warmings with wave 2 enhancement in the troposphere and stratosphere.

The sporadic nature of the warming is also interpreted in several ways. One theory (Iwashima, 1974) is that the standing components of waves 1 and 2 in themselves are not sufficient to produce a warming, but if traveling components come into phase with the quasi-stationary ones an explosive amplification of the wave occurs which propagates rapidly into the stratosphere. Labitzke's (1977) proposal as mentioned above could be another reason for the differences from season to season and warming to warming. Perhaps wave 2 gets amplified more frequently. Another possibility was proposed by Koermer and Kao (1980), where the intensity of the warming was inversely proportional to the strength of the already established polar night jet, which, if not too strong, could reflect wave energy. Finally, another theory comes from Schoeberl and Strobel (1980b), who tie in the orographic forcing with a strong tropospheric jet as a condition to produce a major warming. All of the above conditions are feasible and could occur simultaneously, since they are not contradictory. This shows the need for more research into the tropospheric/stratospheric interaction field in relation to stratospheric warmings.

It is generally accepted that as planetary waves propagate into the stratosphere, they set up an indirect circulation in the polar stratosphere (Matsuno, 1971). As described by O'Neill and Taylor (1979), this circulation consists of air rising near the pole, moving southward near the stratopause, and sinking in mid-latitudes with an

associated poleward heat flux at the bottom of the cell in the lower stratosphere. Meanwhile, a poleward eddy momentum flux develops to counterbalance the coriolis torque acting on the southward movement of air. Matsuno (1971) explained that if there was a sudden amplification of wave 1 or 2, this delicate balance would be destroyed with net heating taking place at the poles because of increased heat flux and the polar night jet would weaken due to increased coriolis torque. Koerner and Kao (1980) compared a major and minor warming and showed significant differences in their heat and momentum budgets, highlighting the importance of this indirect cell in the warming process.

A sudden warming is characterized by a downward propagating warm layer from around 45 km into the lower stratosphere (Quiroz, 1969, 1971) and tends to be highly nonzonal in nature (Hirota, 1968). The magnitude of the effects of the warming process are emphasized by not only a nearly compensating cooling in the mesosphere (Labitzke, 1972; Hirota and Barnett, 1977), but also by a weaker cooling in the lower equatorial stratosphere of about 2° for every 30° to 40° of warming that takes place in polar latitudes (Houghton, 1978). All of these effects make a highly dynamic system out of the stratosphere, which was once believed to be a docile part of the atmosphere.

The best known simulations of stratospheric warmings were made by Matsuno (1971) and Holton (1976). Matsuno used a quasi-geostrophic model. It was a mechanistic model with forcing specified at the bottom boundary of the model which corresponded to the 10 km level.

The troposphere was not included in this formulation. The forcing consisted of a single zonal harmonic component. Interaction was allowed only between this wavenumber and the mean flow. His model produced many of the basic characteristics of observed warmings.

Quiroz et al. (1975) compared this model to recently available satellite data that generally supported the model results. They did note several discrepancies, such as cooling did not occur in the upper stratosphere in Matsuno's model as has been observed; the simulated westerlies in the mesosphere were much stronger than observed; and the changes during the first 1-10 days are too monotonic in comparison to observed vacillations. According to Schoeberl (1978), part of Matsuno's problem was due to the fact that neither damping nor friction was included in his calculations. This did not allow the mean zonal flow to relax after eddy forcing and also caused the critical level to numerically reflect any wave advance.

Holton (1976) used a primitive equation semi-spectral model. This model was also linear and confined to the upper atmosphere. The forcing, like Matsuno's, was turned on slowly at the tropopause and was held steady after reaching a maximum after several days of integration. His results generally tended to confirm many aspects of Matsuno's model. Holton did use damping and, perhaps as a consequence, his model did not show the downward propagation of the zero wind line nor did he get the double warming in the stratosphere. Quiroz (1969) has basically discounted the presence of downward propagating critical levels, but Quiroz et al. (1975) believe a double warming as simulated

by Matsuno is possible. Holton's easterlies are much more conservative than Matsuno's; but in the case of Holton's wave 1 forcing, the wind reversal did not extend deep enough into the lower stratosphere to be classified a major warming by WMO standards.

Using a high vertical resolution spectral model, Lordi (1978) went further and simulated sudden warmings allowing not only for wave and mean flow but also for wave-wave interactions deemed so important by Perry (1967). Starting with essentially the same initial conditions as Matsuno (1971) and Holton (1976) and employing the same single zonal harmonic forcing, he was able to produce sudden warmings. Using a linearized version of his model, Lordi was also able to simulate warmings, but the contrast between these results and those obtained using the "non-linear" version was quite remarkable. In this thesis, the term "linear" means interaction is allowed only between the wave and mean flow. "Non-linear" means the wave can interact with other waves and the mean flow. For wave 1 forcing, the non-linear simulation resulted in a more rapid warming than the linear case and indicated the contribution of higher harmonics to the warming process. For wave 2 forcing, the opposite was true as the linear case was more dynamic. Perhaps this was due to the fact that since only wave 2 was forced, wave 1 remains unaffected and cannot play an essential role in the warming process. Hence, wave energy was only transferred back in the mean flow or to wave 4 (the point of truncation), which may detract from wave 2's ability to produce a strong warming. In the linear case, wave 2 does not yield any energy to higher harmonics and

may cause the simulated warming to progress more strongly. These results clearly indicate that both waves 1 and 2 must play an important role in the warming process. The evolution of Lordi's wave 1 warming, in particular, which reflects wave 2 contributions as well, can be compared closely with the evolution of the warming of January 1973 as depicted by McInturff (1978). Another key observational consistency, which is not clearly evident in the data presented by other researchers mentioned above, is the evolution of the secondary jet maximum in the westerlies around 35 km at higher latitudes during the pre-warming stage as noted by Quiroz et al. (1975). This is produced in all of Lordi's integrations and precedes the sudden warming. The author has made detailed observational studies of the lower stratosphere during the major warmings of 1973-1974 and 1976-1977. These essentially wave 1 warmings are in close agreement with Lordi's wave 1 non-linear results in that there is no evidence of strong easterly development in the mid-latitudes of the lower stratosphere as evolved in wave 2 forcing cases and to some extent the wave 1 linear case. In all of Lordi's runs, the stratospheric warmings were accompanied by cooling in the upper stratosphere and mesosphere as well as cooling in the equatorial stratosphere.

The most recent simulated stratospheric warming calculations were done by Schoeberl and Stroberl (1980a). They used a model similar to that of Matsuno (1971), but included solar radiative heating due to O_2 and O_3 absorption, Newtonian cooling and Rayleigh friction. They again forced with a single zonal harmonic and compared evolution of

their calculations with and without damping. Without damping, they obtained results similar to Matsuno's (1971) with strong easterlies and fairly rapid reversals. With large damping, the warmings, as should be expected, occurred at a much slower rate and the easterly maximum that did develop was much less than those obtained in the undamped case. They indicated that damping controls the amplitude that a warming can achieve. They also reinforced the concept of Holton (1976) that lateral critical levels do play an essential role in the warming process. Their wave 2 warming evolved more rapidly than their wave 1 warming in contrast to the results of Lordi (1978), who used a fully non-linear model. Schoeberl and Strobel (1980a) also imply that warmings require strong westerlies in the lower stratosphere in contrast to the observational data presented by Koerner and Kao (1980).

Schoeberl and Strobel (1980b) recently added a troposphere to their previous model and orographically forced waves in the troposphere. Although in some of their cases, waves 1 and 2 were forced simultaneously, the waves were allowed to interact with each other through the mean flow only. Topography was gradually introduced over a 15 day period. Because of the large damping used, it took 85 days to develop a major warming and then only after the tropospheric jet was increased to 48 ms^{-1} from 36 ms^{-1} which they used in a previous attempt and failed to produce a warming. Although they presented only a brief account of their results, they concluded that wave 1 is much slower developing than wave 2 and therefore major warmings must be wave 2

phenomena, contradicting the observational data of Labitzke (1977, 1978). They also imply that a strong tropospheric jet and a strong polar night jet are essential for a strong warming, conditions which are not supported by Koerner and Kao (1980). Perhaps the reasons for these apparent discrepancies are that the damping used by Schoeberl and Stroberl (1980b) was too large and secondly wave-wave interactions were not permitted. It certainly does not appear to be realistic that sudden warmings should take so long to develop.

Perry (1967) stressed not only the importance of non-linear interactions in the stratosphere, but also the importance of wave-wave interactions in the troposphere as part of the sudden warming process. So far in a detailed model designed to study the warming phenomena only Lordi (1978) has allowed for wave-wave interactions in the stratosphere, but the tropospheric contribution was limited to continuous forcing applied at the tropopause. This forcing poses an artificial condition on the system as evident from the latitude time sections of geopotential for waves 1 and 2 presented by O'Neill and Taylor (1979). The model of Schoeberl and Stroberl (1980b) introduced a troposphere to replace the continuous forcing at the tropopause with a more realistic generation of wave 1 and 2 by orography. However, this model does not allow for wave-wave interactions, which from observational data Perry (1967) had found so important. These conditions may explain why none of the above models have been able to produce warmings with wind reversals comparable in vertical depth as that reported for the winter of 1976-1977 (Taylor and Perry, 1977).

The purpose of this thesis then is to simulate a sudden stratospheric warming with a completely non-linear model which also includes a troposphere. The model will be forced by a combination of zonal harmonic components 1 and 2 by using topography to simplistically represent the gross orographic features of the Northern Hemisphere. This allows for variable forcing of the stratosphere from the troposphere. Unlike many general circulations models, this model will include sufficient vertical resolution to closely follow vertical wave propagation that is so important in the warming process and in any tropospheric-stratospheric interactions.

In this undertaking, we will use a modified version of Lordi's (1978) model for the stratosphere and mesosphere. It will be coupled with a tropospheric spherical harmonic model adapted from the work of Bourke (1974) and Hoskins and Simmons (1975) with modifications. Studying only planetary scale waves, we then want to examine the role of orography in a warming event; the effect of the strength of the polar night jet; the pre-eminence of wave 1 or 2 in the warming process; importance of an upper atmospheric representation in long range numerical simulations; and the feedback effects that the stratosphere may have on the troposphere. These latter effects may contribute to long-term tropospheric climatic fluctuations as suggested by Kasahara et al. (1973).

CHAPTER 2

MODEL FORMULATION

The model to be formulated in this chapter basically consists of two parts. The upper part of the model includes the stratosphere and mesosphere and the basic equation development follows very closely after Lordi (1978). The lower tropospheric part of the model is loosely patterned after the tropospheric models of Bourke (1974) and Hoskins and Simmons (1975). The governing equations for each section of the model, although similar in many respects, are also radically different primarily because of the different vertical coordinate systems employed in each part. However, these somewhat independent equations can be merged into common matrix equations which allow us to perform semi-implicit time differencing on the entire system at the same time.

2.1 Vertical Coordinate Systems

In his model, Lordi used a log-pressure coordinate system defined as follows:

$$z = - H \ln (p/p_s), \quad (1)$$

where z is the height coordinate; p is the pressure; p_s is the mean surface pressure taken to be 1016 mb, and H is the scale height defined by

$$H = RT_m/g , \quad (2)$$

where R is specific gas constant of dry air, g the gravitational acceleration g , and T_m a mean atmospheric temperature assumed to be 244°K . While this system is satisfactory for the upper atmosphere, a modified sigma coordinate system, first introduced by Phillips (1957), is used for the troposphere in order to handle orography which is so important to any tropospheric model.

This σ -system is defined as follows:

$$\sigma = (p - p_R) / (p_* - p_R) , \quad (3)$$

where p_R is a reference pressure indicating the upper boundary of the tropospheric model and lower boundary of the upper model; p_* is the surface pressure; and p is the pressure at a given level. It follows from (3) that $\sigma = 0$ at $p = p_R$ and $\sigma = 1$ at $p = p_*$. In order to determine the reference pressure level, we can solve (1) for p to obtain

$$p = p_s \exp (-z/H) . \quad (4)$$

In his model, Lordi had a lower boundary height of $z_B = 12$ km. Hence, from (4) we can compute a reference pressure $p_R \approx 189.5$ mb, which will make the $\sigma = 0$ level of the troposphere coincide exactly with the 12 km level of the upper atmospheric model.

Figure 1 depicts the vertical grid structure of the coupled models. In the stratosphere and mesosphere, $\Delta z = 3$ km with 26 prognostic levels, which will generally be represented with the index K . The index r is used to indicate the 5 prognostic levels of the

troposphere where $\Delta\sigma = .2$. Vertical velocity (w or $\dot{\sigma}$) and geopotential (ϕ) are diagnostic variables and values are computed for diagnostic levels centered between the prognostic levels. Vorticity (ζ), divergence (D) and temperature (T) are the prognostic variables common to both models. Additionally, log pressure (q) is a prognostic variable in the troposphere. For boundary conditions, we assume vertical velocity is zero at the top of the upper model and the bottom of the lower model. We also specify surface geopotential as a bottom boundary condition. Vertical derivatives at the bottom of the troposphere will be specified in the parameterization of vertical diffusion to be discussed later in this chapter.

2.2 Governing Equations

The momentum, thermodynamics, continuity, and hydrostatic equations serve as the foundation for both models. Although the development of the upper atmospheric model equations will not be discussed in detail, mention will be made of slight modifications and essential equations as developed by Lordi (1978) will be introduced to complete the formulation. In the remaining part of this chapter, we will develop the tropospheric governing equations, give the stratospheric counterpart, form common matrix equations, and introduce the time differencing schemes use to perform model integrations.

After Kasahara (1974), the basic equations for a dry atmosphere in σ -coordinates can be written as follows:

$$\frac{\vec{dV}}{dt} = - \vec{fk} \times \vec{V} - \vec{\nabla}\phi - \frac{\sigma RT}{\sigma p_* + p_R} \vec{\nabla p}_* + \vec{F}; \quad (5)$$

$$\frac{dT}{dt} = \frac{RT}{c_p(\sigma p_* + pR)} \dot{p} + \frac{Q}{c_p} ; \quad (6)$$

$$\frac{\partial p_*}{\partial t} + \vec{\nabla} \cdot (p_* \vec{V}) + p_* \frac{\partial \sigma}{\partial \sigma} = 0 \quad (7)$$

$$\frac{\partial \Phi}{\partial \sigma} = - \frac{RT p_*}{\sigma p_* + pR} , \quad (8)$$

where \vec{V} is the horizontal velocity; f is the coriolis parameter; \vec{k} is the vertical unit vector; $\vec{\nabla}$ is the horizontal gradient operator; Φ is the geopotential. T is the temperature; $p_* = p_* - pR$; \vec{F} is the horizontal frictional force; c_p is the specific heat of dry air at constant pressure; $\dot{p} \equiv dp/dt$, the vertical velocity in pressure coordinates; Q is the diabatic heating; $\dot{\sigma} \equiv d\sigma/dt$ is the vertical velocity in σ -coordinates; and t represents time.

Using equation (5), we will be able to derive both vorticity and divergence tendency equations. Those derivations along with manipulated versions of (6)-(8) will serve as the basic model equations. In the following sections, we will develop these equations.

2.2.1 Vorticity Equations

Expanding the total time derivative of (5) and rearranging terms, the momentum equation can be written in the following form:

$$\frac{\partial \vec{V}}{\partial t} = - (\zeta + f) \vec{k} \times \vec{V} - \vec{\nabla}(\Phi + \frac{\vec{V} \cdot \vec{V}}{2}) - RT \vec{\nabla} Q - \dot{\sigma} (\frac{\partial \vec{V}}{\partial \sigma}) + \vec{F} , \quad (9)$$

where f is the coriolis parameter, $q \equiv \ln(\sigma P_* + p_R)$ and $\zeta \equiv \vec{k} \cdot \vec{\nabla} \times \vec{V}$, the vertical component of relative vorticity. If we let $T = \bar{T}(\sigma) + T'$, (i.e., temperature is composed of a layer mean and a deviation) and take $\vec{k} \cdot \vec{\nabla} \times (9)$, it follows that

$$\partial \zeta / \partial t = - \vec{\nabla} \cdot (\zeta + f) \vec{V} - \vec{k} \cdot \vec{\nabla} \times (RT' \vec{\nabla} q + \sigma \partial \vec{V} / \partial \sigma - \vec{F}) . \quad (10)$$

By the Helmholtz theorem \vec{V} can be expressed as the sum of non-divergent and irrotational parts as follows:

$$\vec{V} = \vec{k} \times \vec{\nabla} \psi + \vec{\nabla} \chi , \quad (11)$$

where ψ is the stream function and χ is the velocity potential. Hence, it follows that

$$\zeta = \vec{k} \cdot \vec{\nabla} \times \vec{V} = \nabla^2 \psi , \quad (12)$$

$$D = \vec{\nabla} \cdot \vec{V} = \nabla^2 \chi , \quad (13)$$

where D is the horizontal divergence. In spherical coordinates, we can express (11) in component form

$$u = - \frac{1}{a} \frac{\partial \psi}{\partial \phi} + \frac{1}{a \cos \phi} \frac{\partial \chi}{\partial \lambda} , \quad (14)$$

$$v = \frac{1}{a \cos \phi} \frac{\partial \psi}{\partial \lambda} + \frac{1}{a} \frac{\partial \chi}{\partial \phi} \quad (15)$$

where u is the zonal velocity component; v is the meridional velocity component, a is the earth's radius; ϕ is the latitude; and λ is the

longitude. If we further define

$$U \equiv u \cos \phi, \quad (16)$$

$$V \equiv v \cos \phi, \quad (17)$$

it follows from (14) and (15) that

$$U = - \frac{\cos \phi}{a} \frac{\partial \psi}{\partial \phi} + \frac{1}{a} \frac{\partial x}{\partial \lambda} \quad (18)$$

$$V = \frac{1}{a} \frac{\partial \psi}{\partial \lambda} + \frac{\cos \phi}{a} \frac{\partial x}{\partial \phi} \quad (19)$$

We can also express the frictional force \vec{F} in component form as

$$\vec{F} = F_\lambda \vec{i} + F_\phi \vec{j} \quad (20)$$

where F_λ and F_ϕ are the longitudinal and meridional components, respectively. The parameterization of these components will be detailed later in this chapter.

In order to control spectral blocking (Puri and Bourke, 1974) that results from horizontal truncation, diffusion is applied to the vorticity equation. Similar to Lordi (1978), we used the linear diffusion mechanism of Leith (1971). This technique damps deviations from equilibrium fields and not the equilibrium fields. With this specification added and using (12), (14)-(20), we can express the vorticity equation (10) in spherical coordinate form as follows:

$$\frac{\partial \nabla^2 \psi}{\partial t} = - \frac{1}{a \cos \phi} \left[\frac{\partial A}{\partial \lambda} + \cos \phi \frac{\partial B}{\partial \phi} \right] + K_h [\nabla^2 (\zeta - \zeta_e) + \frac{2(\zeta - \zeta_e)}{a^2}] \quad (21)$$

where we define

$$A \equiv (\zeta + f)U + \sigma(\partial V/\partial \sigma) + (RT'/a)\cos \phi(\partial q/\partial \phi) - F_\phi \cos \phi \quad (22)$$

$$B \equiv (\zeta + f)V - \sigma(\partial U/\partial \sigma) - (RT'/a)(\partial q/\partial \lambda) + F_\lambda \cos \phi \quad (23)$$

K_h is the horizontal diffusion coefficient. The e subscript represents equilibrium vorticity at the start of model integrations.

The parallel stratospheric equation as given by Lordi (1978) is as follows:

$$\frac{\partial \nabla^2 \psi}{\partial t} = - \frac{1}{a \cos^2 \phi} \left[\frac{\partial \hat{A}}{\partial \lambda} + \cos \phi \frac{\partial \hat{B}}{\partial \phi} \right] + K_h [\nabla^2(\zeta - \zeta_e) + \frac{2(\zeta - \zeta_e)}{a^2}] \quad (24)$$

where

$$\hat{A} = (\zeta + f)U + w(\partial V/\partial z) - F_\phi \cos \phi, \quad (25)$$

$$\hat{B} = (\zeta + f)V - w(\partial U/\partial z) + F_\lambda \cos \phi, \quad (26)$$

for $w \equiv dz/dt$ and z is defined by (1).

Combining (21) and (24), into a single expression, we can write

$$\frac{\partial \zeta}{\partial t} = Z + K_h [\nabla^2(\zeta - \zeta_e) + 2(\zeta - \zeta_e)/a^2] \quad (27)$$

where Z take on the values of the non-diffusive terms on the right side of (21) for the troposphere and the right hand side of (24) for the stratosphere and mesosphere.

2.2.2 Divergence Equation

The divergence tendency equation can be obtained by taking

$\vec{V} \cdot (9)$, which yields

$$\begin{aligned} \frac{\partial(\vec{V} \cdot \vec{V})}{\partial t} &= \vec{V} \cdot [-(\zeta + f)\vec{k} \times \vec{V}] - \nabla^2(\phi + \frac{\vec{V} \cdot \vec{V}}{2} + \frac{RT}{q}) \\ &- \vec{V} \cdot [RT' \vec{V} q + \dot{\sigma}(\partial \vec{V} / \partial \sigma) - \vec{F}] . \end{aligned} \quad (28)$$

Expanding (28) in spherical coordinates, introducing horizontal diffusion, and grouping terms as with the vorticity equation, we obtain

$$\frac{\partial \vec{V}^2}{\partial t} = \frac{1}{a \cos^2 \phi} \left[\frac{\partial B}{\partial \lambda} - \cos \phi \frac{\partial A}{\partial \phi} \right] - \nabla^2(E + \phi + RTq) + K_h [\nabla^2 D + 2(D/a^2)] \quad (29)$$

where

$$E \equiv \frac{\vec{V} \cdot \vec{V}}{2} = \frac{U^2 + V^2}{2 \cos^2 \phi} . \quad (30)$$

For the upper portion of the model, we have

$$\frac{\partial \vec{V}^2}{\partial t} = \frac{1}{a \cos^2 \phi} \left[\frac{\partial \hat{B}}{\partial \lambda} - \cos \phi \frac{\partial \hat{A}}{\partial \phi} \right] - \nabla^2(E + \phi) + K_h [\nabla^2 D + 2(D/a^2)] . \quad (31)$$

As a single combined equation, we can write the divergence tendency equation as

$$\frac{\partial D}{\partial t} = D - \nabla^2(\phi + cRTq) + K_h [\nabla^2 D + 2(D/a^2)] , \quad (32)$$

where $c = 0$ for the upper portion of the model and $c = 1$ for the troposphere and where D takes on the remaining values on the right of (29) that are not explicitly shown in (32) and on the right of (31) in a similar fashion for the lower and upper portions of the model

respectively.

2.2.3. Frictional Force \vec{F}

In this section we will define explicitly the frictional components F_λ and F_ϕ of \vec{F} that were alluded to in the development of the vorticity and divergence tendency equations. For the upper portion of the model F_λ and F_ϕ are characterized by Rayleigh friction. In the troposphere, vertical diffusion is also parameterized in these components along with Rayleigh friction.

Following the vertical stress formulations of Bourke et al. (1977) and the Rayleigh friction method used by Lordi (1978), we can express the tropospheric components of \vec{F} as follows:

$$F_\lambda = \frac{(g)}{p_*} \frac{\partial \tau}{\partial \sigma} - F_r (u - u_e) , \quad (33)$$

$$F_\phi = \frac{(g)}{p_*} \frac{\partial \tau}{\partial \sigma} - F_r v , \quad (34)$$

where F_r is the Rayleigh friction coefficient, u_e is the initial equilibrium zonal wind components; and

$$\tau_\lambda^2 = \rho \frac{(g)}{p_*} K_v \frac{\partial u}{\partial \sigma} , \quad (35)$$

$$\tau_\phi^2 = \rho \frac{(g)}{p_*} K_v \frac{\partial v}{\partial \sigma} , \quad (36)$$

for density ρ and vertical diffusion coefficient K_v defined as

$$K_v = \rho \left(\frac{g}{p_*} \right) v^2 \left| \frac{\partial V}{\partial \sigma} \right|, \quad (37)$$

where v is the mixing length which we assume has a value of 30 meters for $\sigma > .1$ and is zero for $\sigma < .1$.

The lower boundary specification is given by

$$\tau_{*x} = - \rho \frac{C_d}{N} \left| \frac{\partial V}{\partial N} \right| u_N \quad (38)$$

$$\tau_{*\phi} = - \rho \frac{C_d}{N} \left| \frac{\partial V}{\partial N} \right| v_N, \quad (39)$$

where the N subscript denotes the lowest prognostic level. C_d is the drag coefficient assumed to be .0025.

2.2.4 Vertical Velocity Expressions

Before we can proceed with the development of the remaining equations, we must first derive diagnostic expressions for vertical velocities of the various coordinate systems encountered and the relationships between them. Starting with equation (3), it follows that

$$\dot{\sigma} = \frac{1}{p_*} \left[\dot{p} - \sigma \frac{\partial p^*}{\partial t} \right]. \quad (40)$$

From (1), we also have

$$w = - (H/p) \dot{p}. \quad (41)$$

Since at $p = p_R$, $\sigma = 0$ we can combine (40) and (41) to obtain

$$\dot{\sigma}_R = - \frac{w_R}{P_* H} p_R, \quad (42)$$

where the R subscript represents reference pressure level evaluation.

Integration of the continuity equation (7) with respect to σ from 0 to σ using (42) yields

$$\sigma \frac{\partial P_*}{\partial t} + \int_0^\sigma \vec{\nabla} \cdot (P_* \vec{V}) d\sigma + P_* \dot{\sigma} + \frac{w_R p_R}{H} = 0. \quad (43)$$

Extending the integration of (43) to the earth's surface and using the bottom boundary condition that $\dot{\sigma}_{\sigma=1} = 0$, then we have

$$\frac{\partial P_*}{\partial t} = - \int_0^1 \vec{\nabla} \cdot (P_* \vec{V}) d\sigma - \frac{w_R p_R}{H}. \quad (44)$$

Substitution of (44) into (43) yields

$$\sigma \left[- \int_0^1 \vec{\nabla} \cdot (P_* \vec{V}) d\sigma - \frac{w_R p_R}{H} \right] + \int_0^\sigma \vec{\nabla} \cdot (P_* \vec{V}) d\sigma + P_* \dot{\sigma} + \frac{w_R p_R}{H} = 0 \quad (45)$$

and solving (45) for $\dot{\sigma}$, we can write

$$\dot{\sigma} = \frac{\sigma}{P_*} \int_0^1 \vec{\nabla} \cdot (P_* \vec{V}) d\sigma - \frac{1}{P_*} \int_0^\sigma \vec{\nabla} \cdot (P_* \vec{V}) d\sigma + (\sigma-1) \frac{w_R p_R}{P_* H}, \quad (46)$$

which gives us a diagnostic expression for $\dot{\sigma}$.

If we substitute (46) into (40) and solve for \dot{p} , we obtain

$$\dot{p} = \sigma \int_0^1 \vec{\nabla} \cdot (P_* \vec{V}) d\sigma - \int_0^\sigma \vec{\nabla} \cdot (P_* \vec{V}) d\sigma + (\sigma-1) \frac{w_R p_R}{H} + \sigma \frac{dP_*}{dt}. \quad (47)$$

Since

$$\frac{dP_*}{dt} = \frac{\partial P_*}{\partial t} + \vec{V} \cdot \vec{\nabla} P_*, \quad (48)$$

then substitution of (44) into (48) yields

$$\frac{dP_*}{dt} = - \int_0^1 \vec{\nabla} \cdot (P_* \vec{V}) d\sigma - \frac{w P}{R^2} + \vec{V} \cdot \vec{\nabla} P_*. \quad (49)$$

Using (49) in conjunction with (47) yields

$$\dot{p} = - \int_0^{\sigma} \vec{\nabla} \cdot (P_* \vec{V}) d\sigma - \frac{w P}{R^2} + \sigma \vec{V} \cdot \vec{\nabla} P_*, \quad (50)$$

a diagnostic expression for \dot{p} .

Although tropospheric vertical velocity computations in height coordinates are not required in any model calculations, it is computed for output and display purposes. Tropospheric vertical velocities can then be related more meaningfully with the vertical velocities of the upper portion of the model, even though those values are not with respect to a true height system. From the relationship that $w(\partial p / \partial z) = \dot{\sigma}(\partial p / \partial \sigma)$, we can solve for w and substitute the hydrostatic equation (8) to obtain

$$w = \frac{-RTP_*}{g(\sigma P_* + p)} \dot{\sigma}. \quad (51)$$

Since we need only approximate values for output purposes, we assume

$$T = T_m.$$

In the upper part of the model, vertical velocity is expressed in two ways as follows:

$$w^* = \int_z^{z_{TOP}} \left(\exp(-z) \frac{\vec{v}}{H} \cdot \vec{v} \right) dz \quad (52)$$

$$w = w^* \exp\left(\frac{z}{H}\right). \quad (53)$$

Therefore, at the lower boundary at the interface, (52) and (53) imply

$$w_R = \exp\left(\frac{-R}{H}\right) \int_{-R}^{z_{TOP}} \left(\exp(-z) \frac{\vec{v}}{H} \cdot \vec{v} \right) dz, \quad (54)$$

which can be used in conjunction with (46) and (50) in isolating the divergence in the thermodynamic and continuity equation in preparation for semi-implicit time differencing.

2.2.5 Thermodynamic Equation

Expanding the thermodynamic equation (6) and expressing temperature in terms of a layer mean and deviation allows us to write

$$\frac{\partial T'}{\partial t} = - \vec{v} \cdot \vec{\nabla} T' - \frac{\partial}{\partial \sigma} \frac{\partial(\bar{T}+T')}{\partial \sigma} + \frac{R(\bar{T}+T')}{c(\sigma p^* + p)} \frac{\partial p}{\partial \sigma} + \frac{Q}{c}. \quad (55)$$

Further expansion of the gradient operator $\vec{\nabla}$ and writing (55) in spherical coordinates, it follows that

$$\frac{\partial T'}{\partial t} = \frac{-1}{a \cos \phi} \left[\frac{\partial U T'}{\partial \lambda} + \cos \phi \frac{\partial V T'}{\partial \phi} \right] + D T' - \sigma \frac{\partial (\bar{T} + T')}{\partial \sigma} + \frac{R(\bar{T} + T')}{c_p (\sigma p_* + p_R)} \frac{\partial p}{\partial p} + \frac{Q}{c_p} . \quad (56)$$

Substitutions of (46) for σ for the mean vertical gradient part of (56) and (50) for p and expanding the horizontal gradient operator in these expressions, i.e., $\vec{\nabla} \cdot (\vec{P}_* \vec{V}) = \vec{P}_* \vec{D} + \vec{V} \cdot \vec{\nabla} \vec{P}_*$, we can write

$$\begin{aligned} \frac{\partial T'}{\partial t} = & - \frac{1}{a \cos^2 \phi} \left[\frac{\partial U T'}{\partial \lambda} + \cos \phi \frac{\partial V T'}{\partial \phi} \right] + D T' + \frac{Q}{c_p} - \sigma \frac{\partial T'}{\partial \sigma} \\ & - (\partial \bar{T} / \partial \sigma) \left[\frac{\sigma}{p_*} \int_0^1 (\vec{V} \cdot \vec{\nabla} \vec{P}_*) d\sigma - \frac{1}{p_*} \int_0^\sigma (\vec{V} \cdot \vec{\nabla} \vec{P}_*) d\sigma \right] \\ & - \frac{R T'}{c_p (\sigma p_* + p_R)} \left[\int_0^\sigma (\vec{P}_* \vec{D} + \vec{V} \cdot \vec{\nabla} \vec{P}_*) d\sigma - \sigma \vec{V} \cdot \vec{\nabla} \vec{P}_* + \frac{w p}{H} \right] \\ & - \frac{R \bar{T}}{c_p (\sigma p_* + p_R)} \left[\int_0^\sigma (\vec{V} \cdot \vec{\nabla} \vec{P}_*) d\sigma - \sigma \vec{V} \cdot \vec{\nabla} \vec{P}_* \right] \\ & - \frac{\partial \bar{T}}{\partial \sigma} \left[\sigma \int_0^1 D d\sigma - \int_0^\sigma D d\sigma + (\sigma - 1) \frac{w p}{H} \right] \\ & - \frac{R \bar{T} p_*}{c_p (\sigma p_* + p_R)} \left[\int_0^\sigma D d\sigma + \frac{w p}{H} \right] . \quad (57) \end{aligned}$$

Similar to Lordi (1978), we express the diabatic heating as

$$\frac{Q/c}{p} = \alpha(z)(T' - T_e) \quad (58)$$

which is based on the work of Leovy (1964), where T_e is the equilibrium temperature deviation and $\alpha(z)$ is the Newtonian heating-cooling coefficient given by Holton (1976):

$$\alpha(z) = [1.5 + \tanh(\frac{z-35000}{7000})] \times 10^{-6} s^{-1}, \quad (59)$$

where the height corresponding to the σ -coordinate level is computed from mean and deviation geopotential fields.

In order to have divergence involved with mean quantities, we define

$$\beta \equiv \bar{\beta}(\sigma) + \beta' \equiv \frac{p_*}{\sigma p_* + p_R}, \quad (60)$$

$$\delta \equiv \bar{\delta}(\sigma) + \delta' = (1/p_*) . \quad (61)$$

Using (54), (60), and (61) to isolate divergence with mean terms and adding horizontal and vertical diffusion, we can express (57) as follows:

$$\begin{aligned}
\frac{\partial T'}{\partial t} = & - \frac{1}{a \cos^2 \phi} \left[\frac{\partial \Omega T'}{\partial \lambda} + \cos \phi \frac{\partial \Omega T'}{\partial \phi} \right] + \Omega T' + \alpha(z)(T' - T) \\
& + \frac{K}{h} \left[\frac{\partial^2}{\partial z^2} \left(\frac{T' - T}{e} \right) \right] + \frac{F}{v T} - \frac{\partial}{\partial \sigma} \left(\frac{\partial T'}{\partial \sigma} \right) \\
& - (\partial \bar{T} / \partial \sigma) \left[\frac{\sigma}{p_*} \int_0^1 (\vec{V} \cdot \vec{\nabla} p_*) d\sigma - \frac{1}{p_*} \int_0^\sigma (\vec{V} \cdot \vec{\nabla} p_*) d\sigma + \delta'(\sigma-1) \frac{w p}{H} R R \right] \\
& - \frac{R T'}{c (p_*^0 + p_* R)} \left[\int_0^\sigma (p_*^0 D + \vec{V} \cdot \vec{\nabla} p_*) d\sigma - \sigma \vec{V} \cdot \vec{\nabla} p_* + \frac{w p}{H} R R \right] \\
& - \frac{R \bar{T}}{c (p_*^0 + p_* R)} \left[\int_0^\sigma (\vec{V} \cdot \vec{\nabla} p_*) d\sigma - \sigma \vec{V} \cdot \vec{\nabla} p_* + p_* \delta' \frac{w p}{H} R R \right] \\
& - \frac{R \bar{T}}{c p_*} \beta' \left[\int_0^\sigma D d\sigma + \bar{\sigma} \frac{w p}{H} R R \right] \\
& - (\partial \bar{T} / \partial \sigma) \left[\sigma \int_0^1 D d\sigma - \int_0^\sigma D d\sigma + \bar{\sigma} (\sigma-1) \frac{p R}{H} \exp \left(\frac{z_R}{H} \right) \int_{z_R}^{z_{TOP}} D \exp \left(\frac{-z}{H} \right) dz \right] \\
& - \frac{R \bar{T}}{c p_*} \bar{\beta} \left[\int_0^\sigma D d\sigma + \bar{\sigma} \frac{p R}{H} \exp \left(\frac{z_R}{H} \right) \int_{z_R}^{z_{TOP}} D \exp \left(\frac{-z}{H} \right) dz \right], \quad (62)
\end{aligned}$$

where $\frac{F}{v T}$ denotes the vertical diffusion term. After Bourke et al. (1977), $\frac{F}{v T}$ is defined as follows:

$$\frac{F}{v T} = (g/p_*) (\partial \eta / \partial \sigma), \quad (63)$$

where

$$\eta = \frac{\pi \rho^2}{v} (g/p_*) K (\partial \theta / \partial \sigma). \quad (64)$$

Here K_v is defined by (37); $\theta = T(p_0/p)^{R/c_p}$ p is the potential temperature with $p_0 = 1000$ mb, and $\Pi = (p/p_0)^{R/c_p}$. For the lower boundary specification we assume thermal insulation, i.e. $n_* = 0$.

For the stratosphere, we have a thermodynamic equation of the following form:

$$\frac{\partial T'}{\partial t} = \frac{-1}{a \cos^2 \phi} \left[\frac{\partial(UT')}{\partial \lambda} + \cos \phi \frac{\partial(VT')}{\partial \phi} \right] + DT' - w \frac{\partial T'}{\partial z}$$

$$+ K_h \left[\frac{\nabla^2}{e} (T' - T_e) \right] - \frac{RT'w}{c_p H} + \alpha(T' - T_e) - \frac{HN^2}{R} \exp(\frac{z}{H}) \int_z^{z_{TOP}} D \exp(-\frac{z}{H}) dz, \quad (65)$$

where N^2 is the buoyancy frequency defined by

$$N^2 \equiv \frac{R}{H} \left[\frac{d\bar{T}}{dz} + \frac{R\bar{T}}{c_p H} \right] \quad (66)$$

which is assumed to be constant throughout the stratosphere and mesosphere. The term $RT'w/c_p H$ was neglected in Lordi's formulation.

Combining (62) and (65) as a single expression, we can write

$$\frac{\partial T'}{\partial t} = T - \text{CONSTANT} \times \int D \quad (67)$$

i.e., temperature can be expressed as a group of terms varying in time minus terms, constant in time, times an integral of the divergence.

2.2.6 Continuity Equation

Expanding the horizontal gradient operator of equation (47), we can express the continuity equation as follows:

$$(\partial P_*/\partial t) = - \int_0^1 (V \cdot \nabla P_*) d\sigma - \int_0^1 P_* D d\sigma - \frac{w_R p_R}{H}. \quad (68)$$

Multiplying (68) by $\sigma/(\sigma P_* + p_R)$ yields

$$\frac{\partial q}{\partial t} = \frac{-\sigma}{\sigma P_* + p_R} \int_0^1 (V \cdot \nabla P_*) d\sigma - \frac{\sigma P_*}{\sigma P_* + p_R} \left[\int_0^1 D d\sigma + \frac{w_R p_R}{P_* H} \right]. \quad (69)$$

Using (54), (60), and (61), we can isolate divergence and mean quantities to obtain

$$\begin{aligned} \frac{\partial q}{\partial t} = & \frac{-\sigma}{\sigma P_* + p_R} \left[\int_0^1 (V \cdot \nabla P_*) d\sigma + P_* \delta' \frac{w_R p_R}{H} \right] \\ & - \sigma \beta' \left[\int_0^1 D d\sigma + \frac{w_R p_R}{H} \right] \\ & - \sigma \bar{\beta} \left[\int_0^1 D d\sigma + \frac{p_R}{H} \exp\left(\frac{z_R}{H}\right) \int_{z_R}^{z_T} D \exp\left(\frac{-z}{H}\right) dz \right]. \quad (70) \end{aligned}$$

The continuity equation is not a prognostic equation in the stratosphere and is used primarily to compute vertical velocities as given by (52). Assuming $\partial q/\partial t = 0$ for the upper part of the model, we can still write a combined equation such as

$$(\partial q/\partial t) = P - \text{constant} \times \int D \quad (71)$$

where P is the varying part and described by the first two terms on the right of (70) for the troposphere and zero for the stratosphere and mesosphere. Similarly, the constant is zero for the upper portion of the model.

2.2.7 Hydrostatic Equation

Rearranging the hydrostatic equation (8), we have

$$\frac{\frac{\partial \sigma P}{\partial P} *}{\sigma P * + p_R} = - \frac{\partial \Phi}{RT} \quad (72)$$

which can be further simplified as follows:

$$\frac{\partial \Phi}{\partial q} = - RT . \quad (73)$$

In terms of layer mean quantities and deviations from layer means, we can write

$$\frac{\partial \bar{\Phi}}{\partial \bar{q}} = - \bar{RT} , \quad (74a)$$

$$\frac{\partial \Phi'}{\partial q} = - RT' . \quad (74b)$$

According to Kurihara (1968) the form of (73) yields a more accurate estimation of geopotential over variable topography when employing finite difference integrations.

For the stratosphere, we have

$$\frac{\partial \Phi'}{\partial z} = \frac{RT'}{H} , \quad (75)$$

with a similar expression for layer mean quantities. Equations (74b) and (75) can be combined into a single expression when we depict the equations in the discrete state later in this chapter.

2.3 Vertical Differencing

In this model, vertical derivatives and integrals are computed via finite difference methods. Both parts of the model employ the same differencing techniques. For the upper portion of the model this is a slight change from the original centered space differencing techniques as used by Lordi (1978).

Since vertical velocity, $\dot{\sigma}$ for example, is formed at diagnostic levels and the prognostic variables are defined at alternate levels, we define basic differencing schemes involving $\dot{\sigma}$ and the prognostic variables denoted by X , at prognostic level r . Similar to Corby et al. (1972), these relationships are

$$(X \frac{\partial \dot{\sigma}}{\partial \sigma})_r = X_r \frac{(\dot{\sigma}_{r+\frac{1}{2}} - \dot{\sigma}_{r-\frac{1}{2}})}{2\Delta\sigma}; \quad (76)$$

$$(\dot{\sigma} \frac{\partial X}{\partial \sigma})_r = \frac{\dot{\sigma}_r (X_{r+\frac{1}{2}} - X_{r-\frac{1}{2}}) + \dot{\sigma}_{r-\frac{1}{2}} (X_r - X_{r-1})}{2\Delta\sigma}; \quad (77)$$

$$(\frac{\partial \dot{\sigma} X}{\partial \sigma})_r = \frac{\dot{\sigma}_r (X_{r+\frac{1}{2}} + X_r) - \dot{\sigma}_{r-\frac{1}{2}} (X_r + X_{r-1})}{2\Delta\sigma}. \quad (78)$$

Level representation and indexing are denoted in Figure 1, where $\Delta\sigma = .2$ and $\sigma_r = r\Delta\sigma$. When $r = \frac{1}{2}$ we use the following relationship at the boundary:

$$[\dot{\sigma} \frac{\partial(\quad)}{\partial \sigma}]_R = [w \frac{\partial(\quad)}{\partial z}]_R \quad (79)$$

or in discrete form

$$[w \frac{\partial(\)}{\partial z}]_R = \exp(\frac{z}{H}) w^* R \frac{[(\)_{K=\frac{1}{2}} - (\)_{r=\frac{1}{2}}]}{z_{K=\frac{1}{2}} - z_{r=\frac{1}{2}}}. \quad (80)$$

Another special case occurs when $r = 4\frac{1}{2}$. Here $\sigma_5 = 0$ and (76 - 78) can be simplified accordingly.

It follows from the specifications of (76 - 78), that the finite difference analog maintains the following derivative relationship:

$$\frac{\partial(\dot{\sigma}X)}{\partial\sigma} = \dot{\sigma} \frac{\partial X}{\partial\sigma} + X \frac{\partial\dot{\sigma}}{\partial\sigma}. \quad (81)$$

It can also easily be shown that a similar relationship holds for

$$\frac{\partial(\dot{\sigma}\frac{\partial V}{\partial\sigma})^2}{\partial\sigma} = V \cdot (\dot{\sigma} \frac{\partial V}{\partial\sigma}) + \frac{1}{2} V^2 \frac{\partial^2\dot{\sigma}}{\partial\sigma^2}. \quad (82)$$

Vertical integrals are treated discretely in the following manner:

$$(\int_0^{\sigma} X d\sigma)_{r+\frac{1}{2}} = \sum_{s=\frac{1}{2}}^r X \Delta\sigma, \quad (83)$$

where r represents a prognostic level. From (83), it follows that integral quantities are formed only at diagnostic levels. To obtain values at the prognostic levels centered averaging of adjacent diagnostic level values is used.

For the hydrostatic equation (74b) for the troposphere, we employ the following discrete scheme:

$$\frac{\phi'}{r+\frac{1}{2}} - \frac{\phi'}{r-\frac{1}{2}} = - \frac{Ra}{r} \frac{T'}{r}, \quad (84)$$

where

$$\frac{\alpha}{r} \equiv \ln \left[\left(\sigma_{r+\frac{1}{2}} \frac{P}{R} + p_R \right) / \left(\sigma_{r-\frac{1}{2}} \frac{P}{R} + p_R \right) \right]. \quad (85)$$

Geopotentials determined by (84) correspond to diagnostic levels and centered averaging is used to obtain values at prognostic levels.

For the upper portion of the model, (75) is expressed discretely by simple centered differencing, i.e.

$$\frac{\phi}{K+\frac{1}{2}} - \frac{\phi}{K-\frac{1}{2}} = \frac{RT'}{H} \Delta z \quad (86)$$

and averaging is used to obtain prognostic level values.

2.3.1 Mass Conservation

Lorenz (1960) showed that one can maintain integral constraints when vertical derivatives are replaced by finite difference analogs. This was the reason behind defining the schemes presented in the previous section. As pointed out by Arakawa and Lamb (1977), the maintenance of certain integral constraints such as mass and total energy conservation by finite differences may not be critical for short range numerical weather prediction on the order of one or two days. However, long-term integrations beyond a few days require conservation of these properties to prevent non-linear computational instability, false cascade of energy into smaller scale motions, and other undesirable features which can reduce the overall forecast accuracy of the model.

In this section, we test the continuity equation for the maintenance of mass conservation. Writing (44) in discrete form as detailed in the last section, we have

$$(\partial P_* / \partial t) = - \sum_{r=3}^{4\frac{1}{2}} (\vec{\nabla} \cdot (P_* \vec{V}) \Delta \sigma) - \frac{w_p}{R} . \quad (87)$$

If we integrate (87) over the entire globe, the horizontal gradient terms vanish and mass conservation ($\partial P_* / \partial t = 0$) requires that

$$\iint_S w \frac{dS}{R} = 0 , \quad (88)$$

where S represents the global surface. Substitution of (54) for w based on the upper model formulation clearly indicates that (88) indeed holds and shows that this modeling conserves mass.

2.3.2 Conservation of Total Energy

In order to prove total energy conservation, we need to derive the governing energy equation in discrete form. To derive the kinetic energy equation, we multiply the momentum equation (5) by $P_* \vec{V} \cdot \vec{r}$ to obtain

$$P_* \frac{\partial \frac{1}{2} \vec{V}^2}{\partial t} + P_* \vec{V} \cdot \vec{V} \frac{\partial \frac{1}{2} \vec{V}^2}{\partial r} + (P_* \vec{V} \cdot \vec{\sigma} \frac{\partial \vec{V}}{\partial \sigma}) = - \vec{P} \cdot \vec{V} \frac{\partial \vec{V}}{\partial r} - P_* R T \vec{V} \cdot \vec{\nabla} q + P_* \vec{V} \cdot \vec{F} . \quad (89)$$

Multiplying the continuity equation (7) by $\frac{1}{2} \vec{V}^2$ yields

$$\frac{1}{2} \vec{V}^2 (\partial P_* / \partial t) + \frac{1}{2} \vec{V}^2 \vec{\nabla} \cdot (P_* \vec{V}) + \left(\frac{1}{2} \vec{V}^2 \frac{\partial P_* \vec{\sigma}}{\partial \sigma} \right) = 0 \quad (90)$$

where the $\left(\frac{\partial}{\partial r}\right)$ terms in (89) and (90) involve vertical differencing evaluated at prognostic level r . However, since the discrete relationship for (82) holds, we can add (89) and (90) to obtain the following kinetic energy equation:

$$\begin{aligned} \frac{\partial P_* \frac{\dot{V}^2}{2}}{\partial t} + \vec{\nabla} \cdot (P_* \frac{\dot{V}}{r} \frac{\dot{V}^2}{2}) + \left[\frac{\partial P_* \frac{\dot{V}^2}{2}}{\partial \sigma} \right]_r \\ = - P_* \frac{\dot{V}}{r} \cdot \vec{\nabla} \phi - P_* R T \frac{\dot{V}}{r} \cdot \vec{\nabla} q + P_* \frac{\dot{V}}{r} \cdot \vec{F}_r. \end{aligned} \quad (91)$$

In a similar fashion, we can multiply the thermodynamic equation (6) by $P_* \frac{c}{p}$ and the continuity equation (7) by $c \frac{T}{p} r$ and add the resulting equation using the discrete property of (81) to yield

$$\frac{\partial P_* \frac{c}{p} \frac{T}{r}}{\partial t} + \vec{\nabla} \cdot (P_* \frac{\dot{V}}{r} \frac{c}{p} \frac{T}{r}) + \left[\frac{\partial (P_* \frac{c}{p} \frac{T}{r})}{\partial \sigma} \right]_r = \frac{R T P}{\frac{\sigma P + p}{r} R} \frac{\dot{p}}{r} + P_* \frac{Q}{r}. \quad (92)$$

as the thermodynamic energy equation. Adding (91) and (92), we have a total energy equation of the following form:

$$\begin{aligned} \frac{\partial [P_* \frac{(\frac{1}{2} \dot{V}^2 + c T)}{p r}]}{\partial t} + \vec{\nabla} \cdot [P_* \frac{\dot{V}}{r} \frac{(\frac{1}{2} \dot{V}^2 + c T)}{p r}] + \left\{ \frac{\partial [P_* \frac{(\frac{1}{2} \dot{V}^2 + c T)}{p}]}{\partial \sigma} \right\}_r \\ (a) \quad (b) \quad (c) \quad (d) \\ = - P_* \frac{\dot{V}}{r} \cdot \vec{\nabla} \phi - P_* R T \frac{\dot{V}}{r} \cdot \vec{\nabla} q + \frac{R T P}{\frac{\sigma P + p}{r} R} \frac{\dot{p}}{r} + P_* \frac{(\vec{V} \cdot \vec{F} + Q)}{r}, \end{aligned} \quad (93)$$

where we have denoted that the four terms on the right of (93) by (a), (b), (c), and (d) for future reference.

Substituting the discrete form of (50) for p in term (c) above allows us to write

$$(b) + (c) = - P_*^* \frac{RT}{r} \frac{\vec{V}}{r} \cdot \vec{\nabla} q_r + \frac{P_*^* r}{\sigma P_*^* + p_*^* R} [\sigma \frac{\vec{V}}{r} \cdot \vec{\nabla} P_*^* - \frac{w_p}{R R} - \frac{1}{2} \sum_{s=\frac{1}{2}}^r \vec{\nabla} \cdot (P_*^* \frac{\vec{V}}{s}) \Delta \sigma + \sum_{s=\frac{1}{2}}^{r-1} \vec{\nabla} \cdot (P_*^* \frac{\vec{V}}{s}) \Delta \sigma]. \quad (94)$$

Since the first term on the right of (94) cancels with the first part of the second term and substituting (43) for the remaining terms in [] yields

$$(b) + (c) = \frac{P_*^* RT}{\sigma P_*^* + p_*^* R} [P_*^* \frac{\vec{\sigma}}{r} + \sigma \frac{\partial P}{\partial t}]. \quad (95)$$

Using the hydrostatic equation (8) and (95) allows us to write

$$(b) + (c) = (- P_*^* \frac{\partial \Phi}{\partial \sigma} \frac{\vec{\sigma}}{r}) + (- \sigma \frac{\partial \Phi}{\partial \sigma} \frac{\partial P}{\partial t} \frac{\vec{\sigma}}{r}). \quad (96)$$

Substitution of (72) into the second term on the right of (96) gives us

$$(b) + (c) = (- P_*^* \frac{\partial \Phi}{\partial \sigma} \frac{\vec{\sigma}}{r}) + (\sigma RT \frac{\partial q}{\partial \sigma} \frac{\partial P}{\partial t} \frac{\vec{\sigma}}{r}). \quad (97)$$

The horizontal gradient operator of term (a) can be expanded as follows:

$$(a) = - \vec{\nabla} \cdot (P_*^* \frac{\vec{V}}{r} \frac{\vec{\phi}}{r}) + \vec{\phi} \cdot \vec{\nabla} \cdot (P_*^* \frac{\vec{V}}{r}). \quad (98)$$

From the continuity equation (7), the above term can be written

$$(a) = - \vec{\nabla} \cdot (P_* \vec{V} \frac{\phi}{r}) + \phi \left(- \frac{\partial P_*}{\partial t} - P_* \frac{\partial \sigma}{\partial r} \right) \quad (99)$$

or with further manipulation because property (81) holds for the discrete state, (99) becomes

$$(a) = - \vec{\nabla} \cdot (P_* \vec{V} \frac{\phi}{r}) - \phi \frac{\partial P_*}{\partial t} - \left(\frac{\partial P_* \frac{\phi}{r}}{\partial \sigma} \right)_r + (P_* \frac{\partial \phi}{\partial \sigma})_r. \quad (100)$$

Hence, substitution of (97) and (100) into (93) yields

$$\begin{aligned} & \frac{\partial [P_* \frac{(\frac{1}{2}V^2 + c T)}{r p r}]}{\partial t} + \vec{\nabla} \cdot [P_* \vec{V} \frac{(\frac{1}{2}V^2 + c T + \phi)}{r p r}] + \left\{ \frac{\partial [P_* \frac{\partial (\frac{1}{2}V^2 + c T + \phi)}{r p r}]}{\partial \sigma} \right\}_r \\ & = - (\phi - \sigma R T \frac{\partial q}{\partial \sigma}) \frac{\partial P_*}{\partial t} + P_* \vec{V} \cdot \vec{F} \frac{1}{r} \quad (101) \end{aligned}$$

If we integrate the first term on the right of (101) from the bottom to the top troposphere boundary, we have

$$\begin{aligned} & \sum_{r=1}^{4\frac{1}{2}} - (\phi - R \sigma T \frac{\partial q}{\partial \sigma}) \frac{\partial P_*}{\partial t} \Delta \sigma = - \frac{\partial P_*}{\partial t} \Delta \sigma \left[(\phi_{\frac{1}{2}} + \phi_{1\frac{1}{2}} + \phi_{2\frac{1}{2}} + \phi_{3\frac{1}{2}} + \phi_{4\frac{1}{2}}) \right. \\ & \left. - \frac{R}{\Delta \sigma} (\sigma_{\frac{1}{2}} T_{\frac{1}{2}} + \sigma_{1\frac{1}{2}} T_{1\frac{1}{2}} + \sigma_{2\frac{1}{2}} T_{2\frac{1}{2}} + \sigma_{3\frac{1}{2}} T_{3\frac{1}{2}} + \sigma_{4\frac{1}{2}} T_{4\frac{1}{2}}) \right]. \quad (102) \end{aligned}$$

By using (84) and by successive substitution, we can write

$$\phi_4 = \phi_* + R \sigma_{4\frac{1}{2}} T_{4\frac{1}{2}}; \quad (103a)$$

$$\phi_3 = \phi_* + R (\sigma_{4\frac{1}{2}} T_{4\frac{1}{2}} + \sigma_{3\frac{1}{2}} T_{3\frac{1}{2}}); \quad (103b)$$

$$\Phi_2 = \Phi_* + R(\alpha_{4\frac{1}{2}} T_{4\frac{1}{2}} + \alpha_{3\frac{1}{2}} T_{3\frac{1}{2}} + \alpha_{2\frac{1}{2}} T_{2\frac{1}{2}}) ; \quad (103c)$$

$$\Phi_1 = \Phi_* + R(\alpha_{4\frac{1}{2}} T_{4\frac{1}{2}} + \alpha_{3\frac{1}{2}} T_{3\frac{1}{2}} + \alpha_{2\frac{1}{2}} T_{2\frac{1}{2}} + \alpha_{1\frac{1}{2}} T_{1\frac{1}{2}}) ; \quad (103d)$$

$$\Phi_B = \Phi_* + R(\alpha_{4\frac{1}{2}} T_{4\frac{1}{2}} + \alpha_{3\frac{1}{2}} T_{3\frac{1}{2}} + \alpha_{2\frac{1}{2}} T_{2\frac{1}{2}} + \alpha_{1\frac{1}{2}} T_{1\frac{1}{2}} + \alpha_{\frac{1}{2}} T_{\frac{1}{2}}) ; \quad (103e)$$

where $\Phi_* = \Phi_5$ the surface geopotential and $\Phi_B = \Phi_0$ the geopotential at the reference pressure boundary. Using (103a-e) and averaging diagnostic level values to obtain prognostic values, we have

$$\begin{aligned} & \Phi_{\frac{1}{2}} + \Phi_{1\frac{1}{2}} + \Phi_{2\frac{1}{2}} + \Phi_{3\frac{1}{2}} + \Phi_{4\frac{1}{2}} \\ &= 5\Phi_* + R(.5\alpha_{\frac{1}{2}} T_{\frac{1}{2}} + 1.5\alpha_{1\frac{1}{2}} T_{1\frac{1}{2}} + 2.5\alpha_{2\frac{1}{2}} T_{2\frac{1}{2}} + 3.5\alpha_{3\frac{1}{2}} T_{3\frac{1}{2}} + 4.5\alpha_{4\frac{1}{2}} T_{4\frac{1}{2}}) . \quad (104) \end{aligned}$$

Substituting (104) into (102) and using the actual σ values, (102) becomes

$$\sum_{r=\frac{1}{2}}^{4\frac{1}{2}} - (\Phi - R\sigma T \frac{\partial q}{\partial \sigma} r \frac{\partial P}{\partial t})^* \Delta \sigma = 5\Phi_* \frac{\partial P}{\partial t}^* \Delta \sigma . \quad (105)$$

Using expression (105), we can now write the entire results of equation (101) integrated from the top tropospheric boundary down to the surface as

$$\begin{aligned} & \frac{\partial}{\partial t} [P_* \sum_{r=\frac{1}{2}}^{4\frac{1}{2}} (\frac{1}{r} \vec{V}^2 + c T + \Phi_*) \Delta \sigma + \vec{V} \cdot \sum_{r=\frac{1}{2}}^{4\frac{1}{2}} (\frac{1}{r} \vec{V}^2 + c T + \Phi_*) \Delta \sigma] \\ &+ \sum_{r=\frac{1}{2}}^{4\frac{1}{2}} \left\{ \frac{\partial [P_* \sigma (\frac{1}{r} \vec{V}^2 + c T + \Phi_*)]}{\partial \sigma} \right\} \frac{1}{r} \Delta \sigma = \sum_{r=\frac{1}{2}}^{4\frac{1}{2}} [P_* (\frac{1}{r} \vec{V} \cdot \vec{F} + Q_r)] \Delta \sigma . \quad (106) \end{aligned}$$

Performing the discrete differencing as specified by (78) on the vertical flux term of (106) yields

$$\sum_{r=\frac{1}{2}}^{4\frac{1}{2}} \left\{ \frac{\partial [P_* \sigma (\frac{1}{2} \vec{V}^2 + c_p T + \phi)]}{\partial \sigma} \right\}_r \Delta \sigma = -P_* \sigma \left(\frac{1}{2} \vec{V}^2 + c_p T + \phi \right)_R \quad (107)$$

where $\left(\cdot \right)_R$ indicates evaluation at the reference level. If we substitute (107) into (106); assume adiabatic and frictionless conditions; and integrate over the entire global surface, we obtain

$$\frac{\partial}{\partial t} \iint_S [P_* \sum_{r=\frac{1}{2}}^{4\frac{1}{2}} \left(\frac{1}{2} \vec{V}^2 + c_p T + \phi \right)_r \Delta \sigma] dS = \iint_S P_* \sigma \left(\frac{1}{2} \vec{V}^2 + c_p T + \phi \right)_R dS. \quad (108)$$

A similar analysis can be made for the upper portion of the model to yield

$$\begin{aligned} \frac{\partial}{\partial t} \iint_S \left[\frac{P_*}{H} \sum_{K=\frac{1}{2}}^{2\frac{1}{2}} \left(\frac{1}{2} \vec{V}^2 + c_p T + \phi \right)_R \exp\left(\frac{-z}{H}\right) \Delta z \right] dS \\ = \iint_S \frac{P_*}{H} w^* \left(\frac{1}{2} \vec{V}^2 + c_p T + \phi \right)_R dS. \end{aligned} \quad (109)$$

The total energy for the entire model is then described by the summation of (108) and (109). This implies that total energy is conserved only if

$$\iint_S P_* \sigma \left(\frac{1}{2} \vec{V}^2 + c_p T + \phi \right)_R dS + \iint_S \frac{P_*}{H} w^* \left(\frac{1}{2} \vec{V}^2 + c_p T + \phi \right)_R dS = 0. \quad (110)$$

Since it follows from (4), (42), and (53) that $P_* \sigma \dot{R} = -w^* \frac{P_*}{H} \dot{S}$,

equation (110) does indeed hold and total energy is conserved throughout the entire model.

2.4 Semi-implicit Time Differencing Preliminaries

Time derivatives are predominantly computed via semi-implicit time differencing. This method slows high frequency waves that would otherwise limit the size of the time step required for integration of the prognostic equations. Robert (1969) estimated that the semi-implicit time method can use a time step 6 times that of a fully explicit time differencing scheme.

Similar to Hoskins and Simmons (1975), we can write the finite difference analogs for the divergence equation (32), the thermodynamic equation (67), the continuity equation (70) and the hydrostatic equations (74b) and (75) in matrix form as follows:

$$\partial[D]/\partial t = [D] - \nabla^2([\phi'] + R\bar{T}[q]) + K_h \frac{\nabla^2 D + 2(D_e)}{a^2} ; \quad (111)$$

$$\partial[T']/\partial t = [T] - \tau[D] + K_h \frac{\nabla^2 (T' - T_e)}{a^2} ; \quad (112)$$

$$\partial[q]/\partial t = [P] - \pi[D] ; \quad (113)$$

$$[\phi' - \phi'_*] = R\gamma[T'] . \quad (114)$$

where [] in the above equations indicates a column vector of length 31 corresponding to the prognostic levels. If we let i be the row index, we have the following correspondence

$i = 1$	\rightarrow	$K = \frac{1}{2}$
$i = 2$	\rightarrow	$K = 1\frac{1}{2}$
$i = 3$	\rightarrow	$K = 2\frac{1}{2}$
.		
.		
.		
$i = 26$	\rightarrow	$K = 25\frac{1}{2}$
$i = 27$	\rightarrow	$r = \frac{1}{2}$
$i = 28$	\rightarrow	$r = 1\frac{1}{2}$
.		
.		
.		
$i = 31$	\rightarrow	$r = 4\frac{1}{2}$.

$\{\bar{T}\}$ is a 31×31 matrix composed of zeroes everywhere except for \bar{T}_r values on the lower right diagonal positions. τ is a 31×31 matrix composed of terms, constant in time, which multiply divergence to produce temperature tendency. π is a 31×31 matrix that contains all direct effects of means on tropospheric log-pressure tendency. γ is a 31×31 matrix composed of $\Delta z/H$ and α terms used to compute geopotential hydrostatically. Note that γ includes the averaging process and the resulting ϕ' values of (111 - 114) are prognostic level values.

If we let j be a summation index for the vector terms $[D]$, $[T]$, and $[P]$, which corresponds to the model levels as does i , then we can define these more complex vectors of equations (111 - 114) using i and j in place of K or r as the level indicators. For example, $i = 28$ really means $r = 1\frac{1}{2}$ and so on. Hence, we have

$$D_i = \begin{cases} \frac{1}{2} \left[\frac{\partial \hat{B}_i}{\partial \lambda} - \cos \phi \frac{\partial \hat{A}_i}{\partial \phi} \right] - \nabla^2 E_i & (i < 26) \\ \frac{1}{a \cos \phi} & \\ \frac{1}{2} \left[\frac{\partial B_i}{\partial \lambda} - \cos \phi \frac{\partial A_i}{\partial \phi} \right] - \nabla^2 E_i & ; \quad (i > 26) \\ \frac{1}{a \cos \phi} & \end{cases} \quad (115)$$

$$T_i = \begin{cases} \frac{-1}{a \cos^2 \phi} \left[\frac{\partial (UT')}{\partial \lambda} i + \cos \phi \frac{\partial (VT')}{\partial \phi} i \right] + \tilde{H}_K & (i < 26) \\ \frac{-1}{2} \left[\frac{\partial (UT')}{\partial \lambda} i + \cos \phi \frac{\partial (VT')}{\partial \phi} i \right] + \tilde{H}_r, \quad (i > 26) \\ \frac{-1}{a \cos \phi} & \end{cases} \quad (116)$$

where

$$\tilde{H}_K = D_i T_i + \alpha(z_i) (T_i' - T_i) - \frac{RT_i}{2cH} \left(w_{i+\frac{1}{2}}^* + w_{i-\frac{1}{2}}^* \right) \exp\left(\frac{z_i}{H}\right)$$

$$- \frac{\exp\left(\frac{z_i}{H}\right)}{2\Delta z} \left[w_{i+\frac{1}{2}}^* (T_{i+1}' - T_i') + w_{i-\frac{1}{2}}^* (T_i' - T_{i-1}') \right],$$

$$\tilde{H}_r = D_i T_i + \alpha(z_i) (T_i' - T_i) + v^F T_i - \frac{1}{2\Delta\sigma} \left[\dot{\sigma}_{i+\frac{1}{2}} (T_{i+1}' - T_i') + \dot{\sigma}_{i-\frac{1}{2}} (T_i' - T_{i-1}') \right]$$

$$- \frac{(\bar{T}_{i+1} - \bar{T}_i)}{2p_*} \left[\sigma_{i+\frac{1}{2}} \sum_{j=27}^{31} (\vec{V}_j \cdot \vec{\nabla p}_*) \right] - \sum_{j=27}^i (\vec{V}_j \cdot \vec{\nabla p}_*) + \frac{p_* \delta'}{\Delta\sigma} (\sigma_{i+\frac{1}{2}} - 1) \frac{w_p p}{H R}$$

$$\begin{aligned}
 & - \frac{(\bar{T}_i - \bar{T}_{i-1})}{2p_*} \left[\sigma_{i-\frac{1}{2}} \sum_{j=27}^{31} (\vec{V}_j \cdot \vec{\nabla} p_*) - \sum_{j=27}^{i-1} (\vec{V}_j \cdot \vec{\nabla} p_*) + \frac{p_* \delta'}{\Delta \sigma} (\sigma_{i-\frac{1}{2}} - 1) \frac{w_R p_R}{H} \right] \\
 & - \frac{RT'_i}{c(p_i p_* + p_R)} \left[\frac{\Delta \sigma}{2} \sum_{j=27}^i (p_* D_j + \vec{V}_j \cdot \vec{\nabla} p_*) + \frac{\Delta \sigma}{2} \sum_{j=27}^{i-1} (p_* D_j + \vec{V}_j \cdot \vec{\nabla} p_*) - \sigma_i \vec{V}_i \cdot \vec{\nabla} p_* + \frac{w_R p_R}{H} \right] \\
 & - \frac{RT'_i}{c(p_i p_* + p_R)} \left[\frac{\Delta \sigma}{2} \sum_{j=27}^i \vec{V}_j \cdot \vec{\nabla} p_* + \frac{\Delta \sigma}{2} \sum_{j=27}^{i-1} \vec{V}_j \cdot \vec{\nabla} p_* - \sigma_i \vec{V}_i \cdot \vec{\nabla} p_* + p_* \delta' \frac{w_R p_R}{H} \right] \\
 & - \frac{RT'_i}{c(p_i p_* + p_R)} \beta'_i \left[\frac{\Delta \sigma}{2} \sum_{j=27}^i D_j + \frac{\Delta \sigma}{2} \sum_{j=27}^{i-1} D_j + \bar{\delta} \frac{w_R p_R}{H} \right];
 \end{aligned}$$

$$p_i = \begin{cases} 0 & (i < 26) \\ \frac{-\sigma_i}{\sigma_i p_* + p_R} \left[\sum_{j=27}^{31} \vec{V}_j \cdot \vec{\nabla} p_* \Delta \sigma + p_* \delta' \frac{w_R p_R}{H} \right] & (i > 26) \end{cases} \quad (117)$$

$$- \sigma_i \beta'_i \left[\sum_{j=27}^{31} D_j \Delta \sigma + \bar{\delta} \frac{w_R p_R}{H} \right].$$

Next, we can use j as the column indicator for the matrices in (111 - 114), corresponding to the model levels similar to i , to define

$$\tau_{ij} = (HN^2 \Delta z / R) \left[\begin{array}{c|c} \frac{1}{2}(i = j < 26) & \exp\left[\frac{-(j-i)\Delta z}{H}\right] (i < j < 26) \\ \hline 0 \text{ (elsewhere)} & 0 \text{ (elsewhere)} \end{array} \right]$$

$$+ \left[\begin{array}{c|c} \frac{1}{2}\exp\left[\frac{-(j-1)\Delta z}{H}\right] & (i=27, j < 26) \\ \hline 0 \text{ (elsewhere)} & \end{array} \right]$$

$$+ \frac{(\bar{T}_{i+1} - \bar{T}_i)}{2} \left[\begin{array}{c|c} \sigma_{i+\frac{1}{2}} (31 > i > 26, j > 26) & 1 (31 > i > j > 26) \\ \hline 0 \text{ (elsewhere)} & 0 \text{ (elsewhere)} \end{array} \right]$$

$$+ \left[\begin{array}{c|c} \frac{\delta(\sigma_{i+\frac{1}{2}} - 1)}{\Delta \sigma} \frac{p_R}{H} \Delta z \exp\left[\frac{-(j-1)\Delta z - (\Delta z/2)}{H}\right] & (26 < i < 31, j < 26) \\ \hline 0 \text{ (elsewhere)} & \end{array} \right]$$

$$+ \frac{(\bar{T}_i - \bar{T}_{i-1})}{2} \left[\begin{array}{c|c} \sigma_{i-\frac{1}{2}} (i > 27, j > 26) & 1 (i-1 > j > 26) \\ \hline 0 \text{ (elsewhere)} & 0 \text{ (elsewhere)} \end{array} \right]$$

$$+ \left[\begin{array}{c|c} \frac{\delta(\sigma_{i-\frac{1}{2}} - 1)}{\Delta \sigma} \frac{p_R}{H} \Delta z \exp\left[\frac{-(j-1)\Delta z - (\Delta z/2)}{H}\right] & (i > 27, j < 26) \\ \hline 0 \text{ (elsewhere)} & \end{array} \right]$$

$$\begin{aligned}
 & + \frac{R\bar{T}_i}{c_p} \bar{\beta}_i \Delta\sigma \left[\begin{array}{c|c|c}
 .5 (27 < i > j > 26) & .5 (i-1 > j > 26) & .25 (i=j=27) \\
 0 (\text{elsewhere}) & 0 (\text{elsewhere}) & 0 (\text{elsewhere}) \\
 \hline
 \end{array} \right. \\
 & \left. + \begin{array}{c|c}
 -\frac{p_R}{H} \frac{\Delta z}{\Delta\sigma} \exp\left[\frac{-(j-1)\Delta z - (\Delta z/2)}{H}\right] & (i > 27, j < 26) \\
 -\frac{1}{2} \frac{p_R}{H} \frac{\Delta z}{\Delta\sigma} \exp\left[\frac{-(j-1)\Delta z - (\Delta z/2)}{H}\right] & (i=27, j < 26) \\
 0 (\text{elsewhere}) &
 \end{array} \right]; \quad (118)
 \end{aligned}$$

$$\begin{aligned}
 \pi_{ij} = & \left[\begin{array}{c|c}
 \sigma_i \bar{\beta}_i \Delta\sigma & (i > 26, j > 26) \\
 0 (i < 26, j) & \\
 0 (\text{elsewhere}) &
 \end{array} \right. \\
 & \left. + \begin{array}{c}
 \sigma_i \bar{\beta}_i \frac{p_R}{H} \frac{\Delta z}{\Delta\sigma} \exp\left[\frac{-(j-1)\Delta z - (\Delta z/2)}{H}\right] & (i > 26, j < 26) \\
 0 (\text{elsewhere}) &
 \end{array} \right] \quad (119)
 \end{aligned}$$

$$\begin{aligned}
 \gamma_{ij} = & \frac{\Delta z}{H} \left[\begin{array}{c|c}
 .5 (i=j < 26) & 1 (i > j < 26) \\
 0 (\text{elsewhere}) & 0 (\text{elsewhere}) \\
 \hline
 \end{array} \right. \\
 & \left. + \begin{array}{c|c|c}
 \alpha_j (i < 26, j > 26) & .5 \alpha_j (i=j > 26) & \alpha_j (i < j > 26) \\
 0 (\text{elsewhere}) & 0 (\text{elsewhere}) & 0 (\text{elsewhere}) \\
 \hline
 \end{array} \right] \quad (120)
 \end{aligned}$$

Using the semi-implicit scheme of Robert et al., (1972), we define the following notation:

$$\delta_t X \equiv \frac{X^{t+\Delta t} - X^{t-\Delta t}}{2\Delta t}, \quad (121)$$

$$\bar{X}^t \equiv \frac{X^{t+\Delta t} + X^{t-\Delta t}}{2}, \quad (122)$$

where the superscript represents the time step. Using (121) and (122), we can express prognostic expression (111 - 113) in semi-implicit form as follows:

$$\delta_t [D] = [D] - \nabla^2 ([\phi'])^t + R[\bar{T}][q]^t + K_h [\nabla^2 D + 2(D/a^2)]^{t-\Delta t}; \quad (123)$$

$$\delta_t [T'] = [T] - \tau[D]^t + K_h [\nabla^2 (T' - T')]^{t-\Delta t}; \quad (124)$$

$$\delta_t [q] = [P] - \pi[D]^t. \quad (125)$$

Since we can rearrange (121) and (122) to obtain

$$\bar{X}^t = X^{t-\Delta t} + \Delta t \delta_t X; \quad (126)$$

$$\delta_t X = \frac{\bar{X}^t - X^{t-\Delta t}}{\Delta t}, \quad (127)$$

we can substitute using (126) and (127) to express (123) as follows:

$$\frac{\overline{[D]}_t - [D]}{\Delta t} = [D] - \nabla^2 ([\phi'])^{t-\Delta t} + \Delta t \delta_t [\phi'] + R \bar{T} [q]^{t-\Delta t} + \Delta t R \bar{T} \delta_t [q] + K_h^2 [\nabla^2 D + 2(D/a^2)]^{t-\Delta t}. \quad (128)$$

Before we can proceed further, we need to develop an expression for $\delta_t [\phi']$. First, we take the continuous time derivative of (114), which yields

$$\frac{\partial [\phi']}{\partial t} = \frac{\partial [\phi_*']}{\partial t} + R \gamma \frac{\partial [T']}{\partial t} + R \frac{\partial \gamma}{\partial t} [T']. \quad (129)$$

In order to compute $\partial \gamma / \partial t$, we need to be able to compute $\frac{\partial \alpha}{\partial t}$. From the definition of α_r given by (85), we can write

$$\frac{\partial \alpha_r}{\partial t} = \frac{\partial}{\partial t} [\ln(\sigma_{r+\frac{1}{2}} \frac{p_* + p_R}{r+\frac{1}{2}}) - \ln(\sigma_{r-\frac{1}{2}} \frac{p_* + p_R}{r-\frac{1}{2}})]. \quad (130)$$

Differentiating the right side of (130) yields

$$\frac{\partial \alpha_r}{\partial t} = \left(\frac{\sigma_{r+\frac{1}{2}}}{\sigma_{r+\frac{1}{2}} \frac{p_* + p_R}{r+\frac{1}{2}}} - \frac{\sigma_{r-\frac{1}{2}}}{\sigma_{r-\frac{1}{2}} \frac{p_* + p_R}{r-\frac{1}{2}}} \right) \frac{\partial p_*}{\partial t}. \quad (131)$$

Substitutions of the discrete form of (44) for $\frac{\partial p_*}{\partial t}$ in (131), allows us to write

$$\frac{\partial \alpha_r}{\partial t} = \left(\frac{\sigma_{r+\frac{1}{2}}}{\sigma_{r+\frac{1}{2}} \frac{p_* + p_R}{r+\frac{1}{2}}} - \frac{\sigma_{r-\frac{1}{2}}}{\sigma_{r-\frac{1}{2}} \frac{p_* - p_R}{r-\frac{1}{2}}} \right) \left[\frac{-w_R p_R}{H} - \sum_{s=\frac{1}{2}}^{4\frac{1}{2}} \left(\frac{p_* D}{s} + \frac{V}{s} \cdot \frac{\nabla p_*}{s} \right) \Delta \sigma \right]. \quad (132)$$

Since all the other terms of γ are either zero or constant in time, the only remaining terms of $\partial\gamma/\partial t$ involve $\partial\alpha_r/\partial t$ which can be expressed diagnostically by (132).

If we define

$$\Gamma \equiv \frac{\partial\gamma}{\partial t} ; \quad (133)$$

$$\gamma \equiv \bar{\gamma}(\sigma) + \gamma' , \quad (134)$$

we can express (129) as follows:

$$\frac{\partial[\phi']}{\partial t} \frac{\partial[\phi_*']}{\partial t} + R\gamma' \frac{\partial[T']}{\partial t} + R\bar{\gamma} \frac{\partial[T']}{\partial t} + R\Gamma [T'] . \quad (135)$$

If we compute $\partial[T']/\partial t$ for the second term on the right of (135) by computing the right side of (112) directly and call this value $[\theta]$, then we can express (135) in discrete form as follows:

$$\delta_t[\phi'] = \delta_t[\phi_*'] + R\gamma'[\theta] + R\bar{\gamma}\delta_t[T'] + R\Gamma[T'] . \quad (136)$$

Substituting (124) for $\delta_t[T']$ in (136) and substituting (136) for $\delta_t[\phi']$ in (128) and substituting (125) in (128) yields

$$\begin{aligned} & \{ I - R\Delta t^2 (\bar{\gamma}_T + \{\bar{T}\}\pi) \nabla^2 \} \overline{[D]}^T \\ &= [D]^{t-\Delta t} + \Delta t \{ [D] - \nabla^2 ([\phi']^{t-\Delta t} + R\{\bar{T}\}[q]^{t-\Delta t}) \} \\ & - \Delta t^2 \nabla^2 \{ \delta_t[\phi_*'] + R(\gamma'[\theta] + R[T'] + \bar{\gamma}[T] + \{\bar{T}\}[P] + \bar{\gamma}K_h[\nabla^2(T' - T'_e)]^{t-\Delta t}) \} \end{aligned}$$

$$+ \Delta t \frac{2}{h} [V^2 D + 2(D/a^2)]^{t-\Delta t}, \quad (137)$$

where I is the identity matrix. With the spectral representation to be introduced in the next section, we will be able to solve (137) for $[D]^t$ and subsequently solve for $[D]^{t+\Delta t}$, $[T']^{t+\Delta t}$, and $[q]^{t+\Delta t}$.

2.5 Spherical Harmonic Representation

Except for vertical derivatives and the computation of non-linear terms, which are formed at grid points, other model computations are handled spectrally. The variables ψ , x , ϕ' , U , V , P_* , T' and q can be expanded in terms of spherical harmonics as follows:

$$\{\psi, x, \phi'\} = a \sum_{m=-J}^{+J} \sum_{\ell=|m|}^{|m|+L} \{\psi_{\ell}^m, x_{\ell}^m, \phi_{\ell}^m\} Y_{\ell}^m; \quad (138)$$

$$\{U, V\} = a \sum_{m=-J}^{+J} \sum_{\ell=|m|}^{|m|+L+1} \{U_{\ell}^m, V_{\ell}^m\} Y_{\ell}^m; \quad (139)$$

$$\{P_*\} = a \sum_{m=-J}^{+J} \sum_{\ell=|m|}^{|m|+L} \{P_*^m\} Y_{\ell}^m; \quad (140)$$

$$\{T', q\} = \sum_{m=-J}^{+J} \sum_{\ell=|m|}^{|m|+L} \{T_{\ell}^m, q_{\ell}^m\} Y_{\ell}^m, \quad (141)$$

where

$$Y_{\ell}^m = P_{\ell}^m(\mu) e^{im\lambda}, \quad (142)$$

$$\mu = \sin \phi. \quad (143)$$

$P_l^m(\mu)$ is an associated Legendre polynomial normalized to unity with m , the longitudinal wavenumber, and l , the latitudinal index. L determines the limit of the parallelogramic truncation. The $\{ \}$ terms on the right of (138 - 141) represent the respective spherical harmonic coefficients. J is the longitudinal wavenumber truncation.

After the vertical derivatives and non-linear products have been formed at grid points, the resulting terms can be transformed in terms of Fourier series as follows:

$$\{Z, D, T, P, \gamma'[\theta], \Gamma[T']\} = \sum_{m=-J}^{+J} \{Z_m, D_m, T_m, P_m, \theta_m, \kappa_m\} e^{im\lambda} \quad (144)$$

where the m subscript represents the respective Fourier coefficient.

The Legendre transform defined by

$$()_l^m = \int_{-\pi/2}^{\pi/2} ()_m^m P_l^m(\mu) \cos\phi \, d\phi \quad (145)$$

can be applied to the Fourier coefficients in (144) to obtain the appropriate spherical harmonic coefficients. Since in the model, the Fourier series defined by (144) are formed at Gaussian latitudes, (145) can be computed exactly for each term up to the point of truncation.

One of the most important advantages in using spherical harmonics is that horizontal derivatives can be computed accurately and easily. The following derivative properties result from using spherical harmonics:

$$\frac{\partial Y_l^m}{\partial \lambda} = i m Y_l^m; \quad (146)$$

$$\cos \phi \frac{\partial p^m(\mu)}{\partial \phi} = (\ell+1) \varepsilon_{\ell}^m p_{\ell-1}^m(\mu) - \ell \varepsilon_{\ell+1}^m p_{\ell+1}^m(\mu); \quad (147)$$

$$\nabla^2 Y_{\ell}^m = \frac{-\ell(\ell+1)}{a^2} Y_{\ell}^m \quad (148)$$

where

$$\varepsilon_{\ell}^m = \sqrt{(\ell-m^2)/(4\ell^2-1)} \quad (149)$$

From (18), (19), (138), (139), (146) and (147), it follows that

$$U_{\ell}^m = (\ell-1) \varepsilon_{\ell}^m \psi_{\ell-1}^m - (\ell+2) \varepsilon_{\ell+1}^m \psi_{\ell+1}^m + im x_{\ell}^m, \quad (150)$$

$$V_{\ell}^m = -(\ell-1) \varepsilon_{\ell}^m x_{\ell-1}^m + (\ell+2) \varepsilon_{\ell+1}^m x_{\ell+1}^m + im \psi_{\ell}^m. \quad (151)$$

From (12), (13), (138), (139), and (148), we also obtain spectral expressions for vorticity and divergence as follows:

$$S_{\ell}^m = -\ell(\ell+1) \psi_{\ell}^m, \quad (152)$$

$$D_{\ell}^m = -\ell(\ell+1) x_{\ell}^m. \quad (153)$$

All horizontal derivatives in this model are computed spectrally using (146 - 148). These computations are exact up to the point of

truncation, a significant advantage over grid point methods.

Using the spectral relationships outlined so far in this section, we can write (27), (111 - 113) as the following spectral equations:

$$\frac{\partial [S^m_\ell]}{\partial t} = [Z^m_\ell] + \frac{K}{2} \frac{h}{a} \{-\ell(\ell+1)+2\} [S^m_\ell - S^m_{e\ell}] \quad (154)$$

$$\begin{aligned} \frac{\partial [D^m_\ell]}{\partial t} = & [D^m_\ell] + \ell(\ell+1) ([\Phi^m_\ell] + \frac{R}{a^2} \{\bar{T}\} [q^m_\ell]) \\ & + \frac{K}{2} \frac{h}{a} \{-\ell(\ell+1)+2\} [D^m_\ell] \end{aligned} \quad (155)$$

$$\frac{\partial [T^m_\ell]}{\partial t} = [T^m_\ell] - \tau [D^m_\ell] - \frac{K}{a^2} \ell(\ell+1) [T^m_\ell - T^m_{e\ell}] \quad (156)$$

$$\frac{\partial [q^m_\ell]}{\partial t} = [P^m_\ell] - \pi [D^m_\ell], \quad (157)$$

while the [] represents a column vector as defined in the previous section. Note that the hydrostatic equation is treated discretely and geopotential values computed from (114) are then transformed for input to the spectral divergence equation.

2.6 Conclusion of Semi-implicit Differencing

In spectral form using relationships developed in the previous section, we can express (137) as follows:

$$\begin{aligned}
& \{I + \frac{R\Delta t}{a^2} \zeta(\zeta+1)(\bar{Y}\tau + \bar{T}\pi)\} \overline{[D_\zeta^m]_t} \\
&= [D_\zeta^m]^{t-\Delta t} + \Delta t \{ [D_\zeta^m] + \zeta(\zeta+1) ([\phi_\zeta^m]^{t-\Delta t} + \frac{R\bar{T}}{a^2} [q_\zeta^m]^{t-\Delta t}) \} \\
&+ \Delta t^2 \zeta(\zeta+1) \{ \frac{(\phi_{*\zeta}^m)^{t+\Delta t} - (\phi_{*\zeta}^m)^{t-\Delta t}}{2\Delta t} \\
&+ \frac{R}{2} ([\theta_\zeta^m] + [\kappa_\zeta^m] + \bar{Y}[T_\zeta^m] + \{\bar{T}\}[P_\zeta^m] \\
&- \bar{Y} \frac{K}{a^2} \zeta(\zeta+1) [T_\zeta^m - T_{\zeta+1}^m]^{t-\Delta t}) \} + \Delta t \frac{K}{a^2} \{ -\zeta(\zeta+1)+2 \} (D_\zeta^m)^{t-\Delta t}. \quad (159)
\end{aligned}$$

According to Hoskins and Simmons (1975), an equation of the form of (159) is essentially a gravity wave equation. We may invert the matrix

$$M \equiv \{I + \frac{R\Delta t}{a^2} \zeta(\zeta+1)(\bar{Y}\tau + \bar{T}\pi)\}, \quad (160)$$

since $(\bar{Y}\tau + \bar{T}\pi)$ has positive eigenvalues. Since M is constant in time, M^{-1} needs only to be calculated once before the start of prognostic integrations. Hence, we can solve for $\overline{[D_\zeta^m]_t}$ on the left side of (159).

Using this value of $\overline{[D_\zeta^m]_t}$, we can compute $[D_\zeta^m]^{t-\Delta t}$ from (122), $[T_\zeta^m]^{t+\Delta t}$ and $[q_\zeta^m]^{t+\Delta t}$ from the spectral equivalents of (124) and (125), i.e., we have

$$[D_{\ell}^m]^{t+\Delta t} = \overline{[D_{\ell}^m]_t} - [D_{\ell}^m]^{t-\Delta t}; \quad (161)$$

$$\begin{aligned} [T_{\ell}^m]^{t+\Delta t} &= [T_{\ell}^m]^{t-\Delta t} + 2\Delta t \{ [T_{\ell}^m] - \overline{[D_{\ell}^m]_t} \\ &\quad - \frac{K}{2} \frac{h}{a} \ell(\ell+1) ([T_{\ell}^m]^{t-\Delta t} - [T_{\ell}^m]_{\ell}) \}; \end{aligned} \quad (162)$$

$$[q_{\ell}^m]^{t+\Delta t} = [q_{\ell}^m]^{t-\Delta t} + 2\Delta t \{ [P_{\ell}^m] - \overline{[D_{\ell}^m]_t} \}. \quad (163)$$

Since we cannot include the vorticity equation in the semi-implicit scheme since it is not related to divergence, we use centered time differencing of (154) with direct solution as follows:

$$\begin{aligned} [S_{\ell}^m]^{t+\Delta t} &= [S_{\ell}^m]^{t-\Delta t} + 2\Delta t \{ [Z_{\ell}^m] \\ &\quad + \frac{K}{2} \frac{h}{a} \{-\ell(\ell+1)+2\} ([S_{\ell}^m]^{t-\Delta t} - [S_{\ell}^m]_{\ell}) \}. \end{aligned} \quad (164)$$

Equations (161 - 164) yield prognostic values for D_{ℓ}^m , T_{ℓ}^m , q_{ℓ}^m , and S_{ℓ}^m from which we can compute new values of ψ_{ℓ}^m and X_{ℓ}^m from (152 - 153) and in turn compute U_{ℓ}^m and V_{ℓ}^m from expressions (150 - 151). We, then, can construct real values for D , ζ , T' , U , V , and q from the spectral coefficients and subsequently compute p_* and hydrostatically compute Φ .

2.7 Modified Euler Backward Scheme

In order to start model integrations from an initial state, we use the modified Euler backward time differencing scheme after Kurihara (1965). If we let X represent any prognostic variable and Y represent the right side of the prognostic equation, i.e.,

$$\partial X / \partial t = Y , \quad (165)$$

we can represent the three steps of this iterative process as follows;

$$\text{Step 1: } X^{(t+\frac{\Delta t}{2})} = X^t + \frac{\Delta t}{2} Y^t , \quad (166)$$

$$\text{Step 2: } X^{(t+\Delta t)*} = X^t + \Delta t Y^{(t+\frac{\Delta t}{2})} , \quad (167)$$

$$\text{Step 3: } X^{(t+\Delta t)} = X^t + \Delta t Y^{(t+\Delta t)*} . \quad (168)$$

This method of time differencing is applied directly to the spectral equations (154 - 158). Since the scheme is a damping one horizontal diffusion terms are neglected when it is used. The modified Euler backward scheme also removes any computational modes generated from centered time differencing (Haltiner, 1971) and consequently is interspersed every 37 time steps in place of the semi-implicit scheme.

CHAPTER 3

SPECIFICATION

3.1 Model Initialization

Initial fields of geopotential, temperature, stream function and log-pressure must be specified before the start of model integrations. For these initial conditions, we specify zonal profiles that are non-divergent and essentially have a non-divergent tendency. These latter conditions are essential so that high frequency oscillations, which could adversely affect the model's behavior, are basically eliminated. In this section, we will describe the initialization process used to produce the initial profiles used in this model.

Our goal initially was to use the initial conditions of Lordi (1978) for the upper portion of the model, since they met the criteria specified above. However, any realistic tropospheric fields, built to match these conditions, resulted in convectively unstable conditions at the interface between the models near the equator and some alterations had to be made. By subsequently adjusting the initial temperature deviations in the lowest three levels of the stratosphere south of 45N, we were able to obtain a temperature field that was convectively stable and also climatologically more agreeable.

To arrive at a balanced state in the troposphere, we initially started with constant pressure level zonal temperature deviations

from level means, based on January climatic tables from Oort and Rasmusson (1972). Data for polar latitudes were extrapolated from January 1974 and 1976 data from National Meteorological Center (NMC) observational grids. The above temperature fields, which were specified at 5° latitude increments, were first linearly interpolated to Gaussian latitudes used in the model. Using Lordi's original lower boundary geopotential deviation values as an upper boundary condition, we integrated hydrostatically downward to obtain geopotential at intermediate pressure levels to a pre-selected constant pressure surface, denoted \bar{p}_* , which corresponds to the mean surface pressure at our $\sigma = 1$ level. By assuming T to be constant ($\equiv T_*$) with height near this surface, we can integrate the hydrostatic equation from p_* , the actual surface pressure, to \bar{p}_* and obtain

$$\ln(p_*/\bar{p}_*) = - \frac{1}{RT_*} (\Phi_{p_*} - \Phi_{\bar{p}_*}) . \quad (169)$$

Now let $\Phi_{p_*} = \bar{\Phi}_{p_*} + \Phi'_{p_*}$ and $\Phi_{\bar{p}_*} = \bar{\Phi}_{\bar{p}_*} + \Phi'_{\bar{p}_*}$, where the bar denotes a layer, mean, and assuming that $\bar{\Phi}_{p_*} = \bar{\Phi}_{\bar{p}_*}$, and $\Phi'_{p_*} = 0$, corresponding to a flat surface, we obtain

$$p_* = \bar{p}_* \exp(\Phi'_{\bar{p}_*}/RT_*) , \quad (170)$$

where temperature values were determined by interpolation.

Using the resulting p_* , we can compute the pressure corresponding to the five tropospheric prognostic levels. Next, we interpolate the constant pressure level temperatures to these sigma levels and integrate hydrostatically downward in the sigma system from the interface

boundary geopotential used previously to obtain geopotentials at diagnostic levels of the troposphere. However, because of interpolation, the surface geopotential that resulted from this integration was not identically zero as desired. We force this solution by redistributing the differential at the surface logarithmically to higher levels and adjust the temperatures at prognostic levels to maintain hydrostatic balance. These temperatures now allow us to integrate the hydrostatic equation upwards as is done in the model and obtain boundary geopotentials identical to Lordi's.

Averaging the diagnostic level geopotentials to obtain prognostic level values as is done in the model and using the corresponding temperature and pressure fields, we can then quadratically solve the gradient wind balance equation for our σ -coordinate system

$$u(f + \frac{u \tan \phi}{a}) = - \frac{1}{a} \frac{\partial \phi'}{\partial \phi} - \frac{\sigma R(\bar{T} + T')}{\sigma P_* + p_R} \frac{1}{a} \frac{\partial P_*}{\partial \phi} , \quad (171)$$

for the zonal velocity field u . The mean temperature profile \bar{T} is assumed to be that of the standard atmosphere at 45°N.

Since reflective symmetry across the equator is assumed, the resulting zonal wind field may be expanded at prognostic levels in terms of the following series:

$$u(\phi, \sigma) = \sum_{r=1, R, 2} A_r(\sigma) \cos r\phi , \quad (172)$$

where $R = 33$ and

$$A_r(\sigma) = \frac{4}{\pi} \int_0^{\pi/2} u(\phi, \sigma) \cos r\phi \, d\phi , \quad (173)$$

satisfying the boundary conditions that

$$u(\pm \pi/2, \sigma) = 0. \quad (174)$$

Integration of (173) was performed numerically using a Simpson's rule adaption for unequally spaced arguments.

Since horizontal divergence is assumed to be zero, it follows from the continuity equation that

$$(\partial \psi / \partial \phi) = - a \sum_{r=1, R, 2} A_r(\sigma) \cos r\phi, \quad (175)$$

which can be integrated assuming a boundary condition that $\psi(0, \sigma) = 0$ to yield

$$\psi(\phi, \sigma) = - a \sum_{r=1, R, 2} A_r(\sigma) \frac{\sin r\phi}{r} \quad (176)$$

We can then transform the resulting ψ from (176) to obtain initial ψ^m_ℓ fields for the troposphere.

Following the model procedures, we can determine U and ζ from ψ^m_ℓ . We also compute the spectral coefficients ϕ^m_ℓ , T^m_ℓ , and q^m_ℓ for geopotential, temperature, and log-pressure, respectively. Assuming D^m_ℓ is zero and neglecting diffusion and friction, the divergence tendency equation (156) can be solved to yield spectral divergence tendencies on the order of 10^{-10} to 10^{-15} . In order to reduce this tendency even further, we set $\partial D^m_\ell / \partial t$ to zero and solve (156) for ϕ^m_ℓ . We then compute ϕ from the coefficients and compute T' hydrostatically after reversing the averaging process and obtaining diagnostic level geopotential fields. Transforming T' to T^m_ℓ and back to T' , we then

recompute ϕ at diagnostic levels, average ϕ to obtain prognostic level values and then compute ϕ_l^m . We then solve (156) for divergence tendency and again compute a ϕ_l^m to make this tendency zero. We then continued with the remainder of the process outlined above and iteratively continued this process six times until apparent convergence was reached, yielding divergence tendencies on the order of 10^{-14} to 10^{-18} . This was considered sufficiently small so that any initial imbalance would not unduly influence model integrations.

As mentioned earlier, this initialization procedure resulted in convectively unstable conditions at the interface. The boundary level geopotential also no longer exactly matched that of Lordi's because of the above balancing process. Both conditions mandated changes from Lordi's initial conditions. To initialize the upper model levels, we started with Lordi's initial temperature distribution and restructured the temperatures at the lowest three levels at lower latitudes in keeping with observational data and this resulted in a convectively stable situation.

Using the new temperature profile, we then integrated hydrostatically as in the model using the boundary geopotential that results from the tropospheric formulation to obtain diagnostic level geopotentials which were averaged to prognostic levels. Using the gradient balance equation for the upper portion of the model, we solve

$$u(f + \frac{u \tan \phi}{a}) = - \frac{1}{a} \frac{\partial \phi'}{\partial \phi} \quad (177)$$

quadratically for u and can proceed as with the troposphere in

obtaining an initial stream function field. We then can solve (156) for the stratosphere and obtain divergence tendencies on the order 10^{-11} to 10^{-14} . Computing a residual ϕ_{λ}^m as with the troposphere, we can find a corresponding T_{λ}^m field from the hydrostatic relationship yielding tendencies on the order of 10^{-25} or nearly zero. This balance is more effective in the stratosphere, since (177) involves only a balance between u and ϕ , whereas (171) also involves P_* , \bar{T} and T' .

The above analysis yielded initial fields for ϕ_{λ}^m , T_{λ}^m , ψ_{λ}^m and q_{λ}^m that are essentially non-divergent and possess negligible divergence tendency. The zonal wind and temperature profiles for this case, which we will denote as Case 1 are depicted in Figures 2a and 3a, respectively. The upper part of these profiles matches Lordi's to a high degree.

We also wanted to examine the case, denoted, Case 2, which had a much stronger polar vortex in the stratosphere and mesosphere. Using the same troposphere as in Case 1, we adjusted the upper model temperatures by the following factor:

$$T'_{\text{CASE 2}} = T'_{\text{CASE 1}} \left[1 + \left(1 - \exp\left\{ -\frac{(K-1/2)}{2.6} \right\} \right) \right], \quad (178)$$

where K represents the stratospheric level index. This formulation essentially doubles temperature deviations at levels, six and higher, above the interface and increases more gradually the intermediate levels just above the interface. Using these temperatures, we can then initialize for Case 2 using exactly the same upper model initialization as Case 1. Initial zonal wind and temperature fields for Case 2

are depicted in Figures 2b and 3b.

Mean layer values for geopotential, $\bar{\Phi}$, although not required in stratospheric computations, are required in the troposphere to compute height fields used in vertical differencing as in (80); to compute temperature lapse rates for use in convective adjustment procedures to be discussed later in this chapter; and to interpolate σ -level fields to constant height levels for display purposes. These values were computed by using $\bar{\Phi}_{p_*}$ as a bottom boundary and standard atmosphere temperatures for 45N, integrating similar to (84) and center averaging the result to the prognostic levels.

3.2 Orographic Forcing

Surface geopotential must be specified as a lower boundary condition in the model. It is required by the hydrostatic equation (114) and the semi-implicit divergence equation (159). As mentioned in the last section, initial conditions were based on the assumption of a flat surface at the lower boundary. We tested the model and the balanced state of these conditions by keeping the surface unchanged; neglecting friction, diffusion, and heating/cooling; and integrating the model for 10 days. During this period, divergence increased only slightly and the initial zonal fields remained virtually unchanged, indicating the equilibrium state of the initial fields and the capability of the model to maintain them in the absence of external forcing. However, our interests are on the effects of orographic forcing on the troposphere and stratosphere. In order to study these effects, we slowly introduce terrain features at the lower boundary

which are reflected in geopotential deviations at the surface that force the model levels above.

We assumed a very idealistic and simplistic topographic pattern to simulate the continental land mass distribution of the Northern Hemisphere. Due to spectral truncation used in the model, only the zonal ultra-long waves 1 and 2 were included. The longitudinal distribution of the surface height, z_* , at 45N can be expressed empirically as follows:

$$z_*(45N) = A_1 \sin(m_1 \lambda) + A_2 \sin(m_2 \lambda - \frac{\pi}{2}) + \bar{z}_*, \quad (179)$$

where A_1 and A_2 are the amplitudes of zonal wave numbers $m_1 = 1$ and $m_2 = 2$, respectively; \bar{z}_* is the initial flat surface height and was used to determine the initial mean surface pressure \bar{p}_* based on standard atmosphere profiles. The latitudinal variation can be expressed by

$$z_*(\phi) = z_*(45N) \sin^2(2\phi). \quad (180)$$

For the model runs to be described in this thesis, we assumed $\bar{z}_* = A_2 = 240$ m and $A_1 = 150$ m. Although there is no mathematical requirement for $z_* > 0$, the above choice of \bar{z}_* insures this condition. The 45N longitudinal representation of the z_* field is depicted in Figure 4. The maximum z_* for the simplistic European/Asian land mass is 630 m ($A_1 + A_2 + \bar{z}_*$) and for the North American continent, it is slightly more than half that at 330 m ($A_1 - A_2 + \bar{z}_*$). Although these magnitudes are small, when compared to those used by Bourke et al.

(1977) in their spectral model, it should be remembered that their model included much higher harmonics and their spectral representations for topography were able to be more confined than in our model. However, the relative magnitude differential between the peaks for the continents is comparable. Model runs indicate that the forcing used is sufficient to generate geopotential forcing at the tropopause on the order of 300 gpm by combining the wave 1 and 2 components. This easily exceeds the wave amplitude of 200 m at 300 mb, which Schoeberl and Strobel (1980a) say are needed for stratospheric warmings to occur.

In order not to shock the model by the sudden introduction of topography, it was slowly turned on according to the following algorithm

$$\phi'_* = g(z_* - \bar{z}_*)[1 - \exp(-t/t_0^5)] , \quad (181)$$

for time t and $t_0^5 = 2.5 \times 10^5$ s. With this formulation, ϕ'_* attains about 90% of its maximum value after 7 days. Since ϕ'_* is therefore a function of time, we can obtain the time dependent values required by (159) and the current time values required by (114).

3.3 Convective Adjustment

Motions generated by models become gravitationally unstable if the temperature lapse rate exceeds that of the dry adiabat given by

$$\gamma_d = g/c_p . \quad (182)$$

To prevent this instability, we adjust forecast temperatures when they

exceed this critical value. This process is known as convective adjustment. Because of the inherent approximation in spectral models of going from real space to transform modes, some accuracy is lost to truncation. For this reason, we define a slightly weaker lapse rate as our adjustment criteria, namely,

$$\gamma_s \equiv - (g - 0.5)/c_p . \quad (183)$$

This allows for roundoff errors of the transform process.

In the model, the lapse rate is first checked at the interface. If (183) is exceeded, an adjustment is performed. Levels in the upper atmosphere are then checked and, if necessary, adjusted sequentially upward. The remaining tropospheric layers are then processed downward. This adjustment process consists of the following steps:

- (1) Compute lapse rate between adjacent prognostic levels, i.e.

$$\frac{\Delta T}{\Delta z} = \frac{(\bar{T} + T')_{i+1} - (\bar{T} + T')_i}{z_{i+1} - z_i} . \quad (184)$$

As elsewhere in the model, \bar{T} values, based on the standard atmosphere at 45N, are used for layer means based on the mean surface pressure of the layer and are initially specified before the start of model integrations. For the stratosphere, we use the z values given by (1). For the troposphere, we compute height by the following:

$$z = \frac{(\bar{\Phi} + \Phi')}{r} / g , \quad (185)$$

for any prognostic level r .

(2) If γ_s is not exceeded, we check the remaining levels. If γ_s is exceeded, we must insure that any adjustment made on temperature preserves the internal energy between the levels being adjusted. This means that

$$\int c \frac{p_s}{H} \exp(-\frac{z}{H}) T dz = \text{constant}, \quad (186)$$

$$\int c \frac{p_s}{p} T d\sigma = \text{constant}, \quad (187)$$

for the upper and lower portions of the model, respectively. The constraints denoted by (186) and (187) imply the following:

$$\frac{p_s}{H} \exp\left(-\frac{z}{H}\right) T_{K=\frac{1}{2}}^* \frac{\Delta z + p}{r=\frac{1}{2}} T_{r=\frac{1}{2}}^* \Delta \sigma = \frac{p_s}{H} \exp\left(-\frac{z}{H}\right) T_{K=\frac{1}{2}} \frac{\Delta z + p}{r=\frac{1}{2}} T_{r=\frac{1}{2}} \Delta \sigma, \quad (188)$$

$$\exp\left(-\frac{z}{H}\right) T_{K+1}^* + \exp\left(-\frac{z}{H}\right) T_K^* = \exp\left(-\frac{z}{H}\right) T_{K+1} + \exp\left(-\frac{z}{H}\right) T_K \quad (189)$$

$$T_{r+1}^* + T_r^* = T_{r+1} + T_r, \quad (190)$$

for the interface levels, upper model levels, and tropospheric levels, respectively, where T^* represents the adjusted temperature and T the original temperature at the level noted by the subscript.

(3) If adjustment is required, we specify that the new lapse rate equals γ_s . For example,

$$T_{r+1}^* - T_r^* = \gamma_s (z_{r+1} - z_r) \quad (191)$$

for the troposphere. Combining (190) and (191), we can determine T_{r+1}^* and T_r^* . Similar determinations can be made at the interface and for the upper model levels.

(4) Finally, after all levels are checked, if an adjustment were necessary, geopotential is recomputed using (114) and spectral coefficients for T_ℓ^m and ϕ_ℓ^m are computed based on the new values. The above process insures that convective stability is maintained and that thermal energy is conserved.

3.4 Spectral Truncation and Horizontal Diffusion

Following Lordi (1978), parallelogramic truncation is used as indicated in (138 - 141) with $J = 4$ and $L = 24$. We also assume symmetry across the equator, which means that ψ , ζ , Z , and V are expanded in asymmetric harmonics and the other spectral variables need only be expanded in symmetric spherical harmonics. This cuts in half computer core storage that would otherwise be needed to store these spectral coefficients.

The above truncation, along with the fact that in real space there are $N = 18$ points around each latitude circle and $I = 20$ Gaussian latitudes, insures both alias-free calculations of the Fourier coefficients by (144), which makes the transform procedure for evaluating non-linear products equivalent to direct spectral multiplication, and also integrals with respect to latitude may be computed exactly by means of Gaussian quadrature. For details, see Lordi (1978).

As mentioned in Chapter 2, horizontal diffusion was introduced to inhibit the spectral blocking that would exist because of the extensive horizontal truncation used in this model. We specified a horizontal diffusion coefficient as follows:

$$K_h = 1.5 \times 10^{6.2 \text{ } -1} \text{ m s}^{-1}, \quad \ell < 17$$

$$K_h = 6.4 \times 10^{6.2 \text{ } -1} \text{ m s}^{-1}, \quad \ell > 17.$$

However, diffusion was also only selectively applied to the higher harmonics meeting the following criteria:

$$m = 0, \quad \ell > 17$$

$$m = 1, \quad \ell > 15$$

$$m = 2, \quad \ell > 13$$

$$m = 3, \quad \ell > 11$$

$$m = 4, \quad \ell > 9.$$

For the levels at and above 43.5 km, a fourth order filter developed by Shapiro (1971) is also applied to eliminate aliasing that can exist in the vertical due to finite differencing. Because the small vertical modes propagate rapidly upward and amplify in the extremely low density mesosphere, this filter, which strongly damps these modes while not affecting the longer waves, is applied only to the upper portion of the model during each semi-implicit step.

3.5 Momentum Budget

In order to understand the time evolution of zonal wind, \bar{u} , we need a diagnostic expression for $\partial\bar{u}/\partial t$. We start by taking the zonal mean of Eq. (2.7) of Holton (1975) and using the relationship between basic density ρ_0 and scale height H of

$$\frac{1}{\rho_0} \frac{\partial \rho_0}{\partial z} = -\frac{1}{H} \quad (192)$$

to obtain

$$\begin{aligned} \frac{\partial \bar{u}}{\partial t} = & \frac{-1}{a \cos^2 \phi} \frac{\partial}{\partial \phi} [(\bar{u}\bar{v} + \bar{u}'\bar{v}') \cos^2 \phi] \\ & - \frac{\partial(\bar{w}\bar{u})}{\partial z} + \frac{\bar{w}\bar{u}}{H} - \frac{\partial(\bar{w}'\bar{u}')}{\partial z} + \frac{\bar{w}'\bar{u}'}{H} + 2 \Omega \nabla \sin \phi , \end{aligned} \quad (193)$$

where u , v , and w take on their customary meaning and Ω is the earth's angular velocity. By multiplying the above equation by $\exp[-(z-12)/2H]$, denoted by $\varepsilon(z)$, we have

$$\varepsilon(z)(\partial\bar{u}/\partial t) = FM + FB + FC + FD + FE , \quad (194)$$

where

$$FM = \varepsilon(z)(-\frac{1}{a} \frac{\partial \bar{u}'\bar{v}'}{\partial \phi} + 2\bar{u}'\bar{v}' \frac{\tan \phi}{a}) , \quad (195)$$

$$FB = \varepsilon(z)(-\frac{1}{a} \frac{\partial \bar{u}\bar{v}}{\partial \phi} + 2\bar{u}\bar{v} \frac{\tan \phi}{a}) , \quad (196)$$

$$FC = \epsilon(z) 2\Omega \bar{v} \sin \phi \quad (197)$$

$$FA = \epsilon(z) \left(-\frac{\partial \bar{w}u}{\partial z} + \frac{\bar{w}u}{H} \right) \quad (198)$$

$$FE = \epsilon(z) \left(-\frac{\partial \bar{w}'u'}{\partial z} + \frac{\bar{w}'u'}{H} \right) . \quad (199)$$

Hence, we can examine the various contributions to the mean zonal wind changes by horizontal and vertical terms with respect to both the mean flow and the eddies.

For tropospheric computations, we first compute \bar{u} , \bar{v} , \bar{w} , $\bar{u}'v'$, and $\bar{w}'u'$ on sigma levels and then interpolate to find values at 1.5, 4.5, 7.5, and 10.5 km in order to mesh with the z levels in the upper portion of the model. We then compute (194 - 199) for these levels.

3.6 Heat Budget

By taking the time mean of the thermodynamic equation used by Lordi (1978), we can write

$$\begin{aligned} \frac{\partial \bar{T}}{\partial t} &= \frac{-1}{a \cos \phi} \frac{\partial}{\partial \phi} [(\bar{v}T + \bar{v}'T') \cos \phi] \\ &- \frac{\partial}{\partial z} (\bar{w}T + \bar{w}'T') - \frac{\bar{w}HN^2}{R} + \alpha(z)(T - \bar{T}) \end{aligned} \quad (200)$$

where T is the local departure of temperature from the level mean.

Multiplying (200) by $\epsilon(z)$ yields

$$\epsilon(z)(\partial \bar{T} / \partial t) = VTB + VTP + WTB + WTP + HWB + HNA \quad (201)$$

where

$$VTB = - \epsilon(z) \frac{1}{a \cos \phi} \frac{\partial \bar{v}T}{\partial \phi} \cos \phi \quad (202)$$

$$VTP = - \epsilon(z) \frac{1}{a \cos \phi} \frac{\partial \bar{v}'T'}{\partial \phi} \cos \phi \quad (203)$$

$$WTB = - \epsilon(z) \frac{\partial \bar{w}T}{\partial z} \quad (204)$$

$$WTP = - \epsilon(z) \frac{\partial \bar{w}'T'}{\partial z} \quad (205)$$

$$HWB = - \epsilon(z) \frac{\bar{w}HN^2}{R} \quad (206)$$

$$HNA = \epsilon(z) \alpha(z) \frac{(T - \bar{T})}{e} \quad (207)$$

Equation (201) gives us a diagnostic expression for $\partial T / \partial t$ which is primarily composed of mean and eddy fluxes. For the troposphere, we first compute the fluxes at sigma levels and interpolate to z levels as with the momentum budget equation. We then compute (201 - 207) for these levels. We also assume that N^2 given by (66) is constant for the troposphere for these diagnostic purposes as is always the case with the stratosphere.

CHAPTER 4

MODEL RESULTS

The cases were run for a period of 40 days each. As mentioned in the previous chapter, the first case included temperature profiles for the stratosphere and mesosphere, which were similar to those used by Lordi (1978). Case 2 zonal winds were about 50% stronger and zonal temperature deviations were nearly twice those of the previous case. The third case was a tropospheric run using initial conditions in the troposphere identical to those of the other cases. For this last case, a lid was placed on the troposphere by assuming that $w_R = 0$ as an upper boundary condition, which implies that the divergence contribution at and below the tropopause from the upper atmosphere is also zero. The same forcing was used in each of the three cases which we will denote C1, C2, and C3, respectively. For cases C1 and C3, we used a time step of 30 minutes. C2 required a 20 minute step because the stronger flow caused limitations in meeting linear stability criterion.

Integrations were carried out on the National Center for Atmospheric Research (NCAR) CRAY-1 computer. The program, which included several output and diagnostic subprograms, required approximately 590 k of computer core storage. For each 10 day forecast, C1, C2, and C3 required 90, 135, and 20 minutes of computing time, respectively.

The time sections to be presented in this chapter were based on

12 hourly data. Except for polar projections, all tropospheric representations were obtained from data interpolated from sigma levels to constant physical height levels. Polar plots for the troposphere depict the values on a constant sigma surface. Latitude-height sections of geopotential have been density weighted, but time sections of geopotential have not. Geopotential amplitude and phase calculations have been described by Lordi (1978). In this chapter, we will use vertical cross-sections, polar projections, and time sections to describe the evolution of the individual cases, highlighting areas of similarity and dissimilarity both among the cases and with observational data.

4.1 C1 Results

4.1.1 Evolution of zonal mean velocity, temperature, and geopotential

Latitude-height sections of the mean zonal wind, mean zonal temperature deviations, and mean zonal geopotential deviations graphically illustrate the dramatic changes that take place during our simulated sudden stratospheric warmings. For the zonal wind, Figure 5 depicts the zonal wind profile for days 10, 20, 30, and 40. Comparison of day 10 (Fig. 5a) with the initial state (Fig. 2a) shows a slight weakening of the polar night jet core and slight displacement of the lower extension of this jet toward the pole. There is also a minor decrease in the amplitude of the tropospheric jet, which should be expected because of the introduction of non-zonal components.

Figure 5b shows more dramatic changes have taken place by day 20.

The polar jet core near 65 km has weakened to about one-half of its initial value and a secondary core has developed in polar latitudes around 40 km. This feature has been observed by Quiroz et al. (1975) during pre-warming stages of actual sudden warmings. This secondary jet maxima probably is the atmospheric response to the squeezing done by the northward moving easterly regime from the tropics to mid-latitudes between 20 and 40 km.

By day 30 (Fig. 5c) the polar night jet has weakened further as the secondary core has been completely eliminated and replaced by easterlies which extend from 50 km to the surface at latitudes north of 70N. Easterlies also extend from equator to pole in the lower stratosphere completely decoupling the polar night jet from the tropospheric jet which has intensified slightly probably as a response to conserve angular momentum as suggested by Koerner and Kao (1980).

By day 40 (Fig. 5d), the overall situation is similar to day 30. However, the polar night jet shows definite signs of recovery by intensifying and starting to push back into the lower stratosphere. Easterlies are also weakening both in the polar stratosphere and troposphere.

In order to highlight changes that take place during the reversal from westerlies to easterlies, we have also presented latitude-height sections for \bar{u} on days 22, 24, 26, and 28. Figure 6a for day 22 is very similar to Figure 5b, except that at this time the secondary jet is as intense as the upper core. By day 24, however, the secondary jet shows significant weakening with little change elsewhere as depicted in

Figure 6b. This weakening trend continues on day 26 (Fig. 6c) and the easterlies in the lower stratosphere at mid-latitudes also weaken. Easterlies have developed in the polar troposphere at all levels. On day 28 (Fig. 6d), the winds have reversed in the lower stratosphere. This situation is very reminiscent of the easterlies that developed throughout such a large vertical extent during the 1976-1977 sudden warming as reported by Taylor and Perry (1977).

Although the evolution of the zonal winds for this simulated warming presented in Figures 5 and 6 shows many of the characteristics of both the wave 1 and 2 forced warmings produced by Lordi (1978), there are also several differences. One dissimilarity is the contribution of the easterlies that move from the tropics to mid-latitudes in the lower stratosphere. In most of Lordi's simulations, these easterlies not only push the lower of the polar night jet northward as also happens in our simulations, but these easterlies also continue to move northward after the jet has weakened and physically replace the westerlies. In our simulations, the easterly core after initially displacing to mid-latitudes becomes quasi-stationary and the easterlies in the polar stratosphere develop almost instantaneously rather than by advection into the region. Another difference is the strength and extent of the easterlies in the upper stratosphere and mesosphere that resulted from Lordi's (1978) calculations. The pattern depicted in Figures 5 and 6 show that the mesospheric westerlies did not reverse and the strength of the easterlies that developed in lower polar regions was about one-third of those produced in simulations by

AD-A092 420 AIR FORCE INST OF TECH WRIGHT-PATTERSON AFB OH
DYNAMIC INTERACTIONS BETWEEN THE TROPOSPHERE AND STRATOSPHERE. (U)
1980 J P KOERMER
UNCLASSIFIED AFIT-CI-80-31D F/6 4/2

20F 3
AFIT-CI-80-31D

NL

(1978). Possible reasons for these discrepancies are (1) the strong continuous forcing used by Lordi at the tropopause and (2) the forcing forcing by more than one wave and was non-steady at the boundary, it is reasonable to expect a somewhat weaker outcome, especially at higher levels. Latitude-height sections of zonal temperature deviations corresponding to the days depicted in Figures 5 and 6 are presented in Figures 7 and 8. Comparing Figure 7a with Figure 3a, we can note some warming in the lower polar stratosphere and slight cooling in the mesospheric regions above. By day 20, Figure 7b shows this trend more dramatically. It also shows stratospheric cooling and mesospheric warming in equatorial regions. The polar and equatorial regions of the troposphere reflect, to a small degree, the temperature change characteristics of the stratospheric regions above. Figure 7c continues the trend through day 30 and more clearly depicts the cooling in the upper stratosphere. By day 30, the temperature gradient in the lower stratosphere has reversed with warmer temperatures at the pole than in upper mid-latitudes, thermally supporting the easterlies that have developed. The temperature reversal continues through day 40 (Fig. 7d), but is confined to a more shallow layer in the lower stratosphere and upper troposphere. Cooling was beginning to take place in the upper stratosphere and mesosphere in polar regions. Figure 8(a through d) depicts the rapid temperature changes during the height of the warming process, when the polar westerlies are replaced by easterlies.

During this simulated warming, polar stratospheric temperatures rose by nearly 40°K . Mesospheric temperatures cooled some 15°K at the

pole. Near the equator stratospheric temperatures cooled almost 5°K with the same amount of warming in the mesosphere. All of these features are consistent with observed changes in actual warmings and have been described in Houghton (1978).

Figures 9a through d depict the density weighted latitude-height sections of geopotential deviation of the wave 1 component for days 10, 20, 30, and 40. From Figure 9a, we can see even by day 10 the effect of the tropopause in limiting the vertical propagation of wave energy. Energy does move into the stratosphere and favors a more poleward location than the original tropospheric forcing component. By day 20 (Fig. 9b), wave 1 energy propagates even higher and another surge of geopotential is emanating from the troposphere into the lower regions of the polar stratosphere. By day 30 (Fig. 9c), the geopotential wave 1 amplitude in the upper region has weakened considerably; but, in the lower regions, it has intensified and is more disjointed from the troposphere. By the final day of the forecast period (Fig. 9d), the wave amplitude extends higher once again, but the core in the lower stratosphere has also weakened. The phase lines marked on Figures 9a and b show increasing phase with height indicating warm air is being transported northward in the stratosphere (Holton, 1975). This phase relationship has altered significantly by day 30 (Fig. 9c). The situation on day 40 (Fig. 9d) also shows only weak variations of phase with height indicating nearly barotropic conditions.

Figure 10a shows that on day 10 wave 2 is stronger in the lower stratosphere than wave 1 (Fig. 9a), but it does not extend upward as

far as wave 1. It also appears at lower latitudes and tends to be linked more closely with orographic forcing. By day 20 (Fig. 10b), wave 2 intensifies, but changes little in vertical extent. There is also much greater discontinuity with the troposphere. After the reversal, Figure 10c shows a much weaker wave 2 geopotential in the stratosphere which continues through day 40 (Fig. 10d) until wave 2 has practically been eliminated. This follows from Charney and Drazin (1961), since the easterlies serve a critical layer preventing upward wave propagation. According to Houghton (1978) when the source of wave energy is cut off by a critical level, the wave energy present will gradually decay. Wave 1, although affected to some extent by the critical level, probably has some components with easterly phase speeds allowing it to still propagate from the troposphere to the stratosphere. The phase relationship with height for wave 2 closely parallels that of wave 1. Figure 10a and b clearly indicate increasing phase with height and warm air transport towards the pole. The phase relationship for days 30 and 40 (Figs. 10c and d) is not clearly defined and hence more barotropic.

4.1.2 Horizontal Evolution of Geopotential, Temperature, and Tropospheric Jets

Initially, we started with zonal mean fields for geopotential, temperature and velocity. In order to see the meridional and longitudinal development of these fields, we will now show the evolution using polar projections. Figure 11a depicts geopotential deviation at 40.5 km after 10 days of integration. Although basically remaining

circular, as it was initially, the vortex gets displaced slightly from the original pole location and a high develops downstream of the larger orographic peak. By day 20 (Fig. 11b), a distinct wave 2 pattern has developed with an elongated vortex still centered near the pole. However, by day 30 (Fig. 11c), the vortex has split and a high dominates the pole. Figure 11d indicates the high is weakening and a less pronounced wave 2 pattern by day 40. The polar vortex is also starting to regain its hold on the polar regions.

In the troposphere at approximately 6.7 km, the geopotential pattern becomes essentially anchored by orographic forcing as depicted in Figures 12a through d. The vortex does elongate and split as in the stratosphere, but the changes are more subtle than in the stratosphere. We can see that in the troposphere the waves tend to be super-imposed on the mean condition with greater wave activity during the latter stages of integration after the warming process.

At 40.5 km, temperature deviations respond similar to geopotential patterns. First, there is a displacement of the cold center from the pole (Fig. 13a). Next, the displacement continues and temperatures at the pole begin to warm as the high intensifies, as shown in Figure 13b. Thirdly, the cold core splits (Fig. 13c) as warmer temperatures dominate the pole. Finally, the warming subsides and conditions try to return more closely to a zonal mean state (Fig. 13d).

Tropospheric temperature deviations as shown in Figures 14a through c depict more clearly the development of higher harmonic wave components after evolving from a nearly zonal state on day 10 to a

more complex state by day 40. These patterns reflect to a slight degree the changes that have been occurring in the lower stratosphere.

The tropospheric jet first intensifies at locations upwind of orographic forcings as depicted in Figure 15a. This response is probably due to the increased convergence initially developing in these regions as topography is gradually introduced. By day 20 (Fig. 5b), these jets have intensified proportionally to the height of the topography and have moved counterclockwise until slightly downstream of the orographic peaks. Another more southerly positioned jet has developed upstream of the weaker peak. By day 30 (Fig. 15c), the jet over the higher peak now remains essentially anchored, but elsewhere the jet locations are more transient and move westward, a trend that continues on day 40 (Fig. 15d).

4.1.3 Evolutions of Zonal Mean Velocity

Components, Temperatures, Geo-potential and Momentum and Heat Budgets at 68.9 N

Since we have now given a detailed description of C1 evolution, we want to delve more closely into the rapid changes that occur during the warming process. Time-sections are an ideal tool for studying these changes. We will use both height-time sections to study vertical variations and latitude-time sections to depict meridional variations. For height-time sections, 68.9°N was chosen as the latitude for depiction since it depicts most generally features at both lower and higher latitudes. The 7.5 km level was chosen to represent the troposphere on

latitude-time sections, while 40.5 and 67.5 km were chosen to represent the upper atmosphere.

Figure 16 shows time-height sections for zonal mean values of u , v , w , and T' . During the first 15 days (Fig. 16a), the changes in \bar{u} are quite small in contrast to the following 15 day period when the wind reverses. Figure 16b shows two distinct southerly component peaks around 45 to 50 km on day 16 and day 27 followed by a much weaker northerly peak on day 32. The two southerly peaks correspond with two shown on Figure 16c. This relationship between \bar{v} and \bar{w} is a very important ingredient of the warming process and represents the major portion of an indirect circulation cell. As noted by Matsuno (1971), this cell consists of rising air in polar regions, equatorward transport at higher levels, and sinking motion at mid-latitudes. This cell is completed on the lower end by the eddy transport of sensible heat toward the pole. After the zonal wind reverses (Fig. 16a), Figures 16b and c indicate the presence of a meridionally direct circulation. The temperature height-time section (Fig. 16d) shows the most rapid warming activity in the stratosphere during the same periods when the indirect cell circulations are also most intense. Mesospheric cooling and tropospheric temperature changes are much smaller in comparison to those occurring in the stratosphere.

Figures 17a through d depict height-time sections of geopotential (not weighted by density) for zonal waves 1 through 4, respectively. Wave 1 usually dominates the upper stratosphere and mesosphere (Fig. 17a), whereas wave 2 (Fig. 17b) prevails in the lower stratosphere. By

comparing these two wavenumbers, we note that the maximums and minimums are nearly 180° out of phase. As mentioned by Koerner and Kao (1980), this indicates the non-linear transfer of energy between waves 1 and 2. Wave 1 shows a distinct oscillation between the peaks at 60 km with a period of 17 days. Wave 2 has one very strong peak occurring right before the reversal and weakens considerably after day 25. Tropospheric peaks slightly lead the stratospheric ones. In view of the growth of waves 1 and 2 during the periods of kinetic energy decrease of the zonal mean flow (Fig. 16a), a transfer of kinetic energy from the zonal mean flow to the waves may occur after day 15 of the integration.

Observationally Perry (1967) showed that wave 3 was a source of weakening for waves 1 and 2. By virtue of wave-wave interaction, it also can help transfer energy between these waves. Our investigations support these characteristics as shown in Fig. 17c. The first peak for wave 3 on day 21 corresponds to a rapid weakening of wave 1 in that region and the wave 2 intensification at lower levels a few days later. Conversely, the remaining peaks correspond to wave 2 weakening and precede wave 1 intensification during the latter stages of the warming. Wave 4 (Fig. 17d) remains relatively small and peaks when wave 2 reaches its maximum. Hence, wave 4 plays a much more minor role than the longer planetary waves in this simulated warming. It appears, therefore, waves 1, 2, and 3 form an active triad in nonlinear energy transfer. Geopotential maximums in the upper atmosphere tend to be directly in phase with maximums in the troposphere. The amplitude

of the zonal wind also tends to be inversely proportional to wave amplitude. These features were noted in the 1976-1977 warming by Koerner and Kao (1980).

At the end of Chapter 3, we introduced expressions to diagnose zonal wind and temperature changes. By computing and summing all the terms on the right side of equation (194), we have the instantaneous rate of change of zonal velocity depicted as a latitude-time section in Figure 18a. The largest negative stratospheric values indicate decreasing westerlies and occur on days 15 and 24. As indicated by 16a, these westerlies do decrease rapidly between these dates, making these calculations consistent. Instantaneous velocity changes in the troposphere are much more complex and not as clearly defined.

The largest terms that make up $\partial \bar{u} / \partial t$ are FM and FC as indicated by Figures 18b and c. However, these terms have opposite sign and nearly cancel open another in the lower stratosphere as from day 10 to day 21. During the period from day 21 to day 26, a period characterized by a rapid weakening of the zonal wind, the FC term dominates in the lower stratosphere, resulting in westerly decelerations from coriolis torque, which highlights the importance of the indirect cell circulations in the warming process. During early warming stages, when FM and FC are nearly cancelling one another, indicating the "non-interaction effect" of the meridional convergence of $\bar{v}'\bar{u}'$ on the mean flow, the largest term contributing to the decrease of the stratospheric westerlies is FB, depicted in Figure 18c with a peak around day 15 at 40 km. At lower levels, the usually very small FA term also peaks (Fig. 18d) and

also contributes to the deceleration of the westerlies. The FE term (Fig. 18c) contributes the least, but also has a negative peak around day 14 at 30 km and does slightly aid in decreasing the westerlies.

The momentum budget for Case 1 indicates two distinct processes involved in the deceleration of the polar night jet. During the first 20 days of model integrations, an indirect cell forms, a process described by Matsuno (1971). However, the convergence of westerly eddy momentum flux at higher latitudes is nearly compensated by the coriolis torque, basically negating the effects of the indirect cell on the rate of change in the zonal flow. Since the larger terms cancel, the deceleration that occurred during this stage of the warming can be attributed to the smaller terms which have their largest negative values in the stratosphere. From day 21 to 26, the small terms become negligible and an imbalance develops between FM and FC with FC slightly more dominant. With the negative term larger, rapid deceleration can take place, leading to easterlies.

As shown in Figure 19a, the instantaneous temperature changes at 68.9N are not as clearly defined in the stratosphere as were the zonal wind changes. They are positive through most of the stratosphere, indicating warming and negative in the mesosphere indicating cooling. As with the momentum budget, there are two large terms--VTP and HWB--in the zonal heat budget as indicated in Figures 19b and c, respectively. However, they are nearly equal in magnitude and opposite in sign, indicating that eddy heat flux convergence is basically compensated by adiabatic cooling as the large peaks of Figures 19b and c are nearly

in phase during the entire forecast period. This indicates that there exists a "non-interaction effect" of the meridional convergence of meridional flux of sensible heat on the vertical motion. The smaller terms depicted in Figures 19d through g show that among them WTB plays the most significant role in warming the stratosphere, but even it is quite small. Perhaps the lack of definition of the heat budget is due to the choice of latitude in this case, since temperatures change more dramatically closer to the pole.

4.1.4 Evolutions of Zonal Mean Velocities

Temperature, Geopotential, and Momentum and Heat Budgets at Various Heights

Latitude-time sections can better show these north-south relationships and are introduced here. Latitude-time sections of zonal velocity at 7.5, 40.5 and 67.5 km are presented in Figures 20a through c. Few changes occur in the troposphere except for the nearly instantaneous switch to easterlies around day 29 in polar regions. In the stratosphere at 40.5 km after 10 days, we can see the displacement of the polar jet towards the pole with a dramatic weakening of the jet and ultimate reversal between day 23 and day 28. Figure 20b also clearly shows that easterlies from mid-latitudes do not displace poleward, but rather the easterlies develop on their own. At high levels, we can note from Figure 20c that higher latitudes show a southward displacement of the polar night jet, the decreasing amplitude of the jet, and reintensification of the jet during the later portion of the

period depicted.

Figures 21a and b clearly indicate the two major indirect cells that develop during the warming process. Figure 21a shows the southerly component linking the areas of strong vertical motion (Fig. 21b). Weaker direct cells develop simultaneously at lower mid-latitudes. Two direct cells also form in the polar regions one with a maximum amplitude on day 22, when the indirect circulation at lower latitudes is at a relative minimum and the other during maximum easterly development.

Temperature deviations, depicted on Figures 22a through c, show warming at 7.5, 40.5, and 67.5 km in higher latitudes and cooling to some extent at latitudes near the equator. Even though the changes in the troposphere are quite small, they reflect the changes that have occurred in the stratosphere.

Wave 1 geopotential amplitude in the troposphere (Fig. 23a) shows a periodicity on the order of 10 to 15 days. The first two peaks are located around 45°N where the maximum orographic forcing was positioned. The final peak at the end of the forecast period was further north. At 40.5 km, wave 1 amplitude also shows vacillation with about the same periodicity as the troposphere, but favors polar latitudes as indicated in Fig. 23b. The first two tropospheric maximums slightly lead the stratospheric maximums, a feature observationally consistent with data presented by Labitzke (1978b) and O'Neill and Taylor (1979). At even higher levels (Fig. 23c), the wave amplifies due to decreasing density and only two major peaks in wave 1 amplitude are present. The first

maximum shows a definite lag with lower level values, but the second one is nearly in phase with that at 40.5 km.

Figures 24a through c show wave 2 geopotential amplitude at the same levels as above. Peaks at all levels are generally not in phase with wave 1 peaks at the same level, indicating energy transfer between these waves as mentioned by Koerner and Kao (1980). Despite a vacillating behavior in the troposphere, at 40.5 km the situation is more steady with essentially one major peak. At higher levels, the maximum occurs about 5 days after the 40.5 km maximum, but the values are much smaller than they were for wave 1 at the same level.

Unlike waves 1 and 2, wave 3 (Figs. 25a through c) gets little of its energy from the troposphere, as we can see by examining the phase relations at higher levels versus that at tropospheric levels. Even in the troposphere, the source of wave 3 excitation in this model is from wave-wave and/or wave-mean flow interactions. At 40.5 km, the wave-wave interaction is quite evident, since the first peak corresponds to wave 1 dissipation and the second peak to the very large and fast wave 2 dissipation. A similar relationship holds at 67.5 km.

Wave 4 generally peaks with wave 2 in the stratosphere and apparently leads wave 4 development in the troposphere, where wave 2 and 4 are more out of phase than in phase. As was the case with wave 3, stratospheric amplitudes are small, especially at high levels, as we can see from Figures 26a through c.

If we look at the momentum budget at 40.5 km, we can see more clearly the physical processes involved in the wind reversal. Figure

27a clearly shows the large deceleration taking place at high latitudes from day 12 through 27. Again Figures 27b and c indicate that the eddy momentum flux convergence is nearly balanced by the coriolis torque with the latter being slightly larger. There is little activity at lower latitudes. Of the remaining terms in Figures 27d through f, only the mean momentum flux convergence shows a significant contribution to the deceleration of the polar night jet and ultimate reversal.

The heat budget at 40.5 km is not clearly defined, as the instantaneous temperature changes are small and the horizontal eddy heat flux convergence is basically offset by adiabatic cooling, as shown in Figures 28a through c. Of the four remaining small terms (Figs. 28d through g), generally all but the vertical eddy heat flux, WTP, are positive during the warming stages and assist the warming process at this level. At lower levels (not shown here), horizontal eddy heat flux, which forms the bottom part of the indirect cell, is more dominant and does contribute to the warming of the stratosphere.

4.2 Case 2 Results

4.2.1 Evolution of Zonal Mean Velocity, Temperature and Geopotential

Latitude-height sections of the mean zonal wind for case C2 with stronger winds in the upper atmosphere for days 10, 20, 30, and 40 are presented in Figures 29a through d, respectively. Up to day 20, the evolution of these profiles are very similar to C1. However, C2 does not always maintain separate split cores as indicated in Figure 29b

where only the lower level core remains. The tropical easterlies tend to displace the lower extension of the polar night jet to higher latitudes, but the critical line ($\bar{u} = 0$) does not advance as far or as rapidly northward as in C1 (Fig. 5b). The easterlies that do develop in the lower mid-latitudes of the stratosphere are more intense.

By day 30 (Fig. 29c), a double core is again present and the overall situation is very similar to that of day 20 for C1 (Fig. 5b). The intensity of the polar night at higher levels has weakened considerably, but in the lower levels, it is still fairly strong. Some noticeable differences between C2 and C1 are the downward propagating easterlies at subtropical latitudes in the mesosphere in C2 and the more concentrated depiction of the tropospheric jet in C2. By day 40 (Fig. 29d), the lower extension of the polar night jet weakened, causing the secondary jet to vanish, while the jet at higher levels in the stratosphere shows intensification.

To highlight the most dramatic changes that occurred during C2 integrations, we have also presented the zonal wind profiles at 2 day intervals between days 30 and 40. On day 32 (Fig. 30a), the easterly jet intensifies and pushes down into the mesosphere. This displaces the polar night jet northward causing intensification of the jet in the upper levels of the stratosphere. By day 34 (Fig. 30b), the easterlies in the mesosphere continued to intensify as does the polar-night jet at higher latitudes. By day 36 (Fig. 30c), the mesospheric easterlies have started to subside and the polar jet begins to return to more southerly latitudes. As it regresses, the lower extension of

this jet weakens significantly. This trend continues on day 38 (Fig. 30d), but apparently bottoms out as the jet in the lower polar stratosphere shows signs of intensification by day 40 (Fig. 29d). The evolution of C2 is much more dramatic at higher levels than C1 and indicates that strong winds serve as a source to enhance wave activity throughout the stratosphere and mesosphere.

C2 temperature deviations respond similar to C1, but not as fast as C1 through the first 20 days of integrations (Figs. 31a and b). By day 30 (Fig. 31c), there is significant warming in the mid and low stratosphere and cooling in the upper stratosphere and mesosphere. A slight temperature reversal has even occurred between 40 and 50 km. All of these changes in polar regions are accompanied by equatorial cooling of the stratosphere. By day 40 (Fig. 31d), the temperature reversal is no longer present in the mid-stratosphere, but lower stratospheric levels have warmed significantly. Elsewhere, the cooling trends are beginning to reverse.

A closer look between days 30 and 40, reveals that the temperature reversal in the mid-stratosphere near the pole was short lived and not even present by day 32 (Fig. 32a). During this ten day period the mid-stratosphere alternately warmed and cooled as indicated by Figures 32a through d, but the lower stratosphere generally continued to warm by nearly 20°K. However, by day 40 (Fig. 31d), cooling was apparent at all levels in the polar stratosphere.

Wave 1 geopotential (density weighted) and corresponding phase angles with height for C2 on days 10 and 20 (Figs. 33a and b) are quite

similar to those of C1 (Figs. 10a and b). Maximum amplitudes for C2 are slightly south of the locations in C1 and they also extend to slightly higher stratospheric levels. The geopotential extension from the troposphere upward and northward into the polar stratosphere is similar for both cases, but the amplitude of C2 is larger. By day 30 (Fig. 33c), wave 1 develops a tremendous amplitude throughout the entire polar stratosphere, a feature not present in C1. This large peak is nearly disjointed from the troposphere. Figure 33 shows a similar pattern existing again on day 40, indicating a strong wave 1 component. As with C1, phase angles for C2 are more baroclinic at early stages of the warming and become essentially barotropic at later stages.

Figures 34a through d show wave 2 geopotential evolution for C2. The phase relationship evolves similar to that mentioned above for wave 1 with the greatest increase of phase with height on day 10. Wave 2 also penetrates higher levels when the stronger westerlies are present with amplitudes slightly south of the C1 locations in the stratosphere and with C2 amplitudes spread over a broader area. Wave 2 weakening in the stratosphere during the latter phases of the integration period are quite similar for both C2 and C1, despite the fact that the winds did not reverse in C2. This may indicate the presence of a stratospheric vacillation cycle as discussed by Holton and Mass (1976).

4.2.2 Horizontal evolution of Geopotential, Temperatures, and Tropospheric Jets

Polar projections of geopotential deviations at 40.5 km show little disfiguration of the polar vortex of day 10 (Fig. 35a). By day 20 (Fig. 35b), high pressure cells do develop and tend to squeeze the vortex in a wave 2 pattern similar to C1 (Fig. 11b). However, the vortex continues to hold in polar regions on day 30 (Fig. 35c) with high pressure cells no longer on opposite sides of the vortex, but tending to merge, which they effectively do by day 40 (Fig. 35d). Acting together, the polar vortex gets displaced, but not far enough for easterlies to dominate the polar regions.

In the troposphere, the evolution of geopotential for C2 during the first half of the integration period (not shown here) is nearly identical to that for C1 (Figs. 12a and b). During the second half (Figs. 36a and b), C2 does show some subtle differences with C1 (Figs. 12c and d), with C2 having a more pronounced wave 3 and 4 pattern than C1. Usually, the geopotential configuration near the tropopause at 13.5 km was very close to that of 7.5 km. However, during the last ten day period of C2 when warming activity was the strongest, a strong wave 3 pattern developed (Figs. 36c and d), which is often associated with blocking in the troposphere. This feature is not as prominent at lower levels because of the dominance of waves 1 and 2 from orographic forcing.

The C2 plots of temperature deviation for 40.5 km on days 30 and

40 and the corresponding 7.5 km results are shown on Figures 37a through d. Patterns during earlier stages of the integrations were similar to those of C1 (Figs. 13a and b). In comparison with C1 at later stages (Figs. 13c and d), we can see that wave 1 is much more prominent in the stratosphere for C2. The rapid migration of the cold core about the pole for this case indicates large traveling components and wave transience. In the troposphere, patterns are still most strongly influenced by orography and hence are quasi-stationary, but C2 (Figs. 37b and d) shows more diversity in wave activity than C1 (Figs. 14b and d).

The tropospheric jet maxima for C1 (Figs. 15a through c) were quite similar to C2 (not shown). However, the C2 maxima were generally weaker, tending to make the overall flow more zonal than in C1. The apparent anchoring of one jet to the highest topography was present in both cases, as was the transience of the maxima elsewhere.

4.2.3 Evolutions of Zonal Mean

Velocity Components, Temperature,

Geopotential and Momentum and

Heat Budgets at 68.9 N

Even though a major warming according to WMO standards failed to develop for C2 as it did for C1, the so-called "minor" warming was even more dynamic. The time section of zonal wind (Fig. 38a) shows strong vacillations after day 20 with a periodicity of around 7 days. During the pre-warming stages, the jet actually intensifies. The zonal mean v (Fig. 38b) and w (Fig. 38c) also indicate 5 indirect cell

circulations with the most intense cell around day 25 corresponding to the period of greatest warming as shown in Figure 38d. The periodicity of the first two of these cells is quite similar to that of C1, but the C2 circulations are more intense, especially the second one. The smaller indirect circulations that developed after this large one were unique to C2, since in C1 a direct circulation developed after the easterlies developed in the polar stratosphere. At 68.9°N , mid-stratospheric temperatures peaked around day 29. It was preceded by rapid warming and followed by fairly rapid cooling as indicated in Figure 38d. Warming of the lower stratosphere took place gradually almost from the start of integrations, but was most intense from days 31 to 35.

As shown in Figure 39a, wave 1 geopotential for C2 clearly indicates stronger and more rapid vacillations than occur in C1 (Fig. 17a) during the second half of the integration period. During these stages when C2 is most active, wave 1 peaks are exactly in phase with \bar{u} minimums (Fig. 38a), indicating that a portion of wave 1 energy is being extracted from the mean flow. This is similar to the observed data presented by Koerner and Kao (1980). Because of the strong fluctuations of wave 1 (Fig. 39a) and from the polar representation of geopotential (Figs. 35a and b), it is apparent that the polar vortex is wobbling like a spinning top about the pole. When it becomes centered over the pole, the amplitude of wave 1 suddenly decreases. When it shifts away from the pole, there is rapid intensification of wave 1. Generally tropospheric peaks slightly lead stratospheric

maxima.

Wave 2 geopotential (Fig. 39b) for C2 is also stronger and varies more frequently during the latter stages of the forecast period than it was for C1, reaffirming the importance of the critical level that develops when the easterlies extend from equator to pole in cutting off the source of wave excitation in the stratosphere. Wave 2 is essentially out of phase with wave 1, indicating (as in C1) the non-linear transfer of energy. This transfer is again aided by wave 3 (Fig. 39c), which intensifies more slowly at first than it did in C1; but then intensifies and oscillates rapidly during the latter stages of the forecast period. As with C1, wave 3 maxima for C2 tend to occur during the periods when wave 1 is increasing and wave 2 is decreasing or vice-versa. Wave 4 (Fig. 39d) is essentially in phase with wave 2 but is of much higher amplitude than it was for C1 (Fig. 17d).

The strong stratospheric vacillations indicated by geopotential oscillations of the wave components in C2 do not show in the analysis of Holton and Dunkerton (1978). Using a linearized model, they suggest that waves which are able to propagate to large heights produce weaker amplitude vacillations than those that can propagate only to lower levels. C1 corresponds to this latter case in that waves do not propagate to high levels when the zonal winds are weak. C2 with stronger winds and consequently higher wave propagation corresponds to the former. However, C2 produced the largest vacillations in our integrations compared to C1. This difference is probably due to the non-linear effects and due to the presence of four waves in our model.

The strong zonal winds of C2 provide a large energy source from which all waves can extract energy. If the waves are stronger, the wave-wave interaction transfers of energy will probably be larger and greater vacillations result along with greater wave transience. However, if only the waves and mean flow interact, this may not be the case, as shown by Holton and Dunkerton (1978). This discrepancy clearly shows the importance of including wave-wave interactions in the modeling such phenomena as stratospheric warmings.

Instantaneous velocity changes in the stratosphere are also more pronounced for C2 as indicated by Figure 40a. As should be expected, this means that the momentum budget terms should be more pronounced to cause the larger changes, primarily in decelerating the zonal westerlies of the stratosphere. As with C1, the large eddy momentum flux convergence (FM) (Fig. 40b) is compensated to a large extent by the coriolis torque (FC) (Fig. 40c). During the early stages of C2 integrations, FM (which peaks on day 15 of this period) is slightly larger than FC, aiding the acceleration of the westerlies as indicated on Figure 38a. During the next large oscillation, the peaks nearly coincide and cancel because of their opposite sign. During the latter stages of the forecast period marked by frequent vacillation, these terms change rapidly and do not always balance one another, as is the case between days 35 and 37, where FC is more dominant. This imbalance probably is most responsible for the final deceleration phase of the westerlies as shown in Fig. 38a. The smaller terms (Figs. 40d through f) show two major peaks in the stratosphere corresponding to the first

two maxima of FM and FC (Figs. 40b and c) and closely linked to the indirect cell mechanism. FB, FA, and FE all tend to decelerate the stratosphere westerlies at higher latitudes when they are large in amplitude. Since they are still often small in relation to the large terms (FM and FC), it makes their contribution more dubious. For example, the zonal westerlies in the stratosphere still increased during the pre-warming stages despite the fact that vertical fluxes and mean momentum flux were working against this since there was sufficient imbalance between FM and FC to result in acceleration. However, these terms can play a role, as during the second major cycle when FM and FC effectively cancel and zonal wind changes still occur. FB, FA, and FE contribute little during the latter stages of the forecasts.

The net result of instantaneous temperature changes (Fig. 41a) is not clearly defined because of the cancelling effect of the contributing terms. From Figure 41b, we can see the lower portion of the indirect cells alluded to earlier. This eddy meridional heat transport is counteracted to a large extent by the adiabatic cooling effects of HWB (Fig. 41c). During the first pulse, the net heating between days 10 and 18 in the stratosphere as indicated on Figure 38d may be due to WTB (Fig. 41e) since VTP and HWB nearly cancel. However, WTP (Fig. 41f) reduces the extent WTB and the other small terms VTB (Figs. 41d and f) show little contribution. During the second warming pulse between days 24 and 29 (Fig. 38d), VTP (Fig. 41b) with weak assistance from WTB (Fig. 41e) apparently dominates HWB (Fig. 41c) and the other small terms, resulting in mid-stratospheric warming. From days 20 to

33, this trend reverses and cooling takes place (Fig. 38d).

4.2.4 Evolutions of Zonal Mean Velocities, Temperature, Geopotential, and Momentum and Heat Budgets at Various Heights

Latitude-time sections for zonal wind are shown in Figures 42a through c. Tropospheric wind evolution (Fig. 42a) is similar to that of C1 (Fig. 20a), except easterlies did not develop for C2. At 40.5 km (Fig. 42b), the slower evolution of C2 is evident although the poleward displacement of the jet is similar to C1 (Fig. 20b). The time evolution of mean zonal wind at 67.5 km (Fig. 42c), the situation is quite different from C1 (Fig. 20c) with C2 showing greater oscillations along with more rapid decelerations at lower latitudes. This is probably the result of easterly jet development in the mesosphere above these latitudes.

The major indirect cell circulations are clearly evident at higher latitudes from Figure 43a and b. Both cells develop at about the same time as they had done during C2 integrations, probably indicating an inherent vacillation process as proposed by Holton and Mass (1976) since at this time waves were primarily extracting energy from the mean flow. Thermally direct circulations also simultaneously develop in mid-latitudes as they had done in C1. All of these circulation cells, although similar, lie further south for C2 than in C1.

Tropospheric temperature changes (Fig. 44a) for C2 are similar to C1 (Fig. 22a) except for the sudden cooling in the polar regions that

occurred after the initial warming during C2 integrations. At 40.5 km (Fig. 44b), sudden warming in polar regions occurs from days 24 to 30, followed by cooling almost as large from days 30 to 34. At lower latitudes, the evolution is remarkably similar to C1 (Fig. 22b). The warming and cooling surges at 67.5 km (Fig. 44c) basically mimic those of 40.5 km just described. C2 temperature changes were slower in coming about than in C1, but when they did occur the changes were much more rapid and about the same order of magnitude as in C1.

In the troposphere, C2 wave 1 geopotential (Fig. 45a) looks much like that of C1 (Fig. 23a) for the first 30 days. However, after the wind reverses in C1, wave 1 tropospheric geopotential appears much larger in the polar regions. At 40.5 km (Fig. 45b), C2 wave 1 geopotential is essentially similar to that of C1 (Fig. 23b) with a maximum amplitude during these pre-warming stages slightly larger and about 10° further south than C1. The last 13 days of each case are considerably different with tremendous wave 1 activity for C2 as described earlier in this section. At even higher levels (Fig. 45c), wave 1 appears to be out of phase and lagging the 40.5 km level. Higher periodicities are characteristic of the latter part of C2 integrations. It is during the times of sudden wave 1 amplification that westerlies tend to decelerate most rapidly.

Wave 2 geopotential for C2 (Fig. 46a) at 7.5 km has the same basic features as C1 (Fig. 24a), showing only slightly larger amplitudes at higher latitudes. At 40.5 km (Fig. 46b), wave 2 is out of phase with wave 1 (Fig. 45b). This is especially vivid from day 27 to day 31,

where wave 2 decreased rapidly as wave 1 simultaneously amplified. Recall that the warming essentially peaked during this period. Wave 2 (Fig. 46c) is much stronger and more active at 67.5 km than it was for C1 (Fig. 24c). Again, it shows an out of phase relationship with wave 1 (Fig. 45c).

Although wave 3 (Fig. 47a) evolves in the troposphere at about the same time as it does in C1 integrations (Fig. 25a), we can see that the C2 development is much more intense, reflecting the wave 3 pattern discussed earlier that occurs during the latter stages of the forecast period. At higher levels (Figs. 47b and c), wave 3 is also stronger than in the previous case and its vacillations correspond to wave 1 and 2 energy transfers.

Wave 4 geopotential for C2 (Fig. 48a) has about the same tropospheric amplitude as it did in C1 (Fig. 26a). Stratospheric values (Figs. 48b and c) are in contrast much larger for C2 indicating the greater energy source available initially. As with C1, wave 4 maximums are closely linked to wave 2 peaks.

Latitude-time sections for the momentum budget at 40.5 km are presented in Figures 49a through f and essentially confirm the processes described earlier based on time-height sections. FM is basically the only term trying to maintain or accelerate the westerlies. FC provides the greatest source for deceleration and in fact the greatest deceleration usually occurs when FC is clearly dominant over FM. During the last 12 days, the C2 warming remains characterized by oscillations reflected in the momentum budget terms and which is probably a result

of the rapid energy transfer between waves.

The instantaneous temperature change (Fig. 50a) also indicates the oscillating behavior of C2, especially at high latitudes. Most of the fluctuations can be attributed to small imbalances between VTP (Fig. 50b) and HWB (Fig. 50c). Warming is aided to a small extent at high latitudes by VTB and WTB, indicated in Figures 50d and e. At somewhat lower latitudes, WTP (Fig. 50f) contributes to cooling. HNA contributes little to the heating and cooling processes at this level.

In summary, C2 is similar to C1 during the first half of the forecast period, but C2 becomes more complex during the latter stages when it becomes highly oscillatory in all respects. During these sudden changes, imbalances in indirect circulations develop resulting in deceleration or acceleration of the zonal wind and heating or cooling. These processes are in good agreement with the basic mechanism proposed by Matsuno (1971). The oscillations themselves tend to be the result of wave transience and wave-wave interactions. In this case as in C1, large terms in the momentum and heat budgets nearly cancel. However, the slight imbalances between these large terms can control the warming process. It is only when these large terms essentially cancel, that the smaller terms become important enough to affect significant wind and temperature changes. Even though the warming generated in C2 over the 40 day integration period cannot be classified as major, it was as dynamic as the major C1 warming in its evolution. C2 results also tend to confirm the hypothesis of Koerner and Kao (1980) that a strong polar vortex can inhibit major stratospheric warmings.

4.3 Case 3 Results

Case 3 (C3) involved running the model for the troposphere only using the same initial conditions for these levels as were used in C1 and C2. Identical forcing was also used. A lid was placed on the model at 12 km negating interactions with the stratosphere. By doing this, we are able to highlight interaction effects from the stratosphere to the troposphere of C1 and C2 by comparing their tropospheric results with those of C3.

Latitude height sections of zonal velocity for C3 are shown in Figures 51a through e. Relatively few changes from the original profile (Fig. 51a) occur until late in the integration period. At this time (Figs. 51f and e) a dual jet develops in the subtropics and at mid-latitudes. This feature did not develop in C1 and C2, but may be the result of upper boundary reflection.

Polar plots of geopotential deviation at approximately 6.7 km show a very monotonous pattern in Figures 52a through d. The wave activity other than that being forced by orography is much less pronounced than that which resulted by inclusion of an upper atmosphere. The temperature deviations (Figs. 53a through d) also follow this trend with a zonal type pattern throughout the forecast period in contrast with the non-zonal nature of the temperature distribution of C1 (Figs. 14c and d) and of C2 (Figs. 37c and d) recorded at later stages of the integrations. The C3 zonal wind maxima (Figs. 54a through d) shows a rather slow development versus the other cases. There is also no apparent anchoring of a jet to topography in C3 as was noticed in C1

and C2. Instead, all the maxima move around a latitude circle with the mean flow.

At 7.5 km (Fig. 55a), changes in the C3 zonal wind are slower, weaker and steadier than the other cases. Polar easterlies do develop as they did in C1, but the development is more gradual than the sudden change noted in C1 (Fig. 20a). Temperature (Fig. 55b) does not significantly change during the entire forecast period in stark contrast to the development of C1 (Fig. 22a) and C2 (Fig. 44a). This difference probably indicates an important interaction between the stratosphere and the troposphere in that the troposphere reflects, to a small degree, the stratospheric temperature changes. As noted by Namias (1978), the mean temperatures at higher latitudes in January 1977 were much warmer than normal following a major sudden warming very similar to that produced in C1. Although many areas were warmer, some areas of the United States experienced the coldest January ever known (Wagner, 1977). Hence, the stratosphere may influence the troposphere significantly enough to produce long-term climatic anomalies.

Finally, the geopotential wave amplitudes for waves 1 through 4 (Figs. 56a through d) show much less variability for C3 than was shown by the other cases. Although the amplitudes of wave 1 and 2 are similar and evolve similar to that of C1 and C2, waves 3 and 4 simply do not develop with anywhere near the intensity as shown in the previous cases. The former item we would expect, since waves 1 and 2 in the troposphere are controlled primarily by the orographic forcing, which is the same for both cases. The latter item may be one reason why many general

circulation models have their greatest problems in accurately predicting the evolution of the planetary waves (Sommerville, 1979).

CHAPTER 5

CONCLUSION

In this thesis, we have formulated a new model to examine the processes involved in a sudden stratospheric warming. We have simulated a major and a minor warming during forty day time integrations. We have looked at the momentum and heat budget contributions and the wave evolutions associated with these warmings. Finally, we have shown results indicating the importance of including the upper atmosphere in modeling efforts.

The model presented is innovative and can serve as a building block for even more sophisticated studies. Most spectral models that include a troposphere in sigma-coordinates have been based on $p_R = 0$ (e.g. Bourke, 1974; Hoskins and Simmons, 1975). Although this simplifies the resulting equations, it does not allow for enough definition in the upper atmosphere. By using two separate coordinate systems and $p_R \neq 0$, we can have detailed resolution of the stratosphere and mesosphere using log-pressure coordinates and still use the sigma-coordinates for the troposphere. These latter coordinates have excellent terrain handling properties (Kasahara, 1974) and they also simplify the specification of bottom boundary conditions.

The spectral form of the model lets us use semi-implicit time differencing, which in turn allows us to use larger time steps. Spherical harmonics also allow us to perform horizontal

differentiations, integrations, and fast Fourier transforms exactly up to the point of truncation. The model is also designed to conserve mass and energy by using appropriate vertical differencing schemes. This and the semi-implicit time differencing give the model the capability to perform long term integrations.

Currently, the biggest drawbacks of this model are the computer core size required and the large amount of computer time required to perform the time integrations. There are several areas that could be trimmed to reduce both of these requirements. The most important would be in divorcing various diagnostic and output routines from the main program. They could be run separately, independent of the main program. Another area that could be examined to promote greater efficiency is the requirement for 26 levels in the upper atmosphere. Experimentation might show that several levels could be eliminated, which would reduce both core size and save computational time. Greater efficiency might also be achieved by program consolidation which would allow for array reduction.

The model has great potential for future studies. If greater efficiency can be achieved, the model can be expanded in several ways. The most obvious expansion would be the inclusion of higher harmonics in the troposphere. Currently, the model is truncated at wave 4 and does not allow for the inclusion of the very important synoptic scale waves. The additional harmonics would let energy cascade to these meteorologically important wavenumbers. The stratosphere is probably sufficiently covered, as we can see by small wave 4 amplitudes that

developed in cases C1 and C2, and would not have to be expanded further. Another area of possible expansion would involve not assuming symmetry across the equator and consequently going to a true global model. This would allow for inclusion of topography representative of both hemispheres and also include transports across the equator. A third major area of future research would be the inclusion of more physics, such as moisture and differential heating parameterization. All of these modifications would add realism and subsequently even greater accuracy to the model results.

In our integrations of C1 and C2, we have demonstrated how sudden warmings can be initiated by orographic forcing. We have also shown how the evolution of these warmings is dependent upon the initial intensity of the polar night jet. Given the same degree of forcing, the weaker jet yields more easily to the forcing from below and this situation can more readily lead to a major sudden stratospheric warming. A stronger jet is at first less affected by forcing, but as the waves begin to extract energy from the large amount available in the mean flow, the warming can become very active. Until this point was reached, however, the initial evolution of C1 and C2 was quite similar. C1 later showed smaller amplitude waves with longer periodicity, especially at higher levels versus the larger and higher frequency characteristics of C2.

The stratospheric vacillations appear to be caused by the process of energy transfer resulting from wave to wave interactions. Although wave and mean flow interactions may also account for a certain degree of

vacillation, especially during the early stages of our integrations, it cannot account for the much higher frequency oscillations produced in C2. By comparing wave growth and decay among the planetary waves, the importance of the wave to wave interactions to the vacillation process is quite evident. Because of the inability to sustain a process for a long enough period in a highly vacillating regime with significant wave transience, the C2 warming most probably did not become major.

Our integrations certainly support the indirect cell mechanism as outlined by Matsuno (1971) as the prime ingredient in the warming process. Although the large terms involved in momentum and heat budgets tend to cancel, a slight imbalance between them can cause large changes in zonal wind and temperature. Sometimes they do receive support from the smaller contributors to these budgets, which become increasingly important when the larger terms effectively negate one another.

It is still difficult to conclude whether wave 1 as supported by Labitzke (1977, 1978) or wave 2 as supported by Schoeberl and Strobel (1980b) is most important in the warming process. The C1 warming showed a greater wave 2 tendency with its split vortex in contrast with C2, which was more aligned with wave 1. However, the time sections for both cases tend to indicate that indirect cells develop, westerlies decelerate, and temperatures increase most frequently when wave 1 is amplifying and while wave 2 is decaying. It appears then that it is the push from an intensifying wave which causes the sudden changes and in this context both waves 1 and 2 are important since each can serve

as an energy source for the other because of wave to wave interactions. Wave 3 aided in this exchange of energy serving as a source of dissipation as proposed by Perry (1967) and also as an interloper linking waves 1 and 2.

In the troposphere, changes were not as dynamic as the upper atmosphere, probably due to the anchoring of topography and truncation at wave 4. To some extent the troposphere did reflect the stratospheric warming event with smaller but similar changes in zonal velocity and temperature at both high and low latitudes. The main differences between C1 and C2 in the troposphere were the increased wave 3 and 4 activity of C2, the larger warming of polar regions that occurred with C1, and the easterlies which also appeared in the polar regions of C1. In both C1 and C2, there was some tendency of tropospheric geopotentials to lead stratospheric peaks.

Finally, our results indicate the need for the inclusion of some upper atmospheric parameterization to aid in long range wintertime tropospheric predictions. Interactions between the troposphere and stratosphere resulted in enhanced wave activity at higher wavenumbers which was proportional to the strength of the polar night jet. The troposphere also reflected the temperature and zonal wind changes that occur during sudden warmings in the stratosphere. The location and movement of tropospheric jet maxima also tended to behave differently and more erratically when the upper atmosphere contributions were neglected. The troposphere is not separated from the stratosphere in nature and cannot be separated in the modeling process if we want to accurately predict dynamic meteorological phenomena.

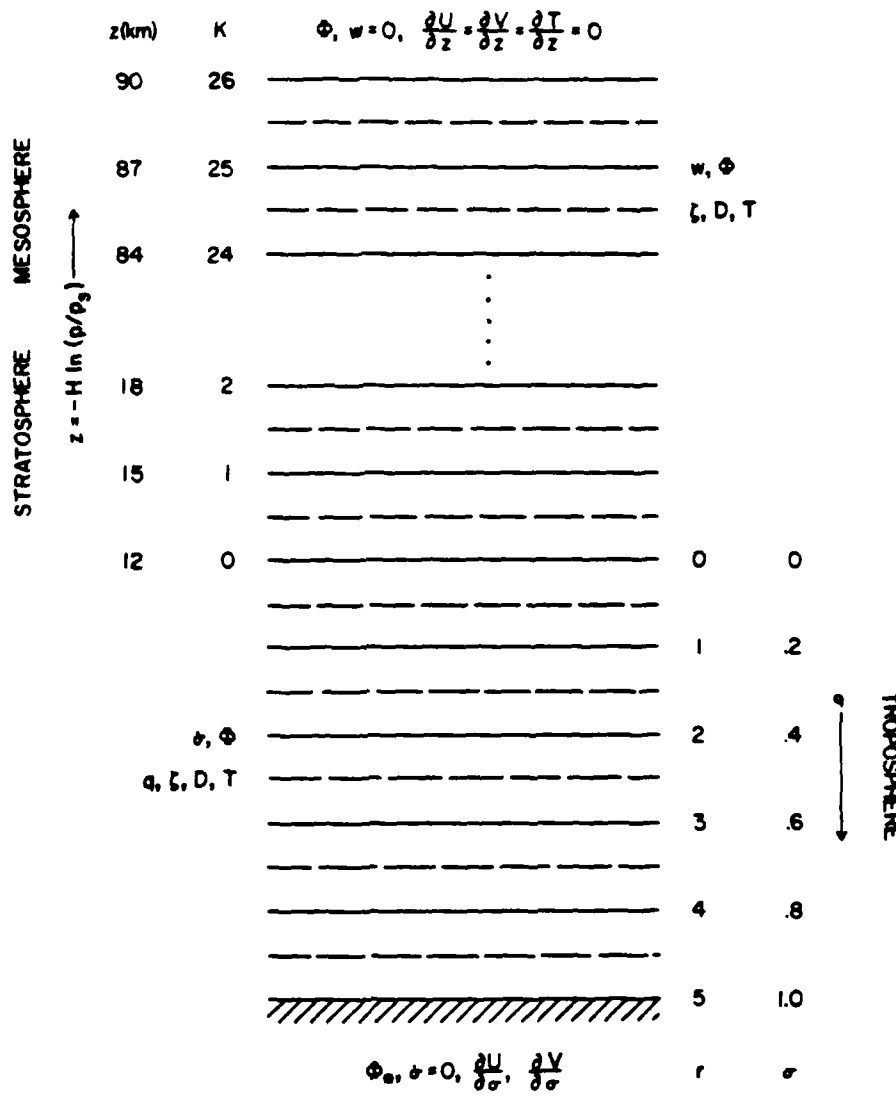


Figure 1. Model Schematic. Dashed/solid lines represent prognostic/diagnostic levels respectively. Boundary conditions are specified at top and bottom boundaries.

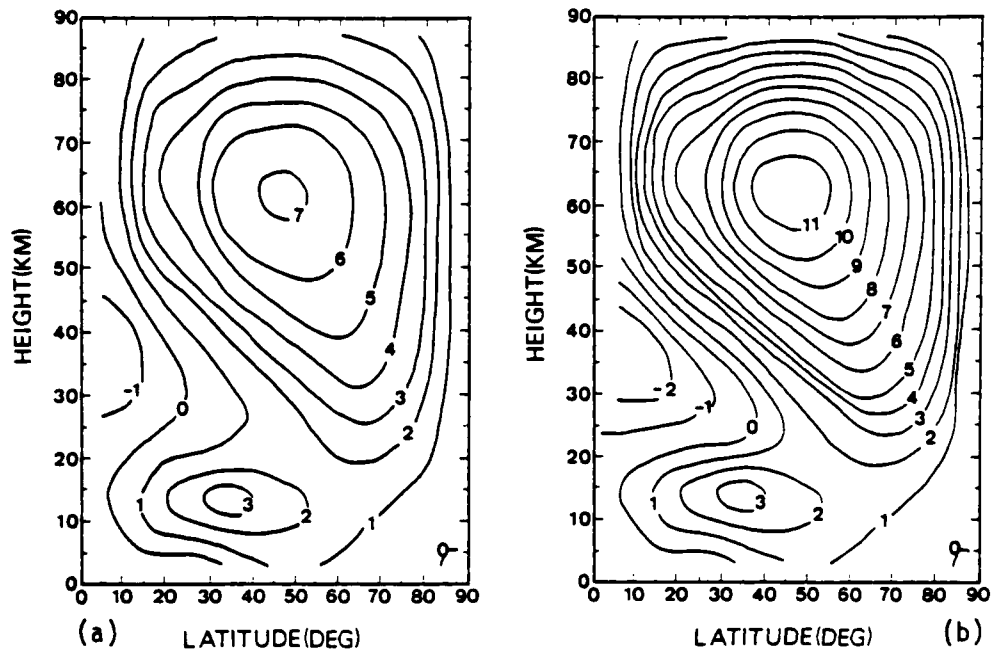


Figure 2. Latitude-height sections of initial mean zonal wind ($\times 10 \text{ m s}^{-1}$) for (a) Case 1; and (b) Case 2.

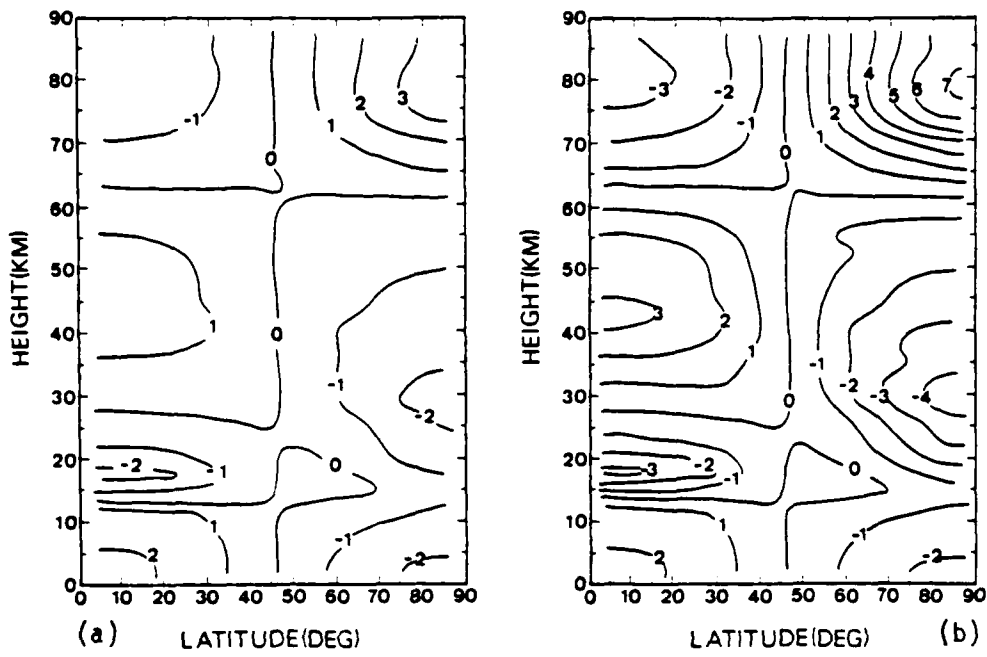


Figure 3. Latitude-height sections of the initial zonal mean temperature deviations ($\times 10^{\circ}\text{K}$) for (a) Case 1; and (b) Case 2.

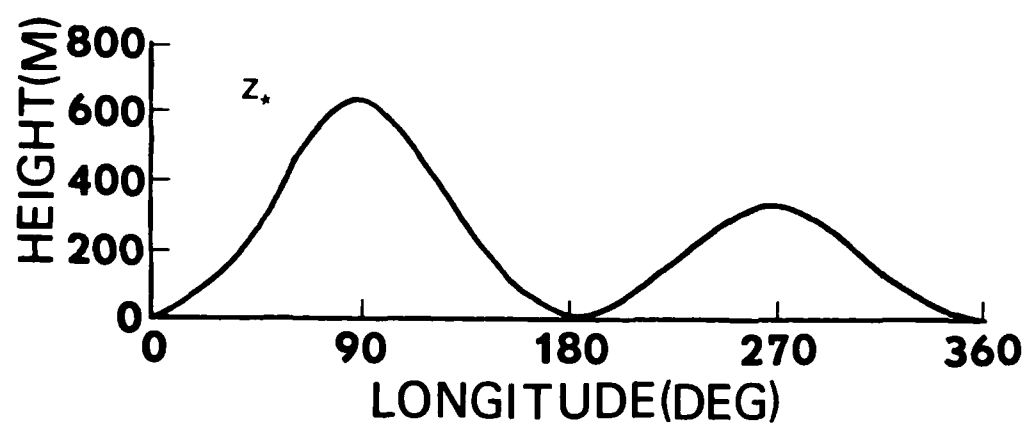


Figure 4. Maximum longitudinal surface height distribution at 45°N.

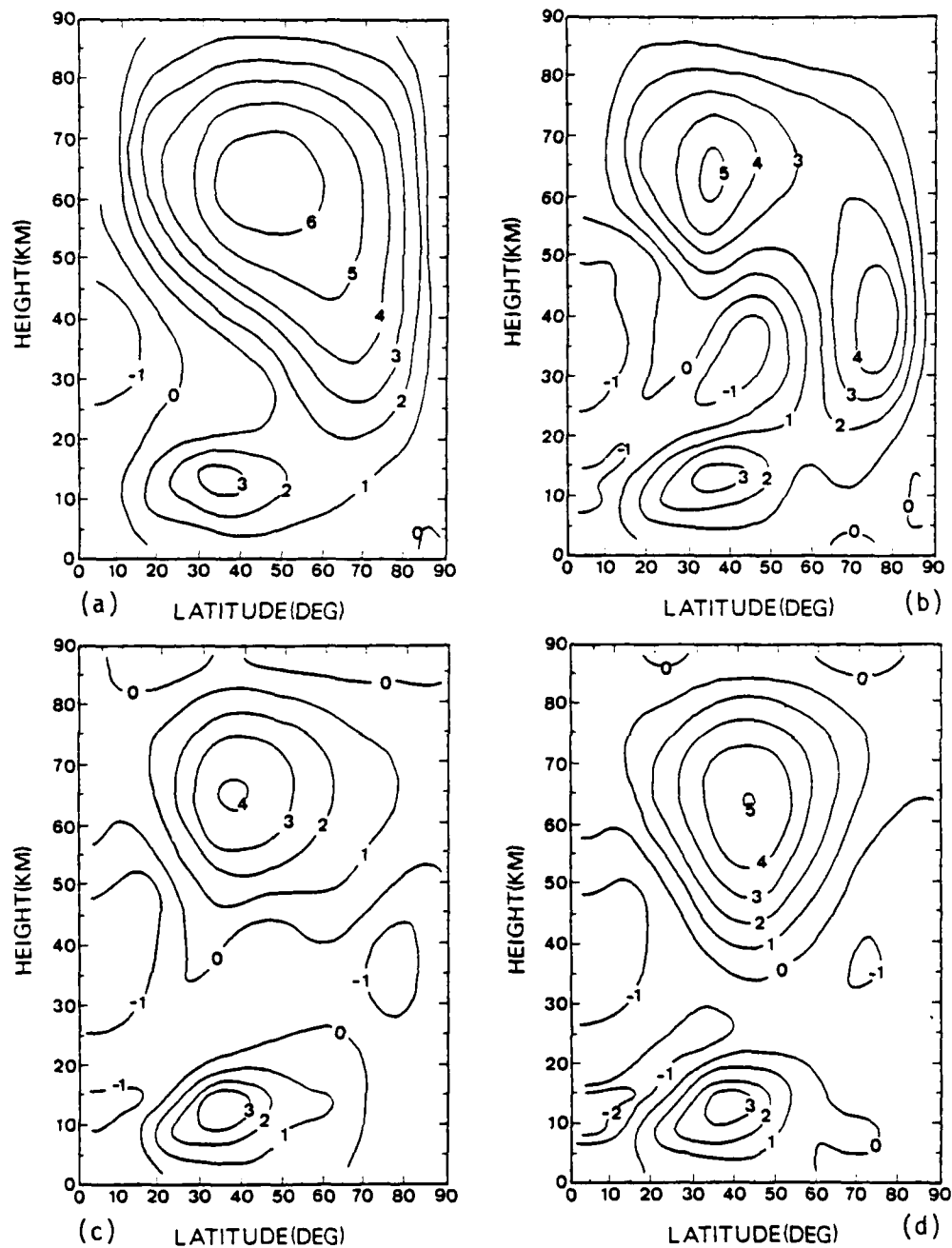


Figure 5. Latitude-height sections of the mean zonal wind ($\times 10 \text{ m s}^{-1}$) for C1 on (a) day 10; (b) day 20; (c) day 30; and (d) day 40.

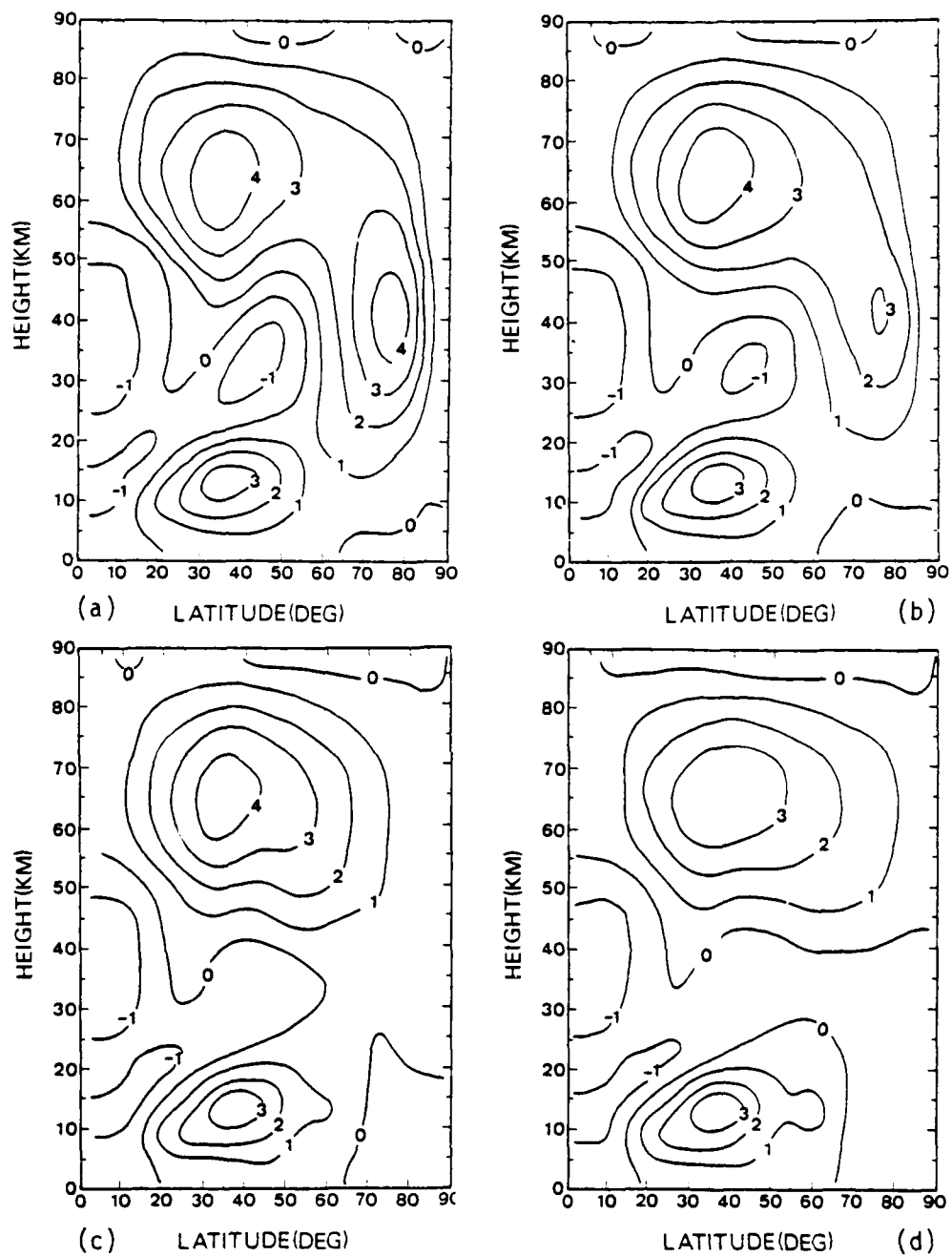


Figure 6. Same as Fig. 5 except on (a) day 22; (b) day 24; (c) day 26; and (d) day 28.

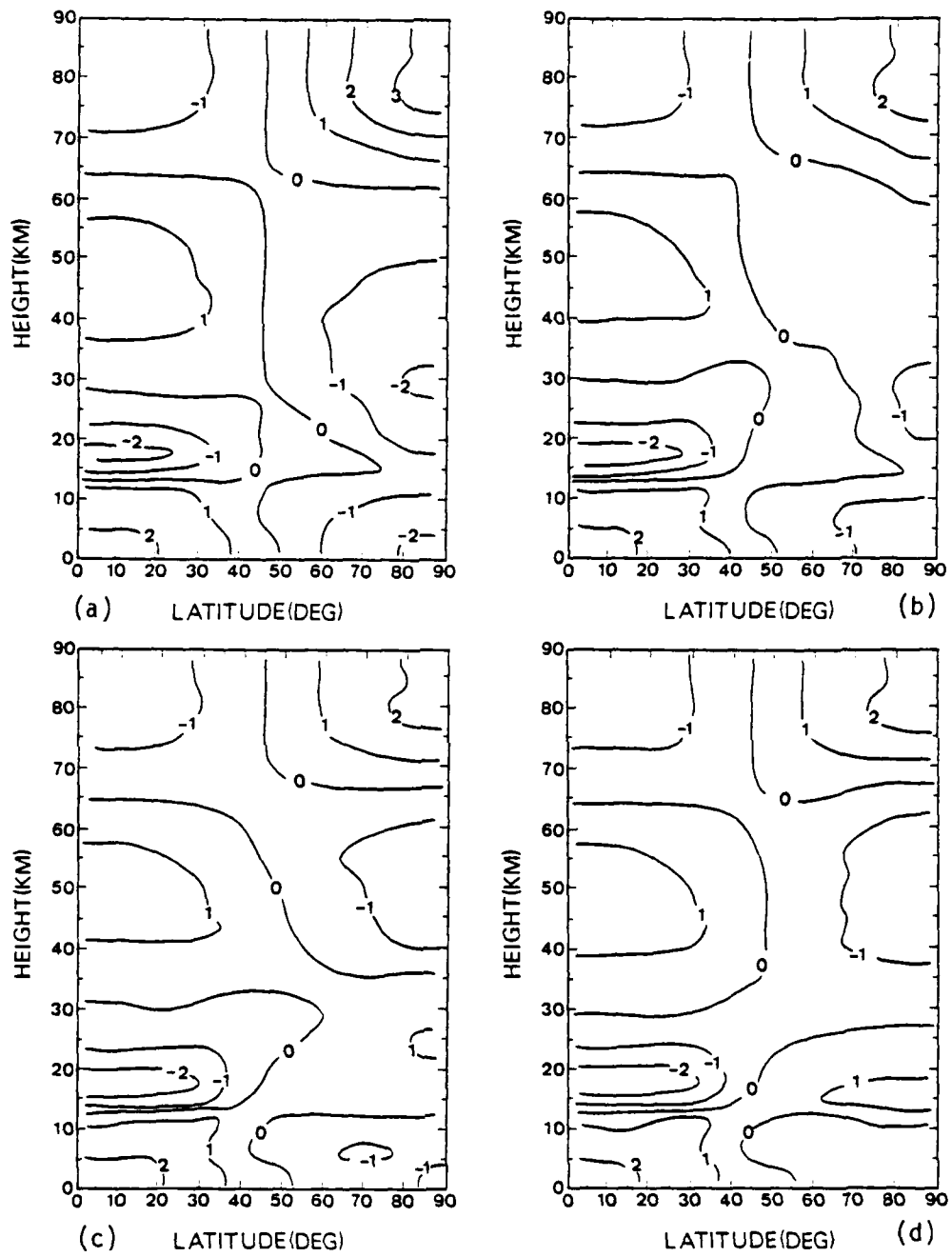


Figure 7. Latitude-height sections of zonal mean temperature deviations ($\times 10^3$ K) for C1 on (a) day 10; (b) day 20; (c) day 30; and (d) day 40.

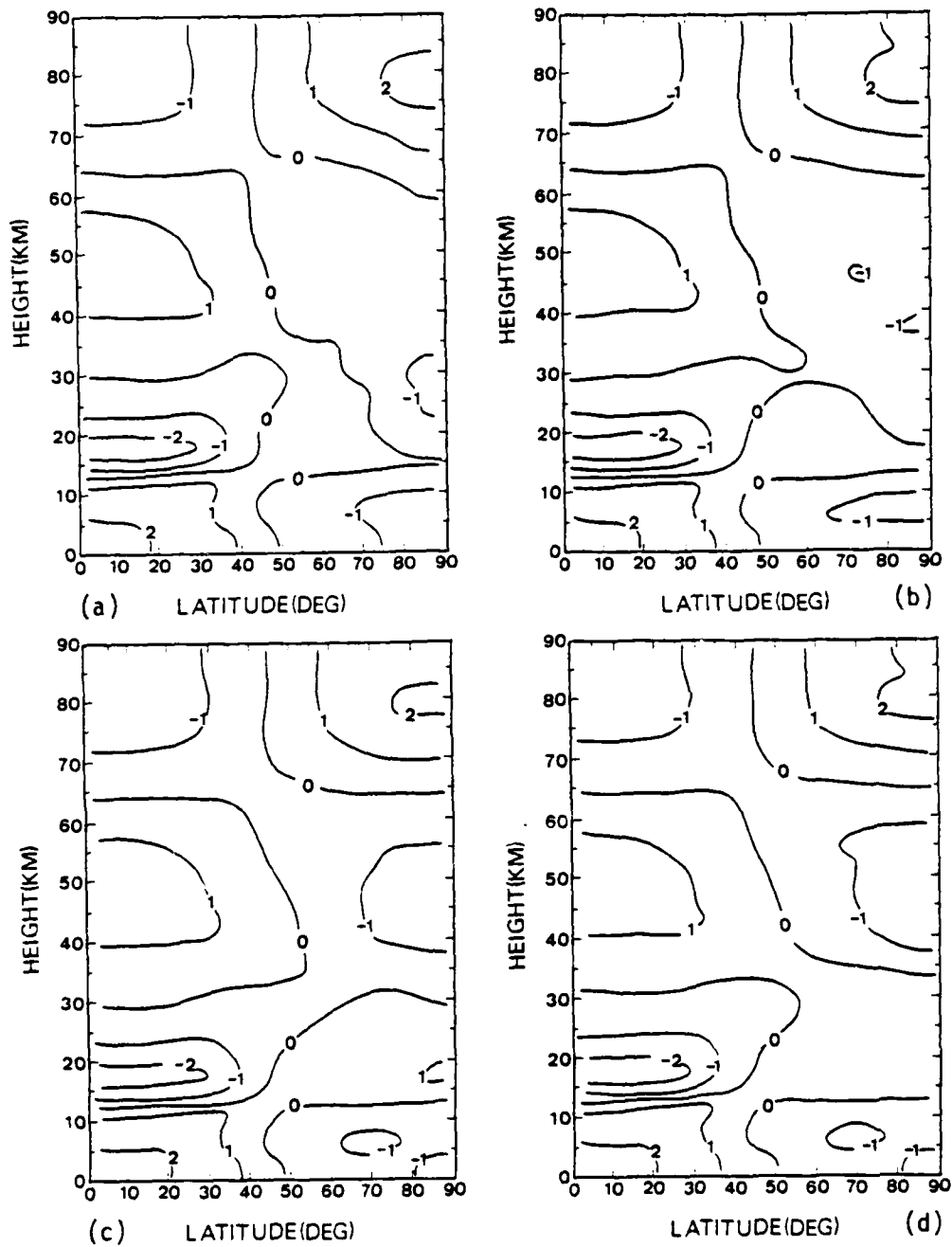


Figure 8. Same as Fig. 7 except on (a) day 22; (b) day 24;
(c) day 26; and (d) day 28.

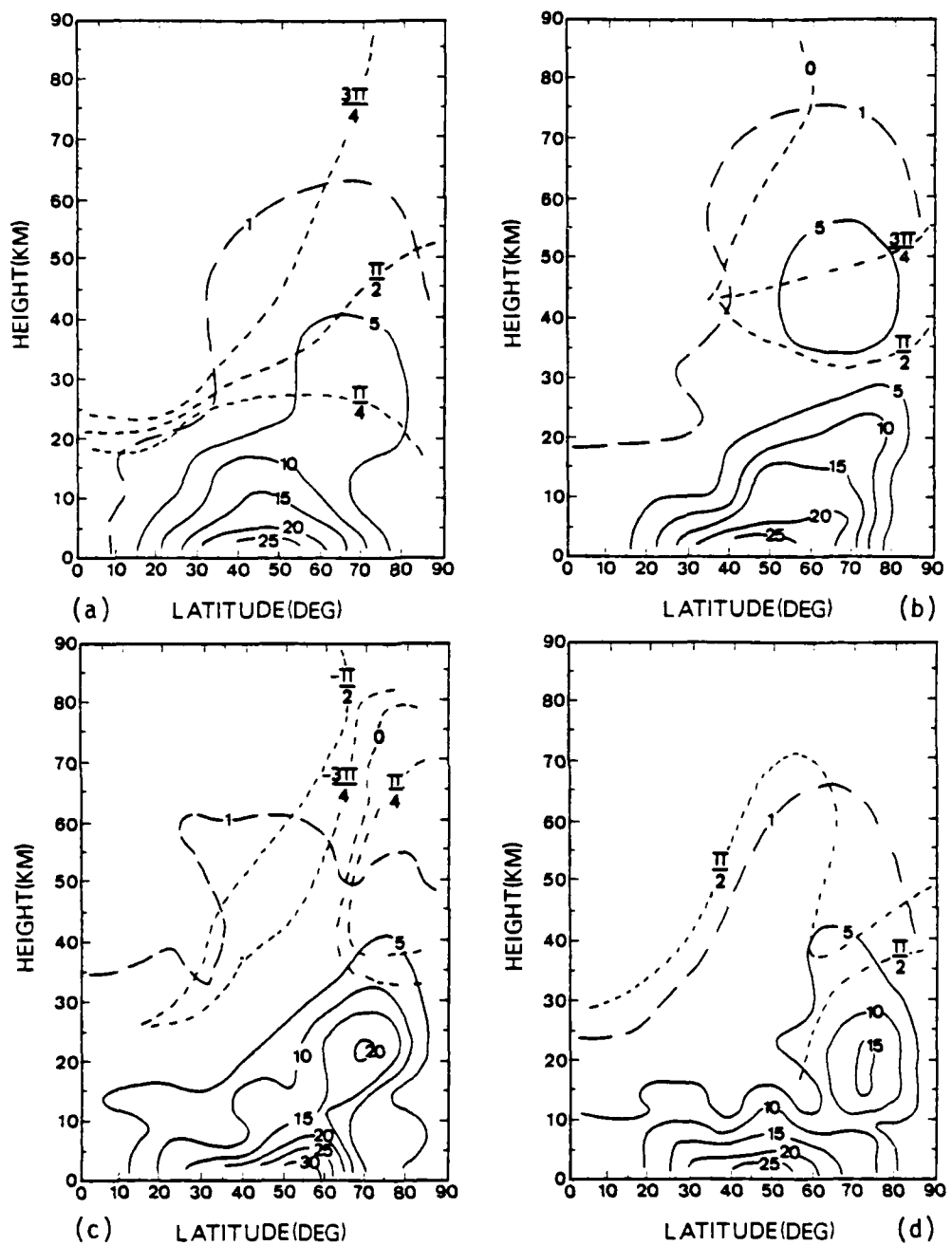


Figure 9. C1 latitude-height sections of $|\phi_1|$ ($\times 10^2 \text{ m}^2 \text{ s}^{-2}$) indicated by solid lines (except for $|\phi_1| = 100$ represented by long dashed lines) with the ϕ_1 phase angle (radians) indicated by short dashed lines for (a) day 10; (b) day 20; (c) day 30; and (d) day 40.

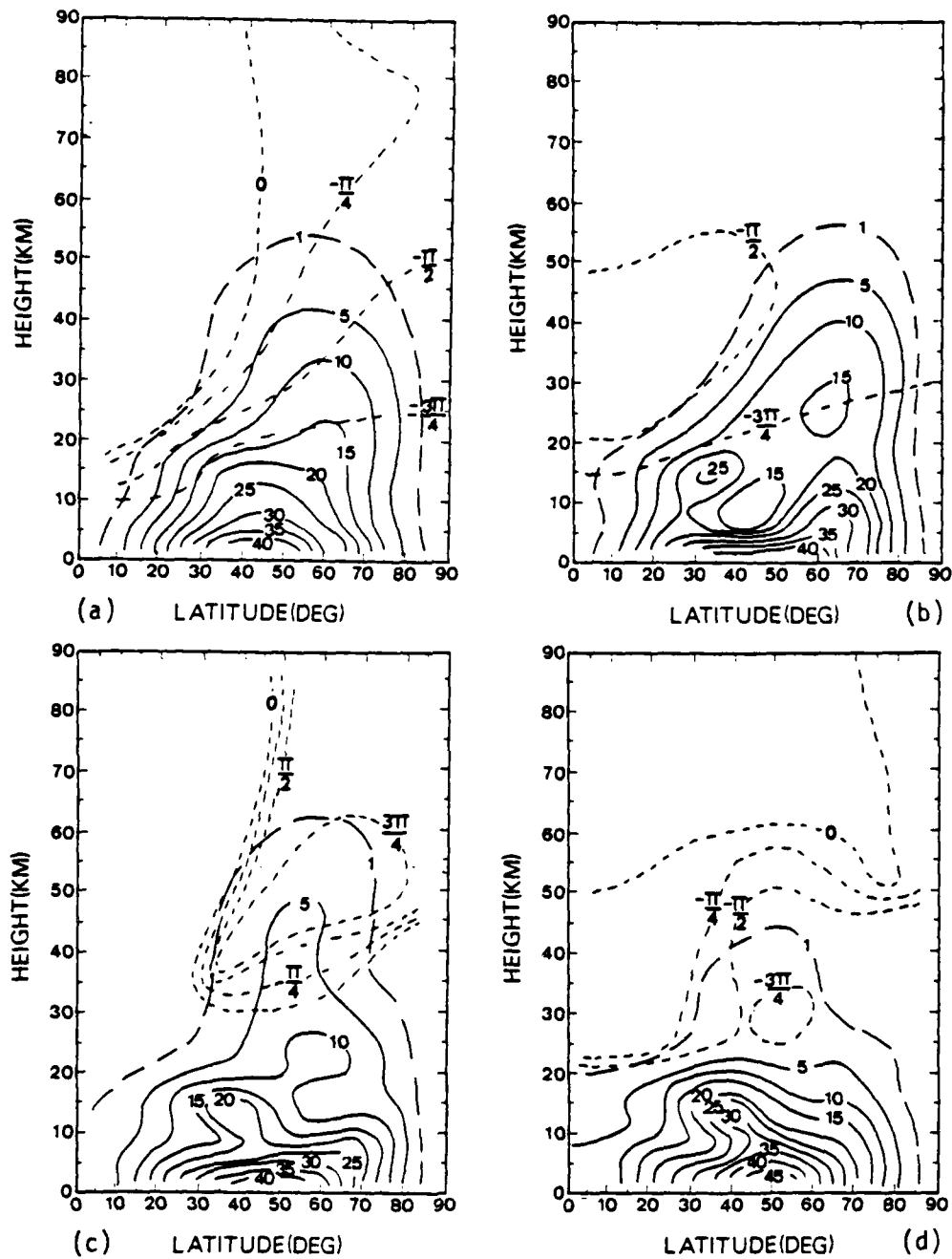


Figure 10. Same as Fig. 9 except for Φ_2 .

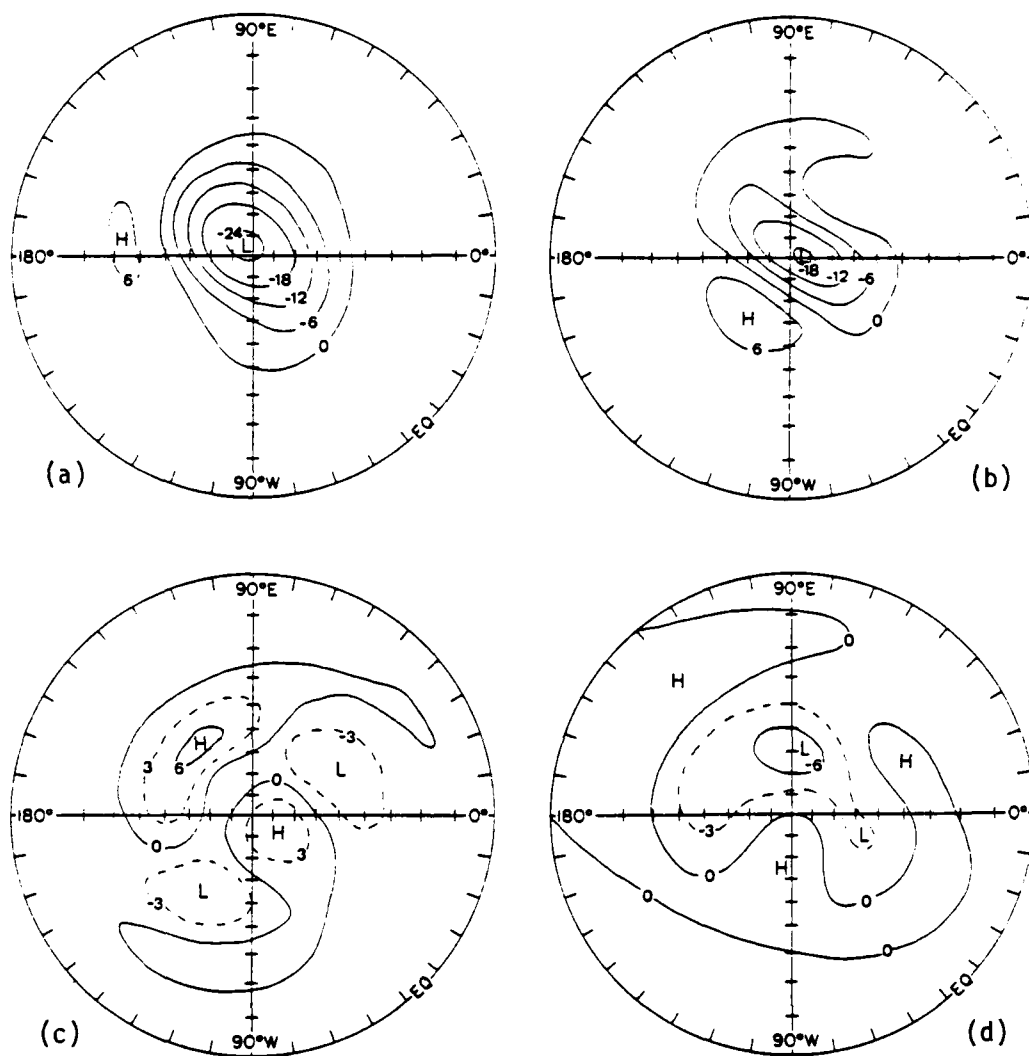


Figure 11. Polar stereographic projections of height deviations ($\times 10^2$ m) at 40.5 km for C1 on (a) day 10; (b) day 20; (c) day 30; and (d) day 40.

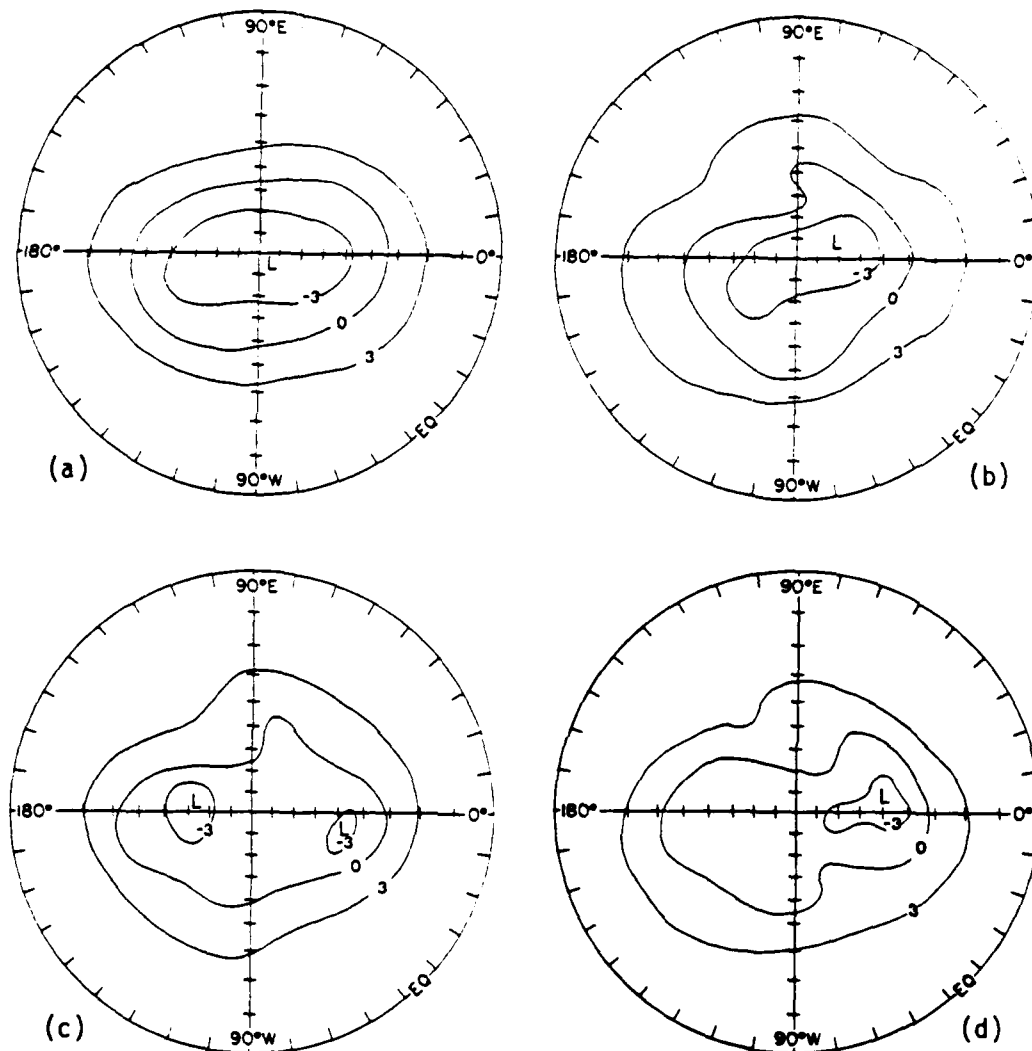


Figure 12. Same as Fig. 11 except at approximately 6.7 km.

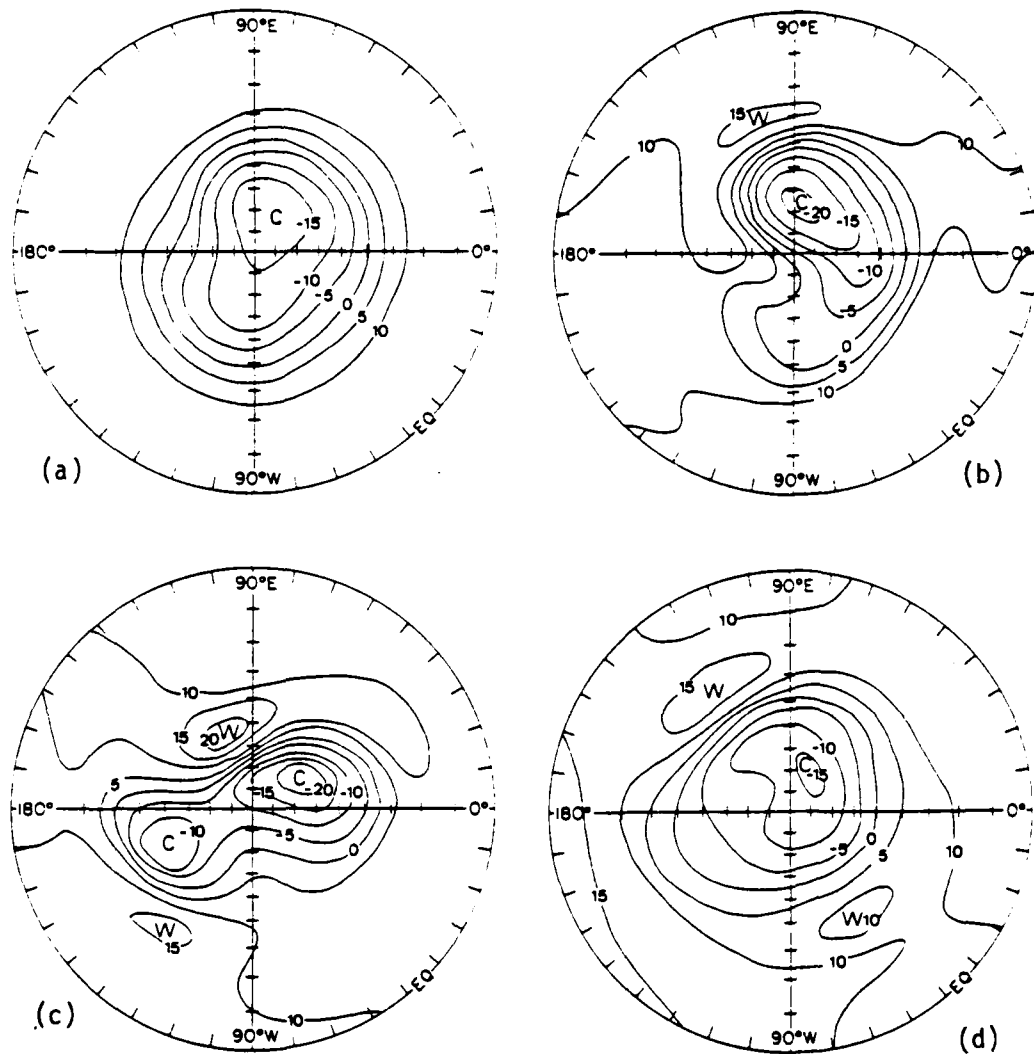


Figure 13. Polar stereographic projections of temperature deviations ($^{\circ}\text{K}$) at 40.5 km for C1 on (a) day 10; (b) day 20; (c) day 30; and (d) day 40.

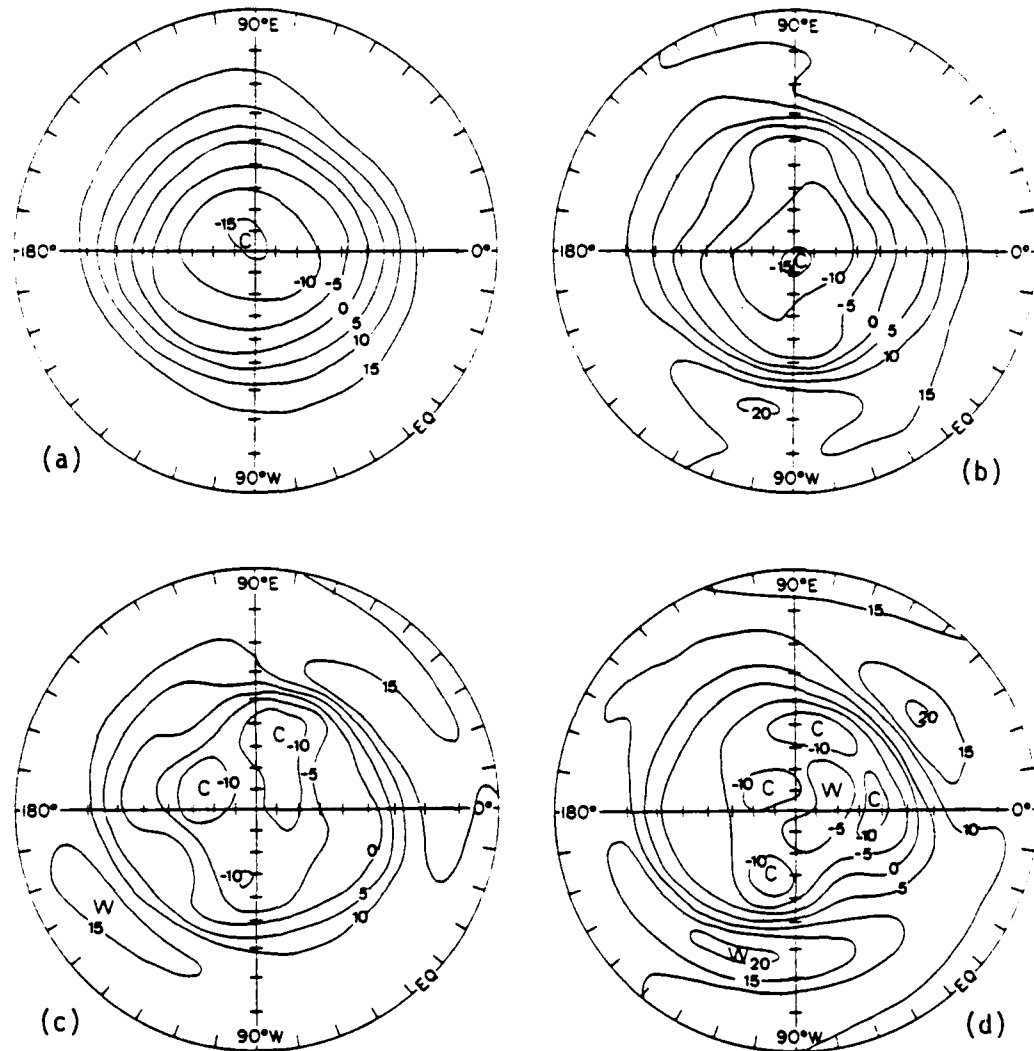


Figure 14. Same as Fig. 13 except at approximately 6.7 km.

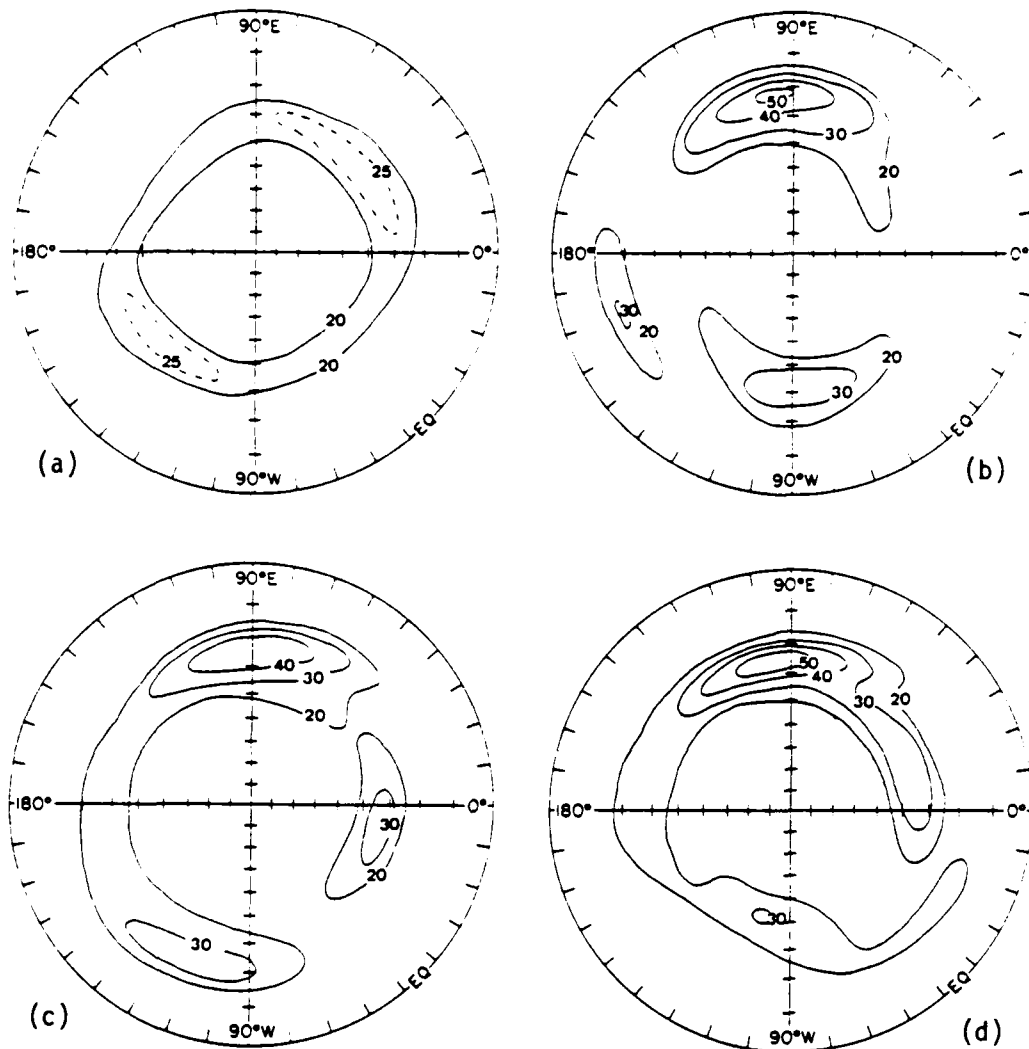


Figure 15. C1 polar stereographic projections of the zonal wind component (m s^{-1}) for values greater than or equal to 20 m s^{-1} on (a) day 10; (b) day 20; (c) day 30; and (d) day 40.

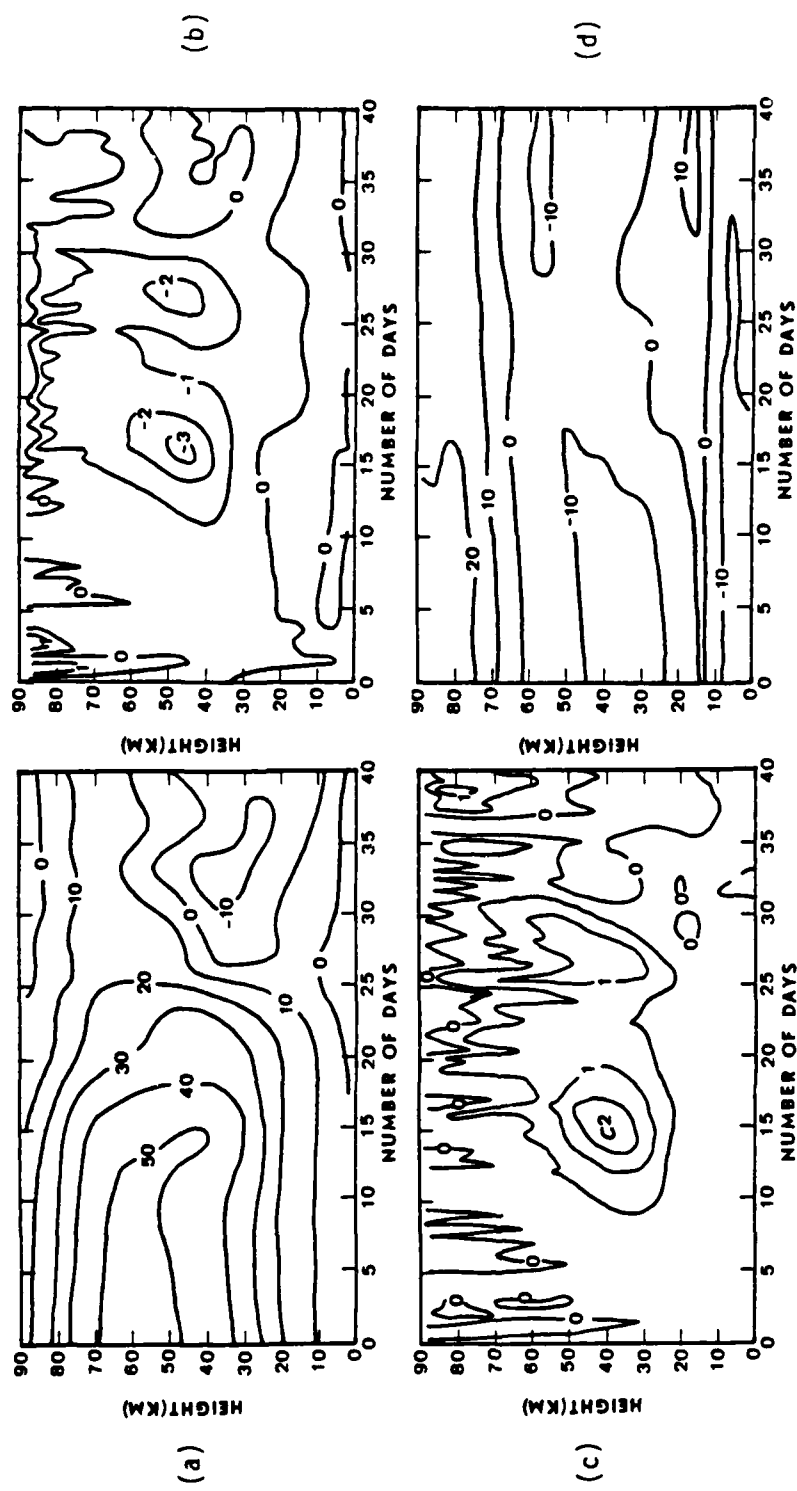


Figure 16. C1 height-time sections at 68.9°N of (a) mean zonal wind (m s^{-1}); (b) zonal mean meridional velocity component (m s^{-1}); (c) zonal mean vertical velocity ($\times 10^{-1} \text{ m s}^{-1}$); and (d) zonal mean temperature deviation ($^{\circ}\text{K}$).

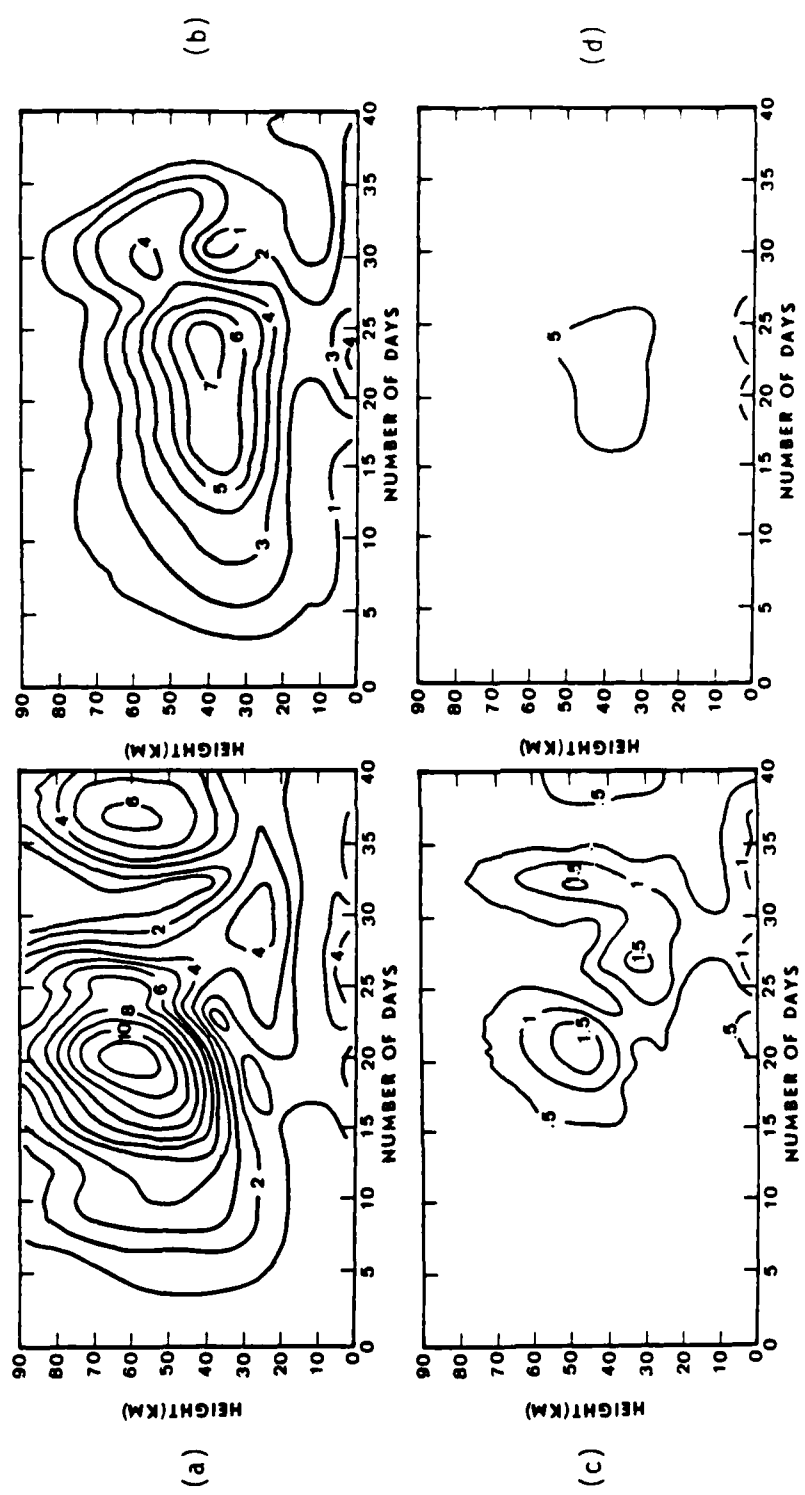


Figure 17. C1 height-time sections at 68.9 N of (a) $|\phi_1|$; (b) $|\phi_2|$; (c) $|\phi_3|$; and (d) $|\phi_4|$. Units are $10^3 \text{ m}^2 \text{ s}^{-2}$.

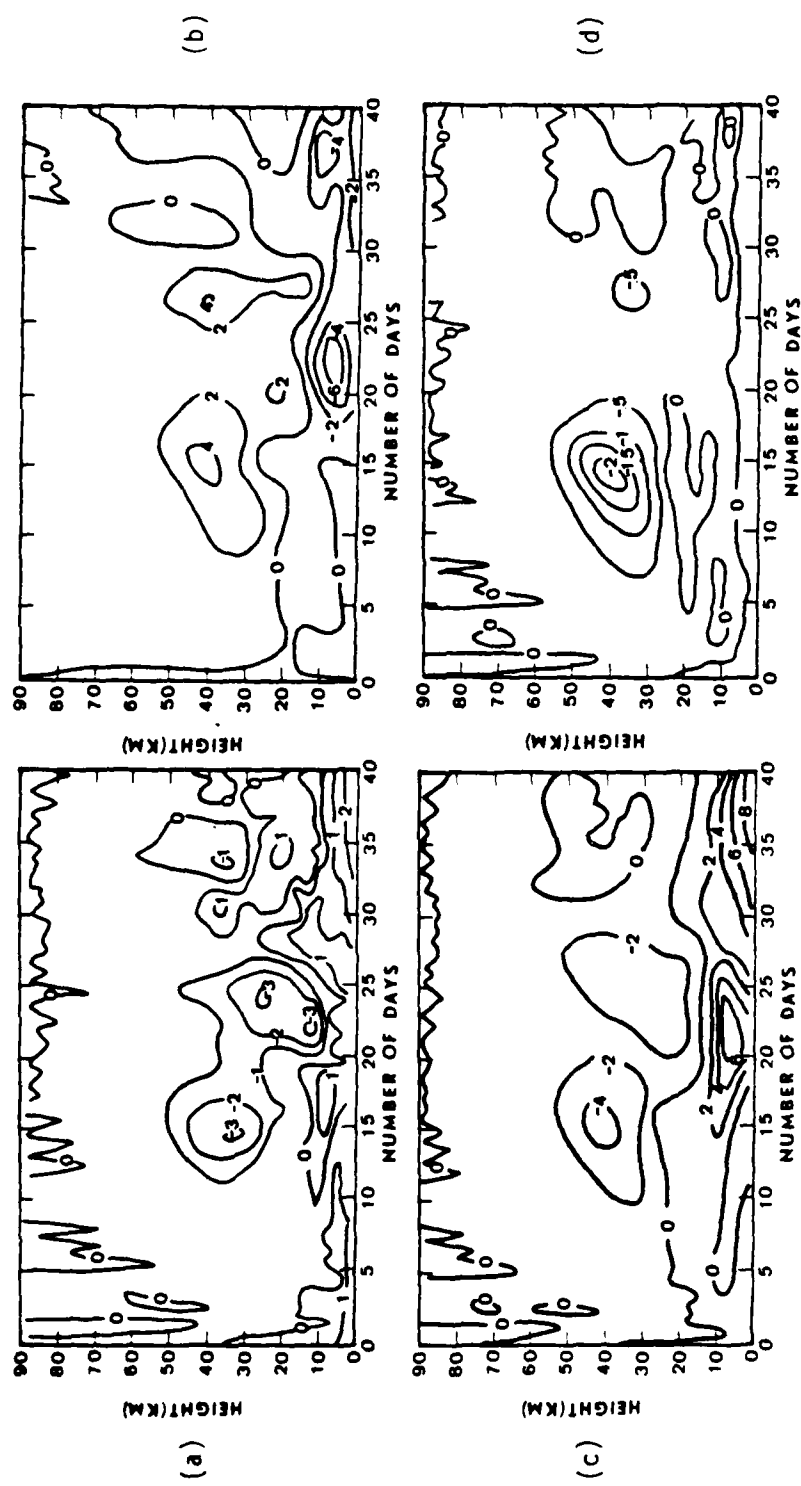


Figure 18. C1 height-time sections of (a) $\partial \bar{u} / \partial t$; (b) $\partial \bar{u} / \partial t$; (c) $\partial \bar{v} / \partial t$; (d) $\partial \bar{v} / \partial t$. Units are 10^{-4} m s^{-2} .

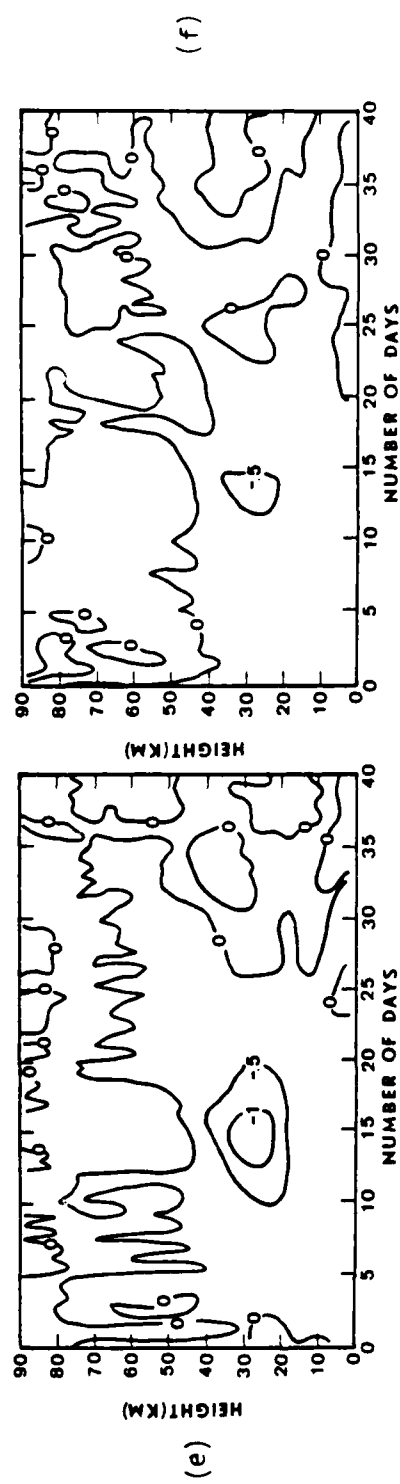


Figure 18 (continued). (e) FA; and (f) FE.

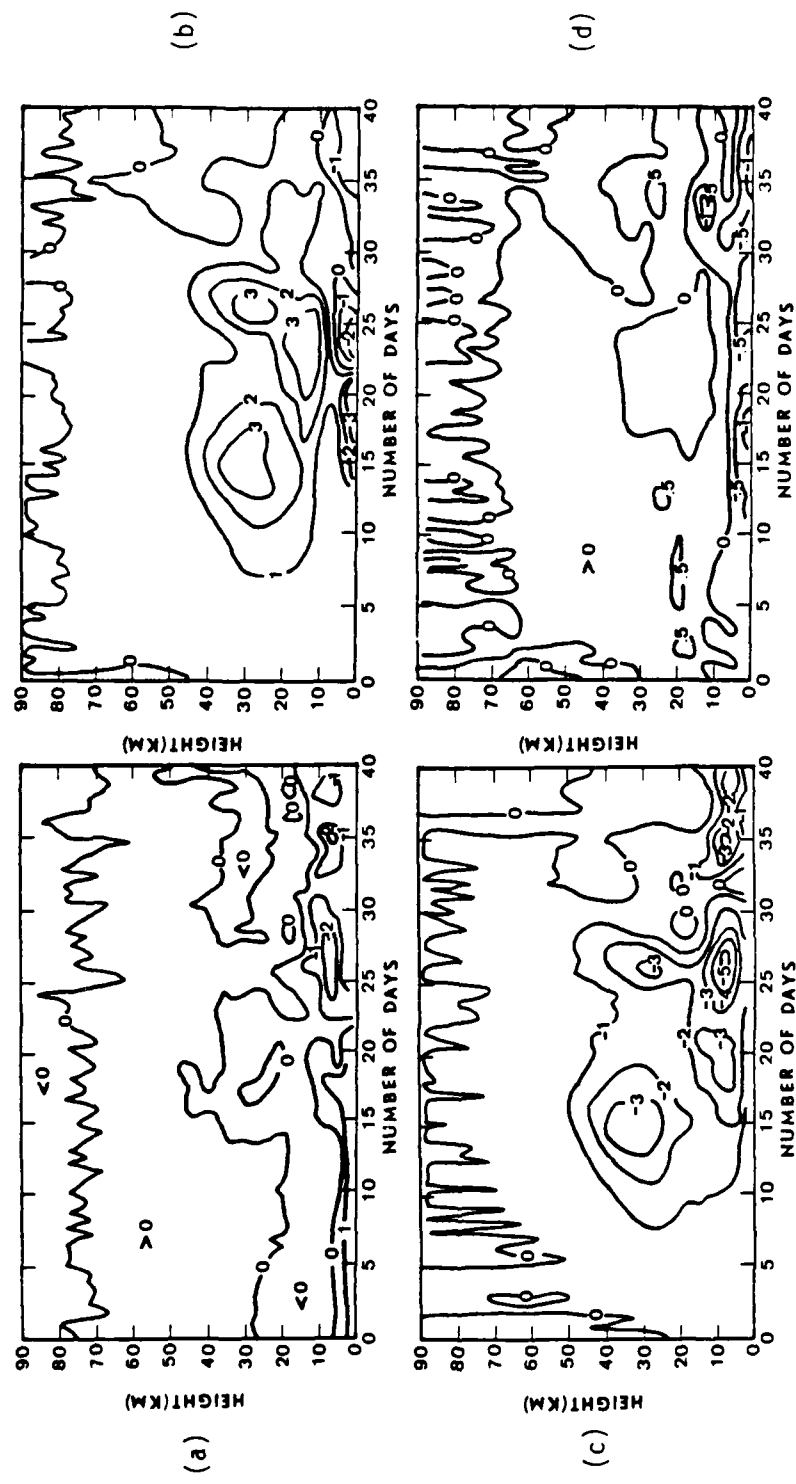


Figure 19. C1 height-time sections at 68.9°N of (a) $\partial\bar{T}/\partial t$; (b) VTP; (c) VTB; (d) HWB. Units are $10^{-4} \text{ }^{\circ}\text{K s}^{-1}$.

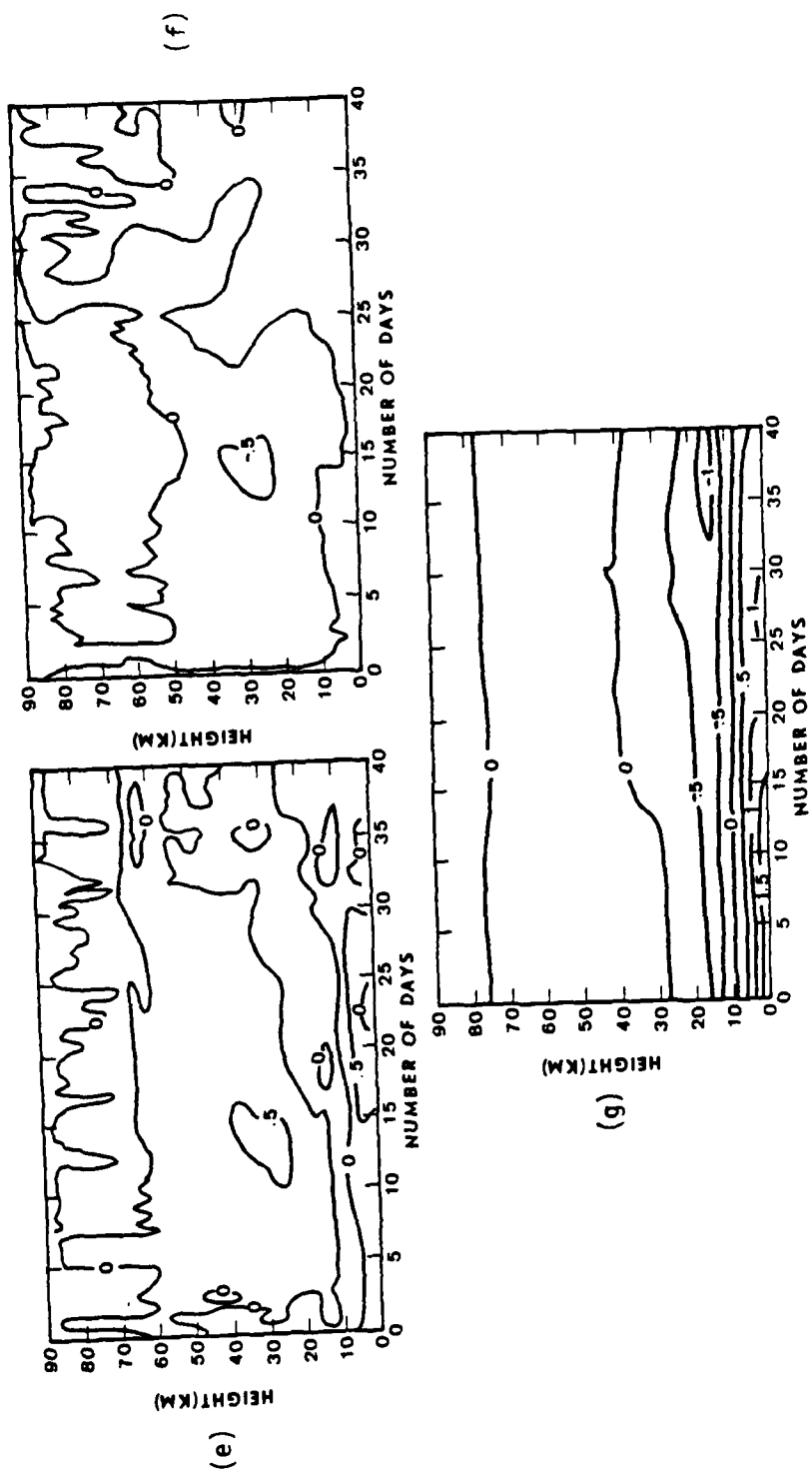


Figure 19 (continued). (e) WTB; (f) WTP; and (g) HNA.

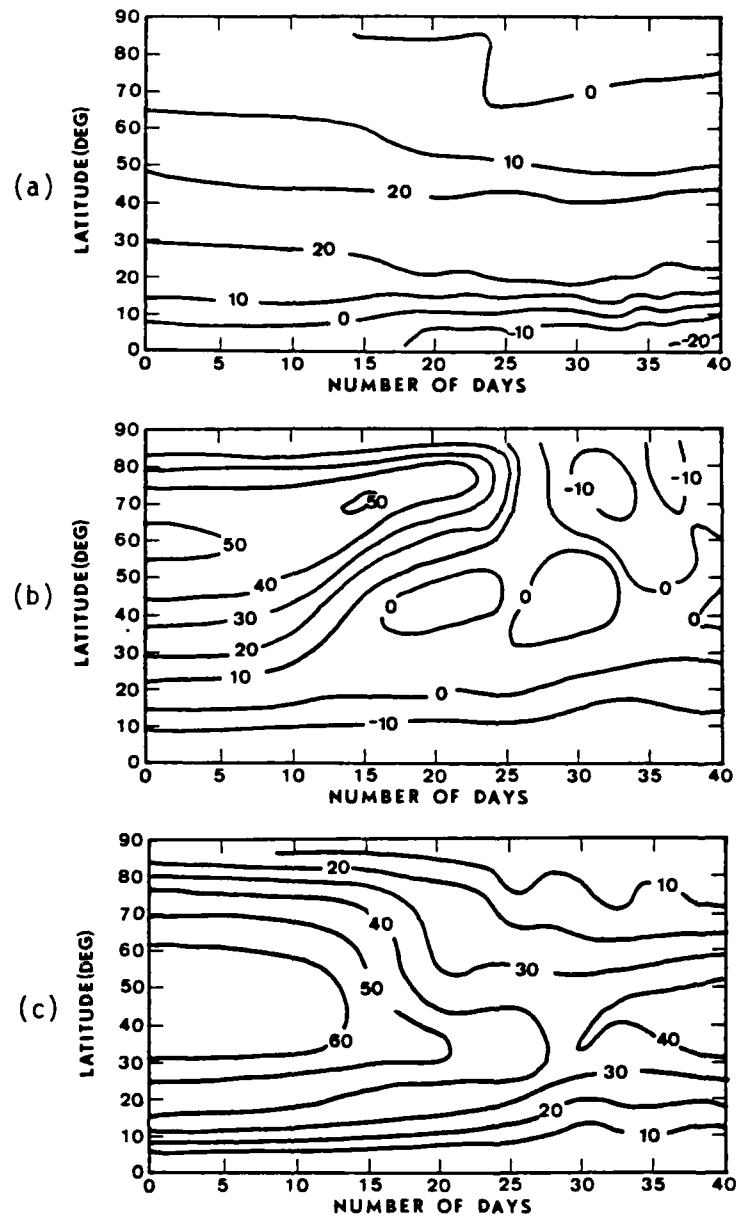


Figure 20. C1 latitude-time section of mean zonal wind ($m s^{-1}$) at (a) 7.5 km; (b) 40.5 km; and (c) 67.5 km.

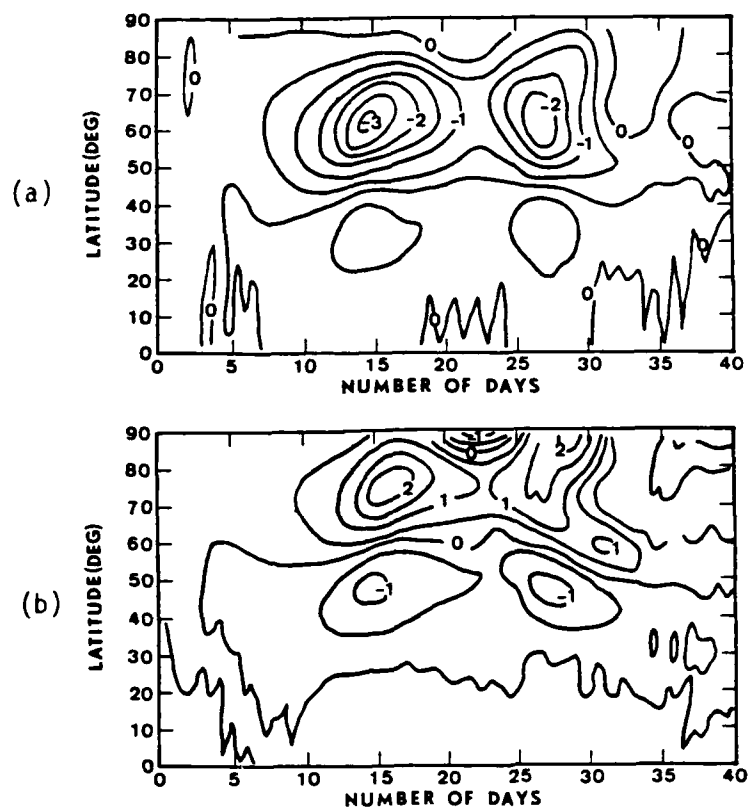


Figure 21. C1 latitude-time sections at 40.5 km of (a) the zonal mean meridional velocity component (m s^{-1}) and (b) the zonal mean vertical velocity ($\times 10^{-1} \text{ m s}^{-1}$).

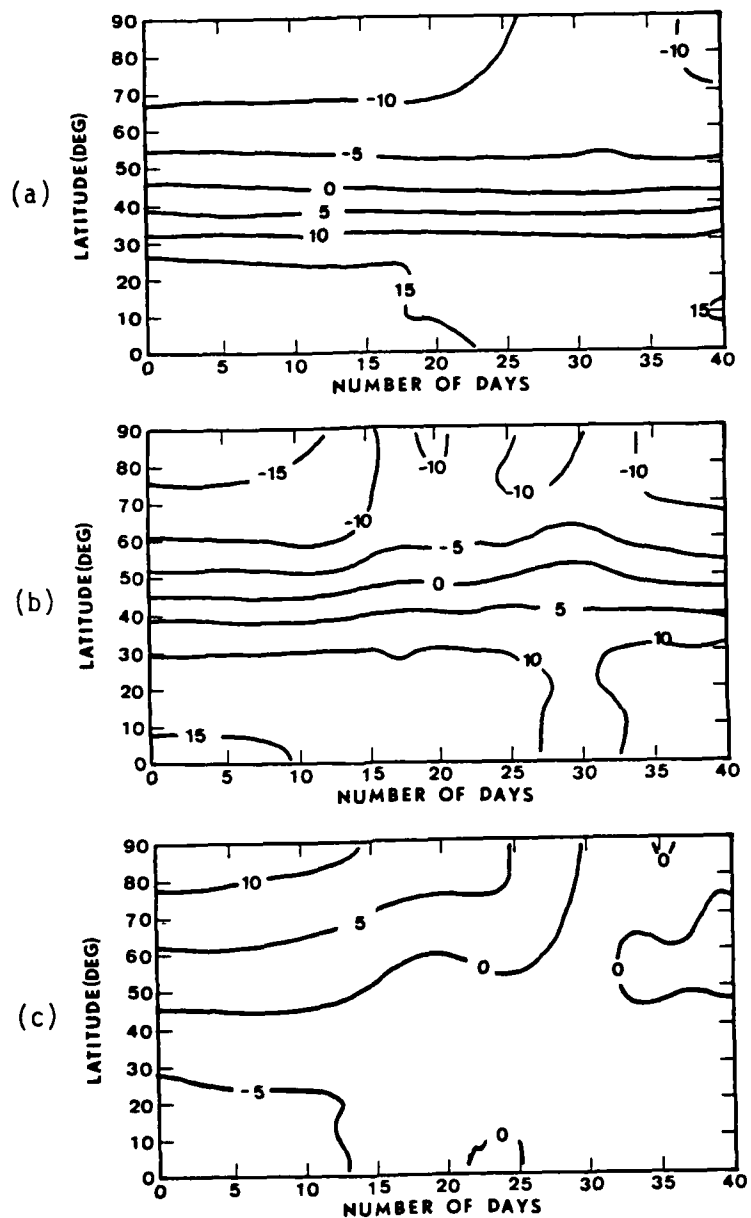


Figure 22. C1 latitude-time sections of zonal mean temperature deviation ($^{\circ}\text{K}$) at (a) 7.5 km; (b) 40.5 km; and (c) 67.5 km.

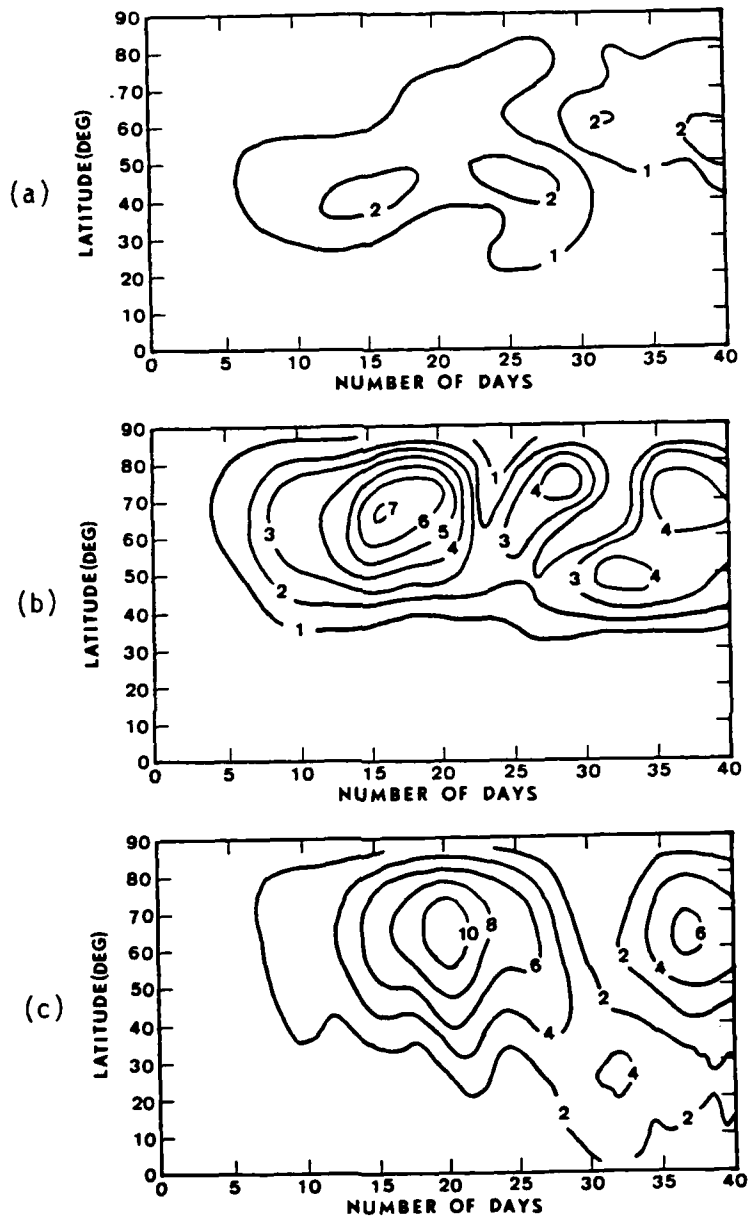


Figure 23. C1 latitude-time section of $|\Phi_1|$ ($\times 10^3 \text{ m}^2 \text{ s}^{-2}$) at
 (a) 7.5 km; (b) 40.5 km; and (c) 67.5 km.

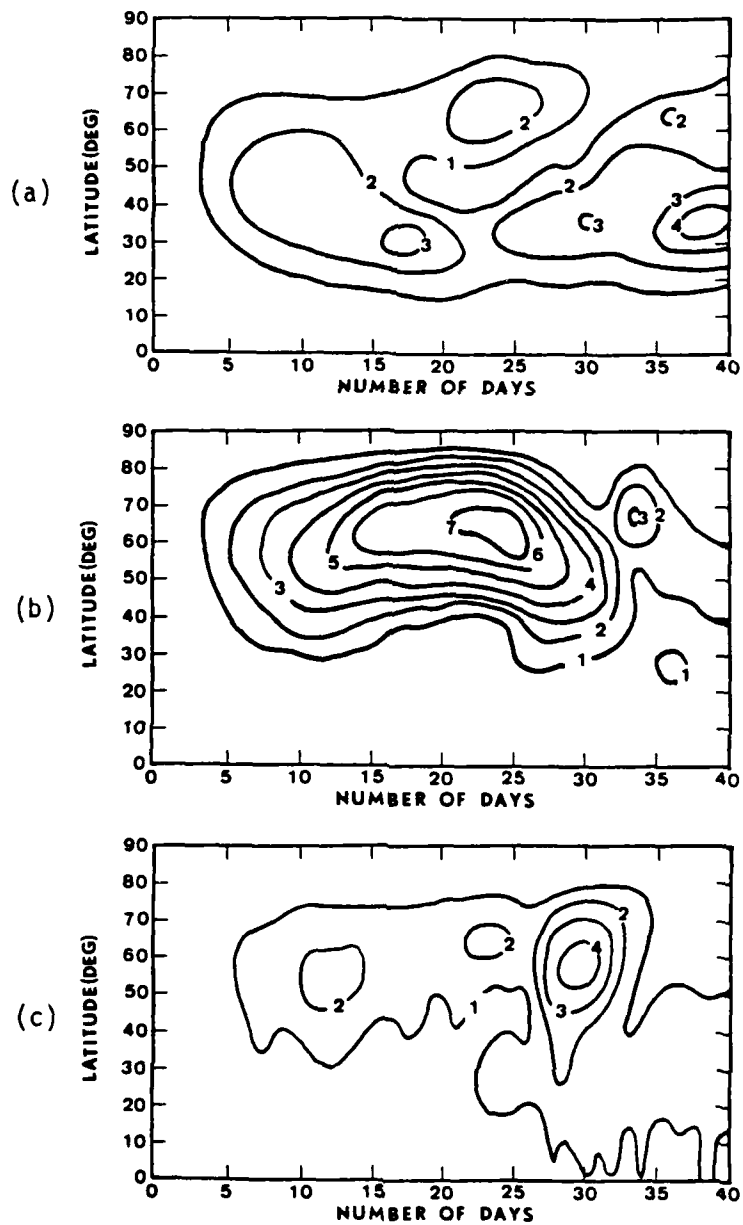


Figure 24. Same as Fig. 23 except for $|\Phi_2|$.

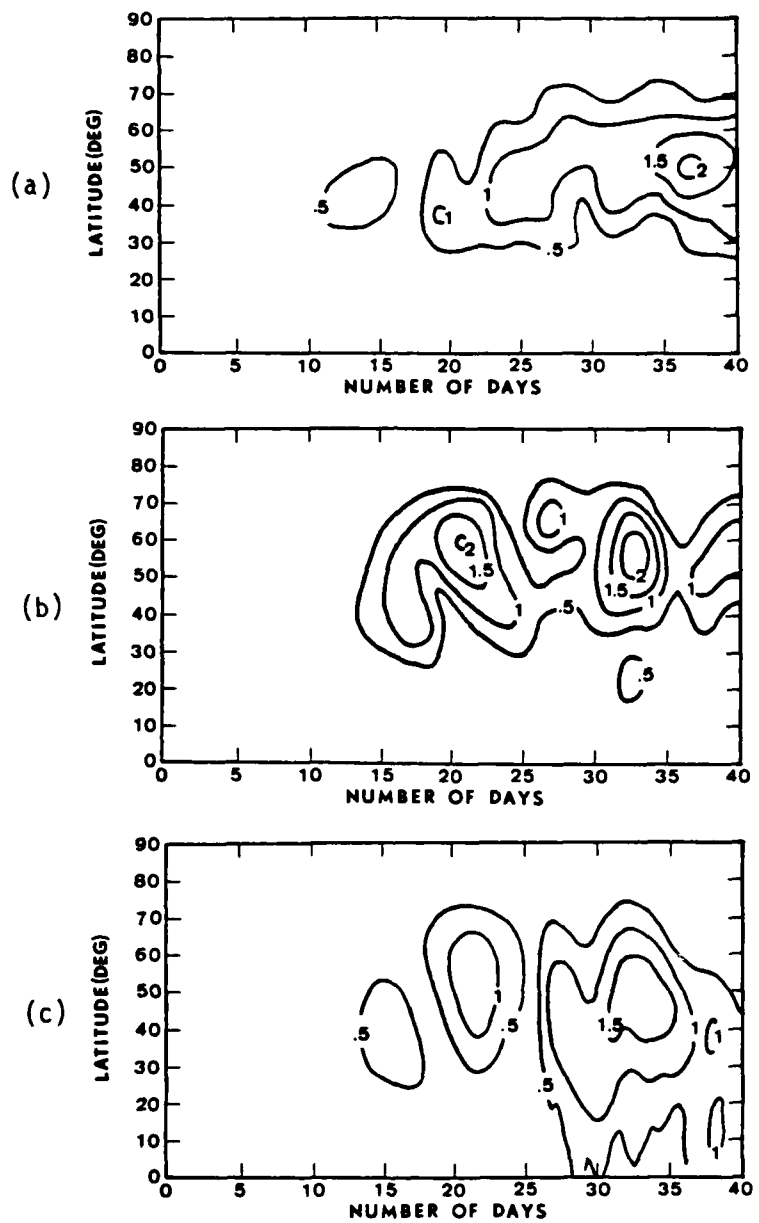


Figure 25. Same as Fig. 23 except for $|\phi_3|$.

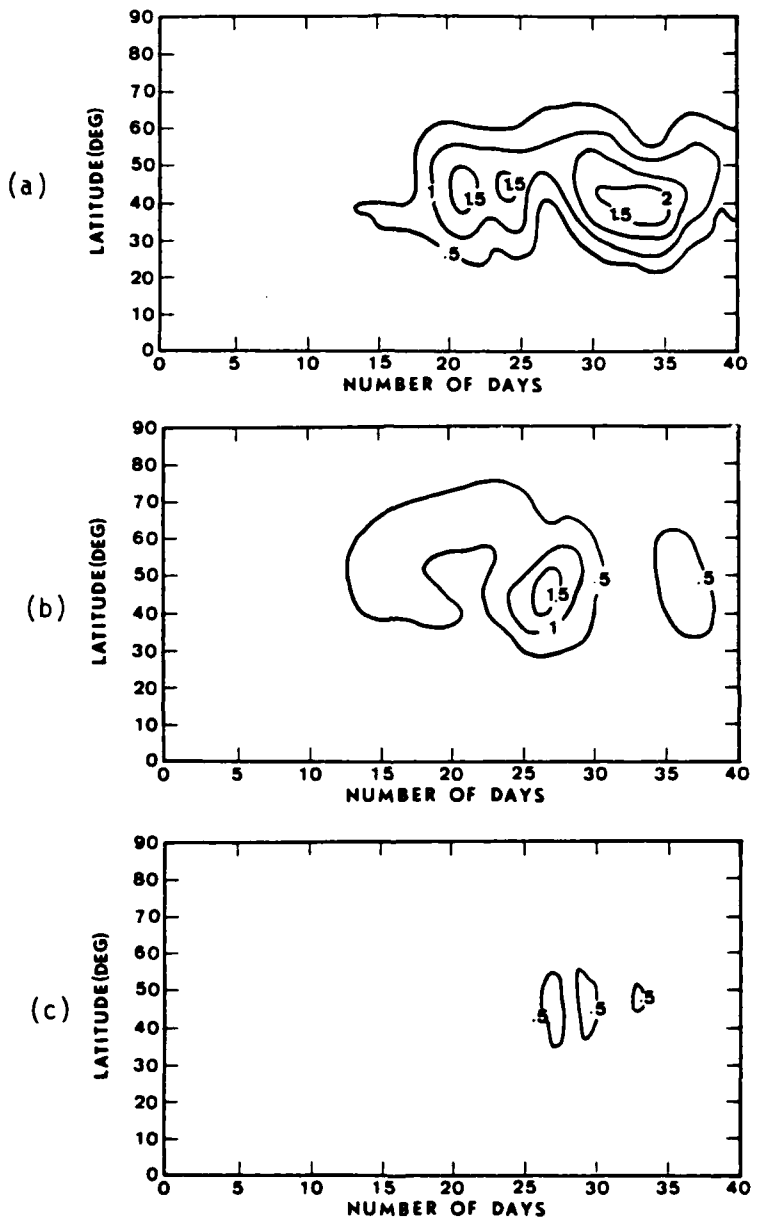


Figure 26. Same as Fig. 23 except for $|\Phi_4|$.

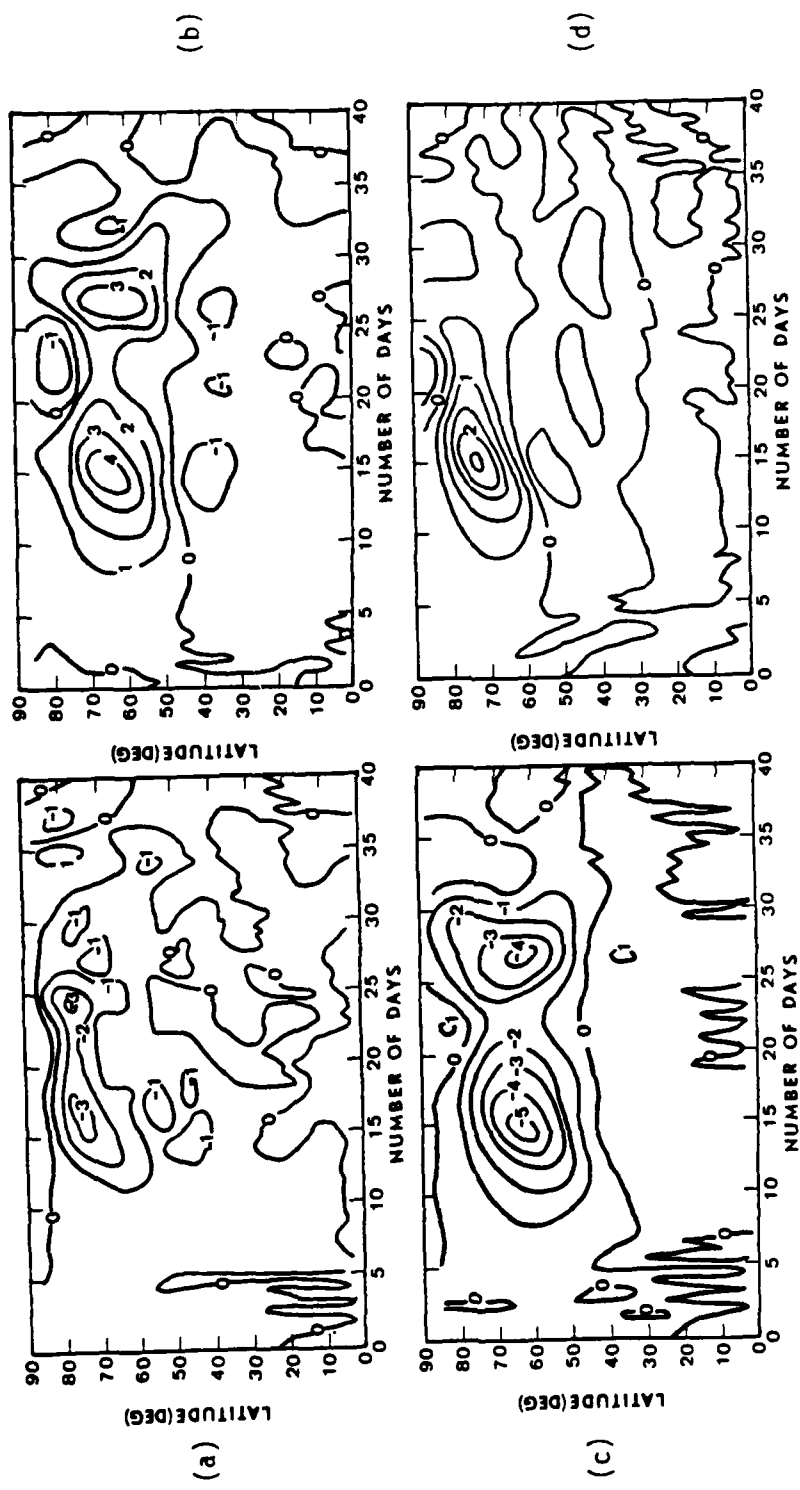
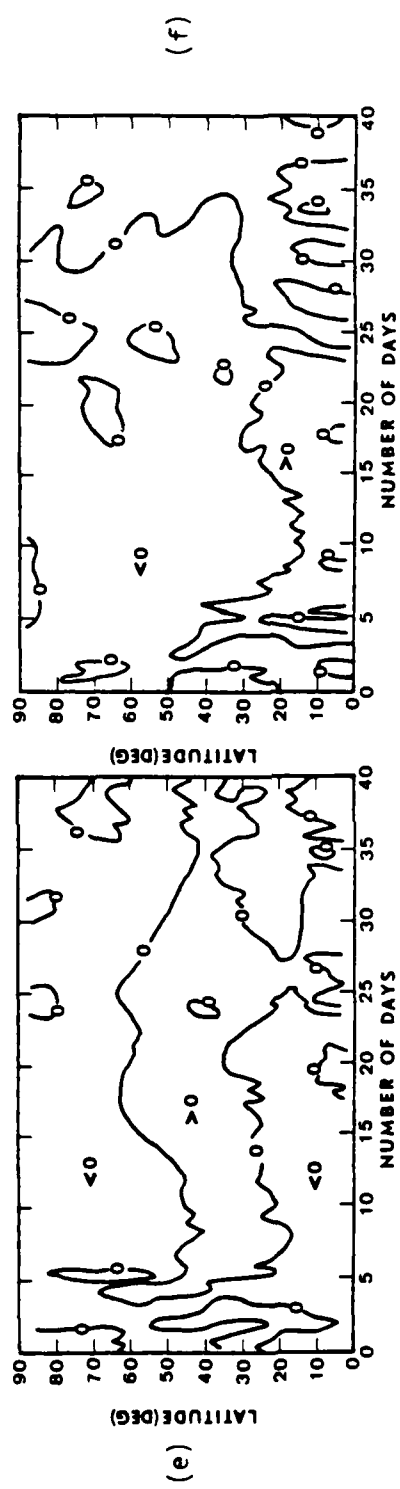


Figure 27. C1 latitude-time sections at 40.5 km of (a) $\bar{a}_u/\partial t$; (b) $\bar{a}_u/\partial t$; (c) $\bar{a}_u/\partial t$; (d) $\bar{a}_u/\partial t$. Units are 10^{-4} m s^{-2} .



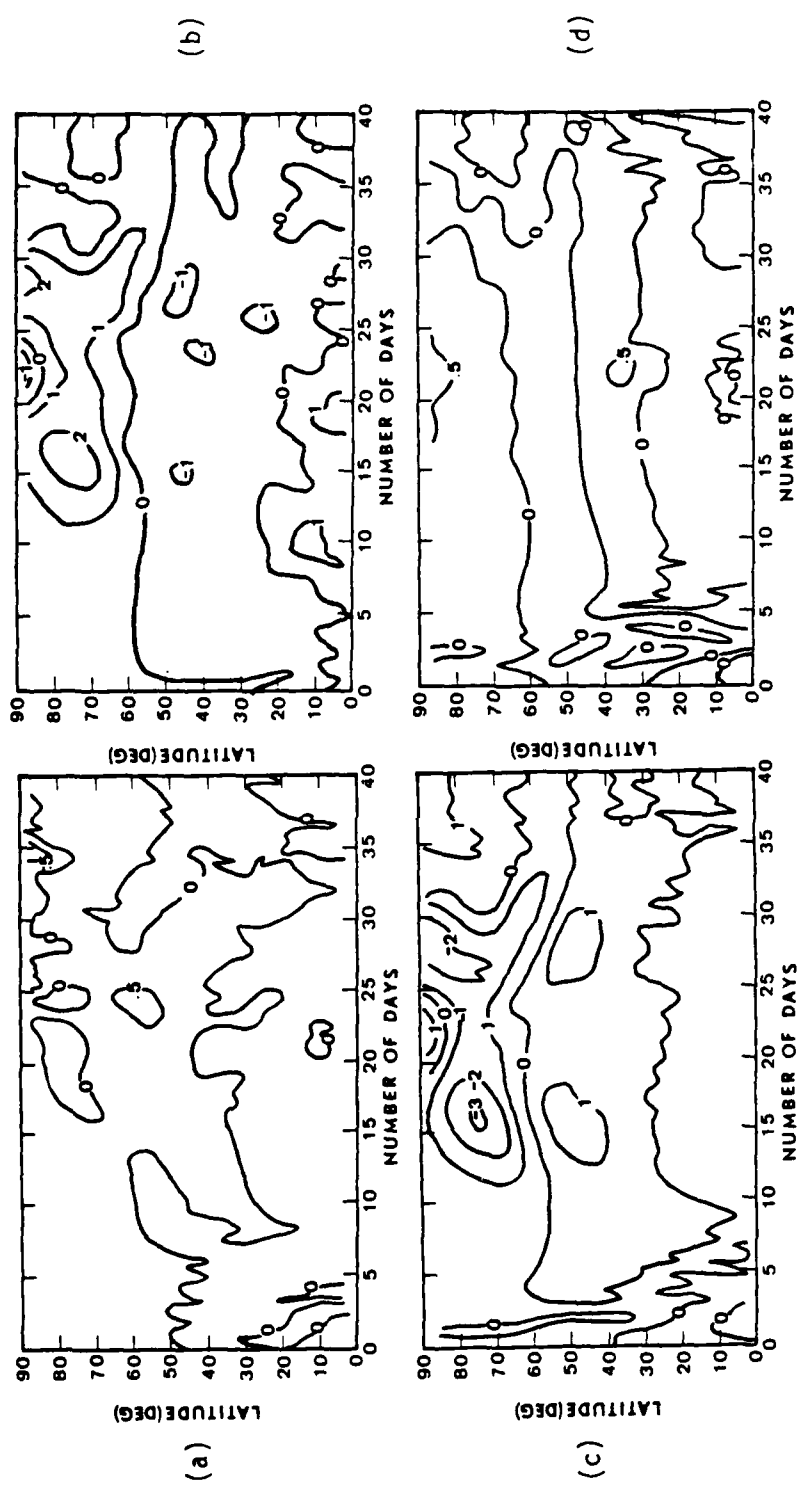


Figure 28. C1 latitude-time section at 40.5 km of (a) $\bar{\partial}T/\partial\text{lat}$; (b) VTP; (c) HWB; and (d) VTB.

Units are $10^{-4} \text{ }^{\circ}\text{K s}^{-1}$.

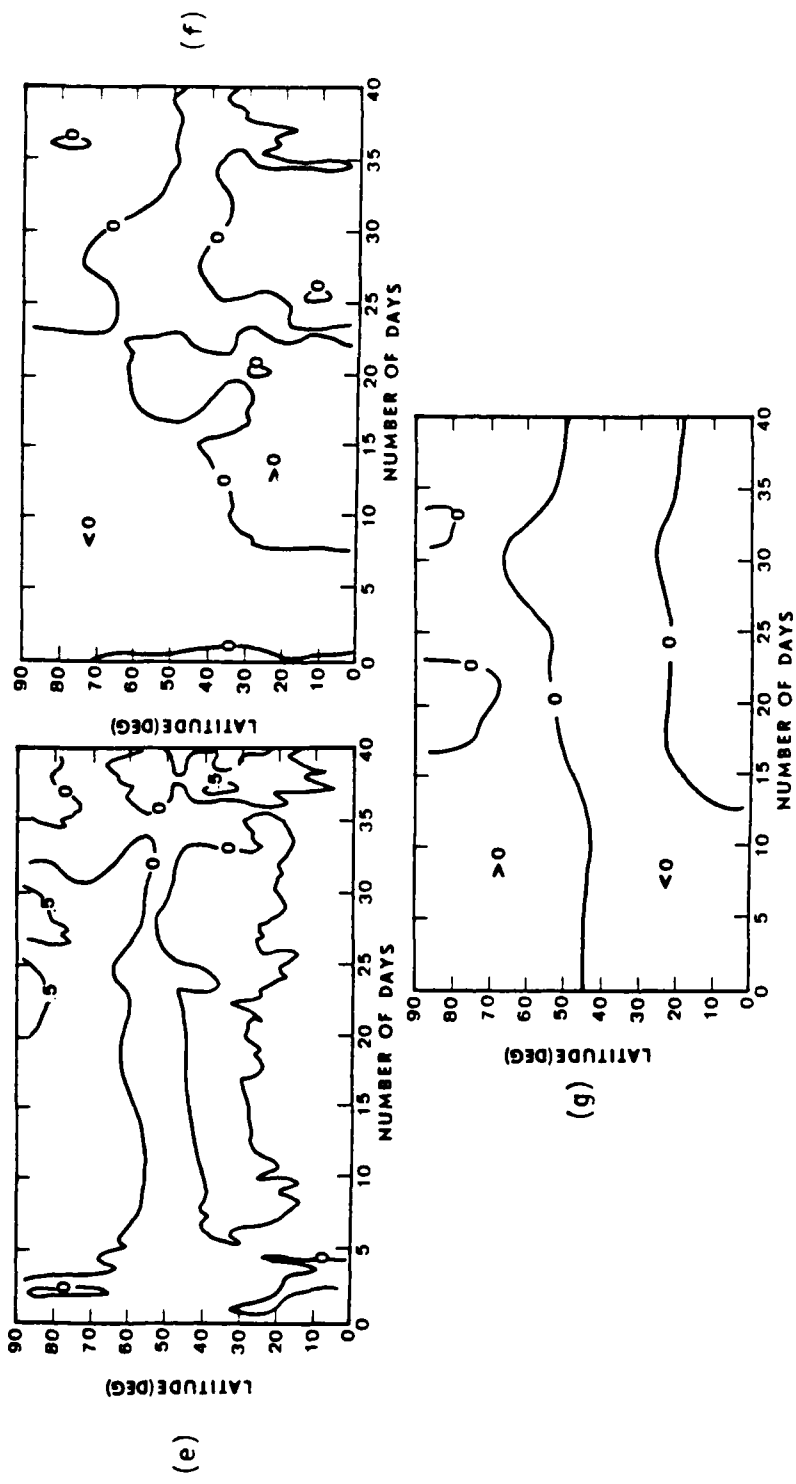


Figure 28 (continued). (e) WTB; (f) WTP; and (g) HNA.

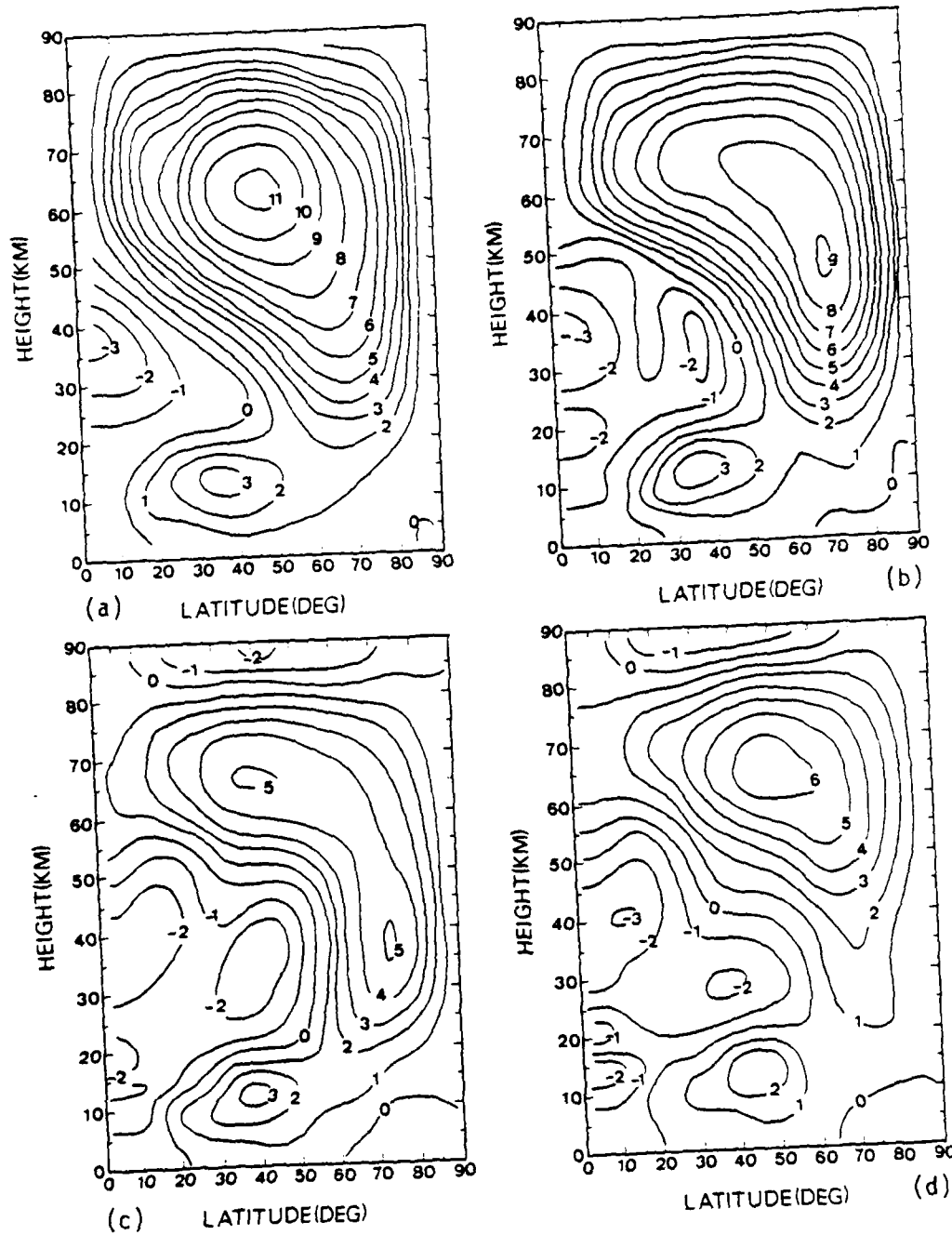


Figure 29. Latitude-height sections of the mean zonal wind ($\times 10 \text{ m s}^{-1}$) for C2 on (a) day 10; (b) day 20; (c) day 30; (d) day 40.

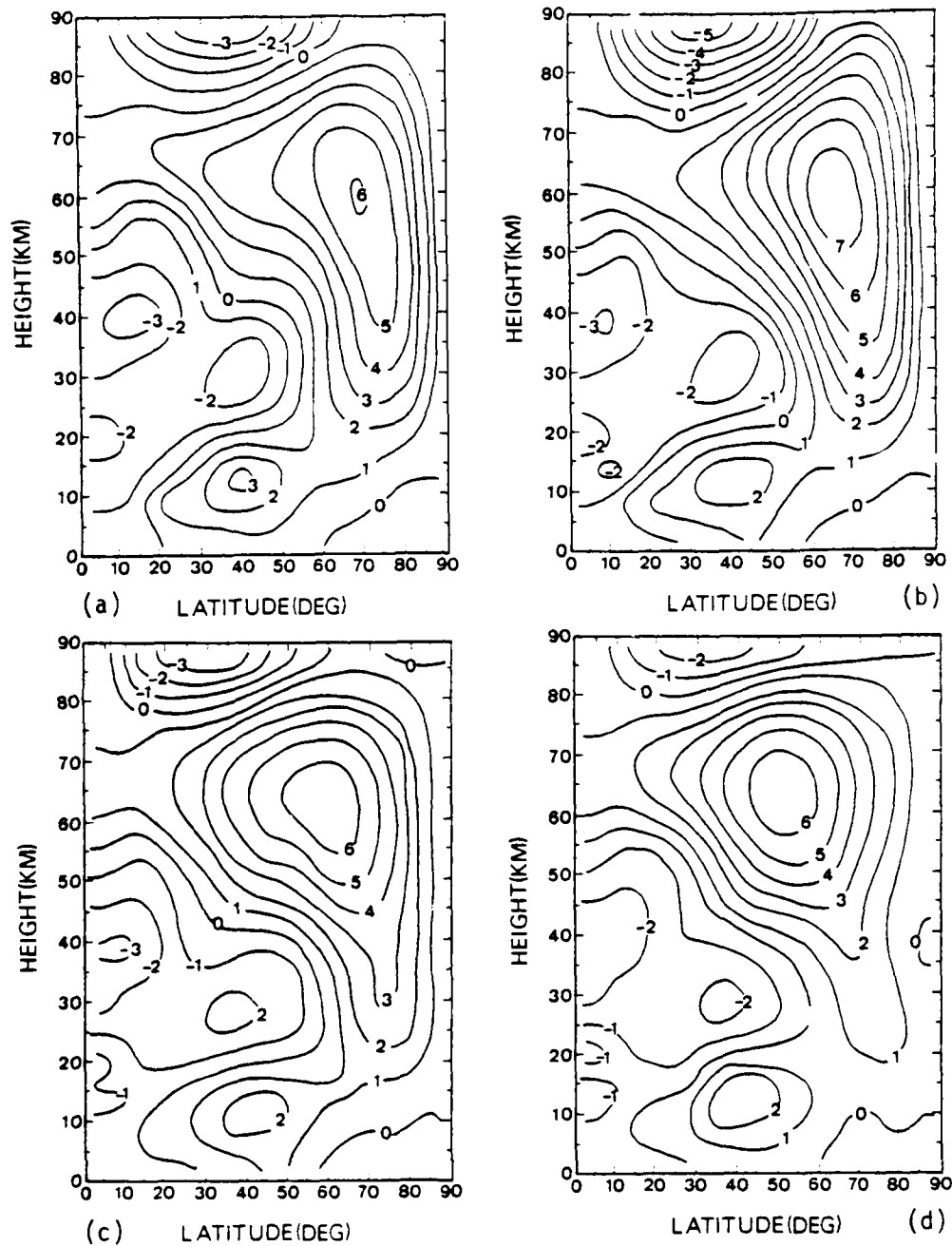


Figure 30. Same as Fig. 29 except on (a) day 32; (b) day 34;
(c) day 36; and (d) day 38.

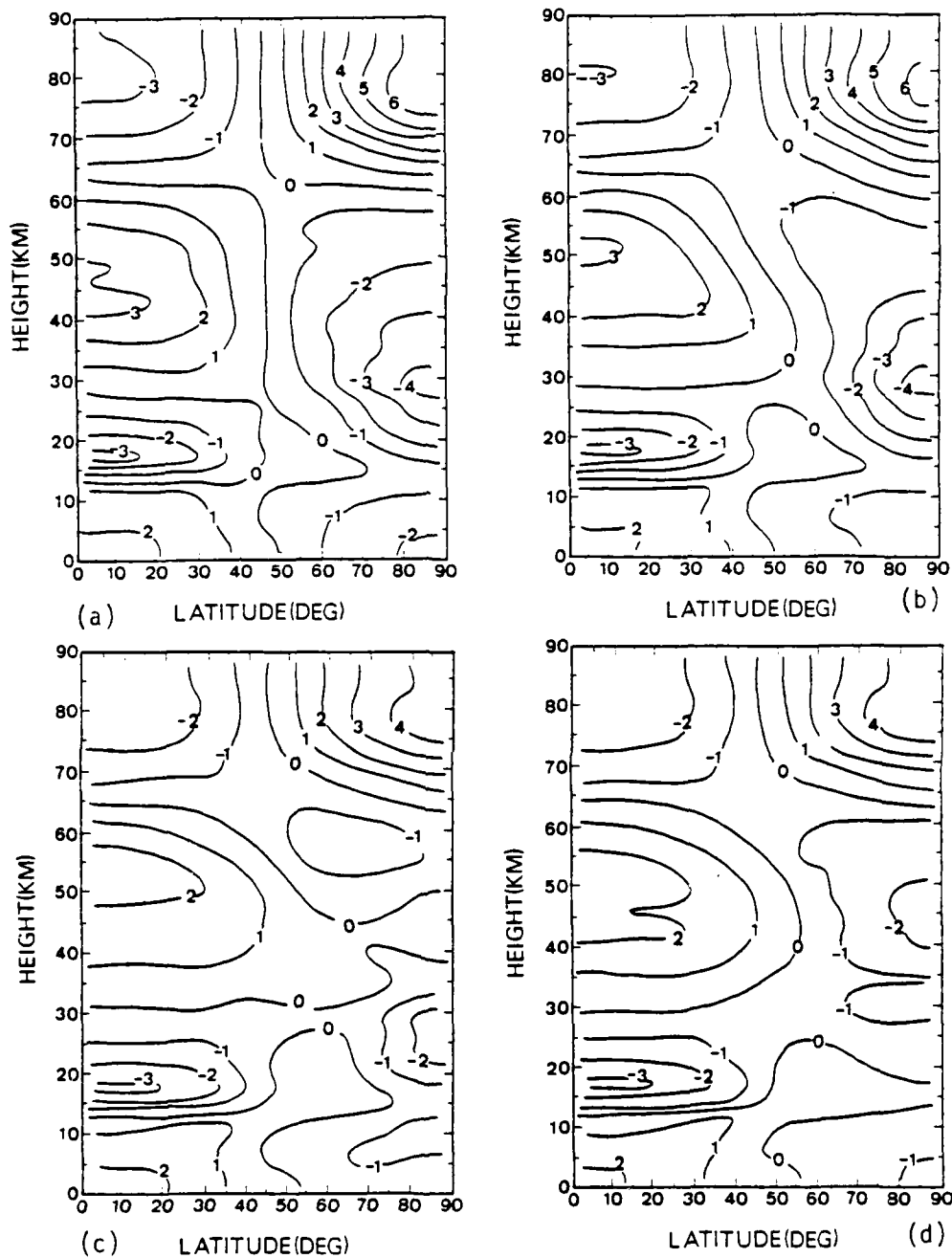


Figure 31. Latitude-height sections of zonal mean temperature deviation ($\times 10^0$ K) for C2 on (a) day 10; (b) day 20; (c) day 30; and (d) day 40.

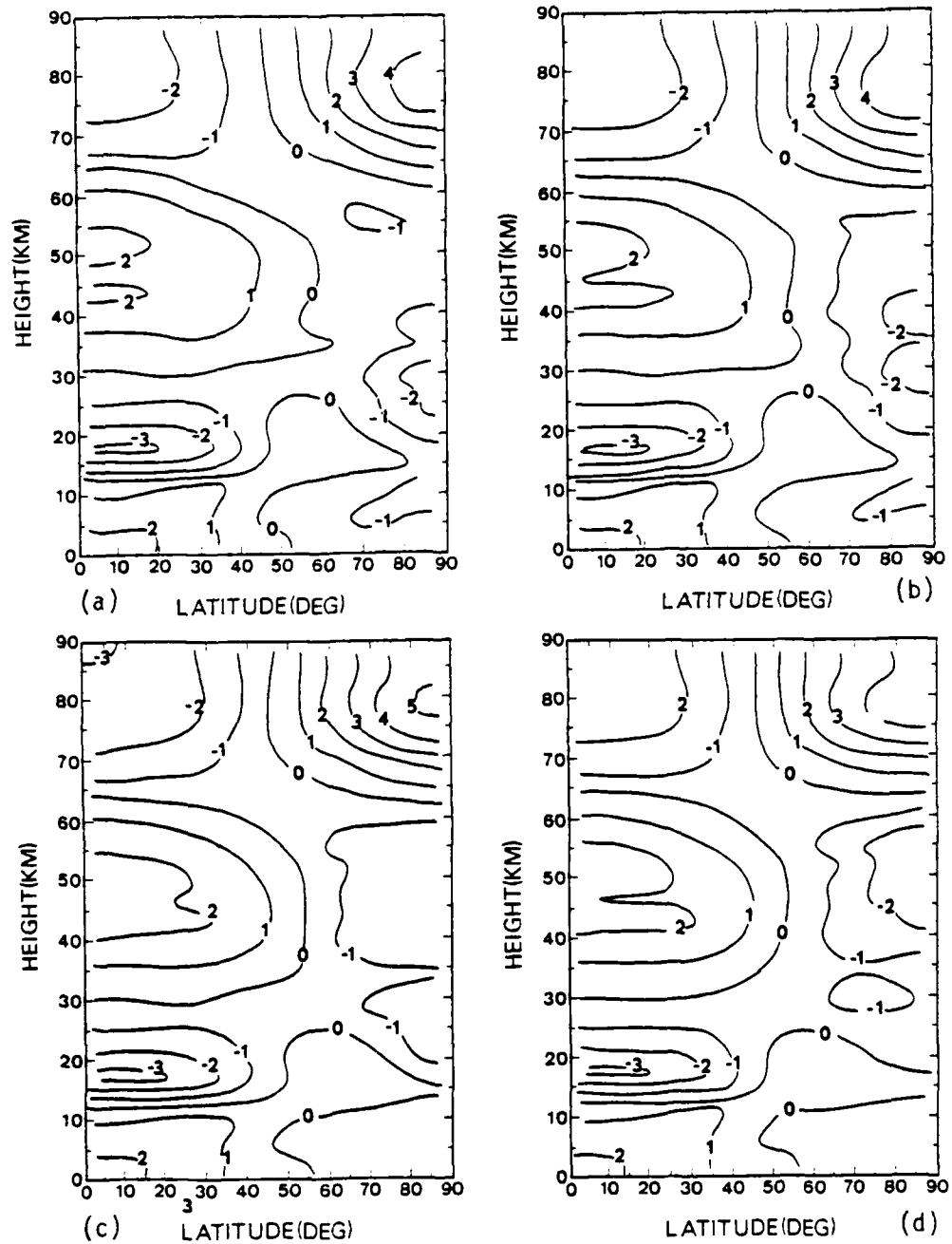


Figure 32. Same as Fig. 31 except on (a) day 32; (b) day 34;
(c) day 36; and (d) day 40.

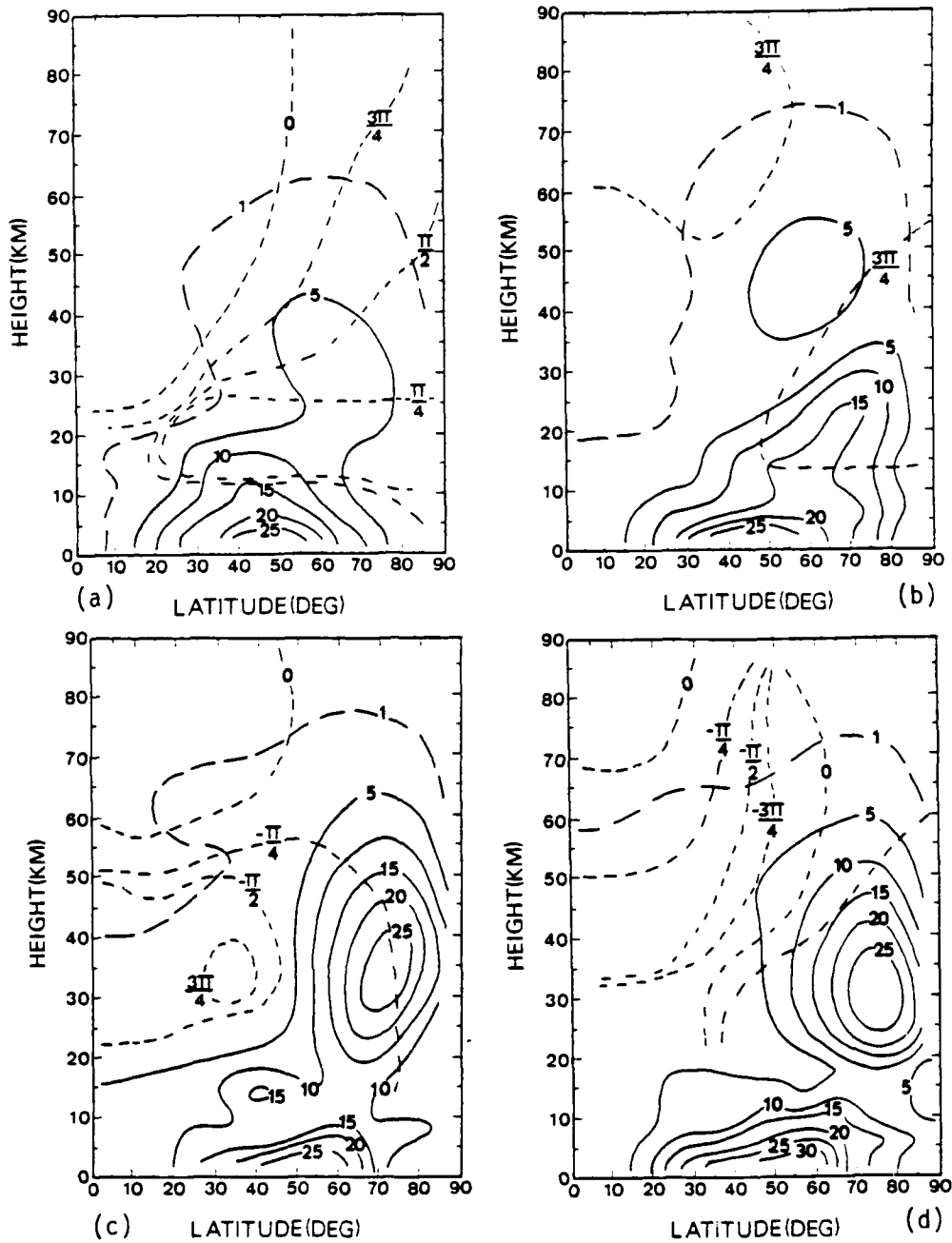


Figure 33. C2 latitude-height sections of $|\Phi_1|$ ($\times 10^2 \text{ m}^2 \text{ s}^{-2}$) indicated by solid lines (except for $|\Phi_1| = 100$ represented by long dashed lines) with the Φ_1 phase angle (radians) indicated by short dashed lines for (a) day 10; (b) day 20; (c) day 30; and (d) day 40.

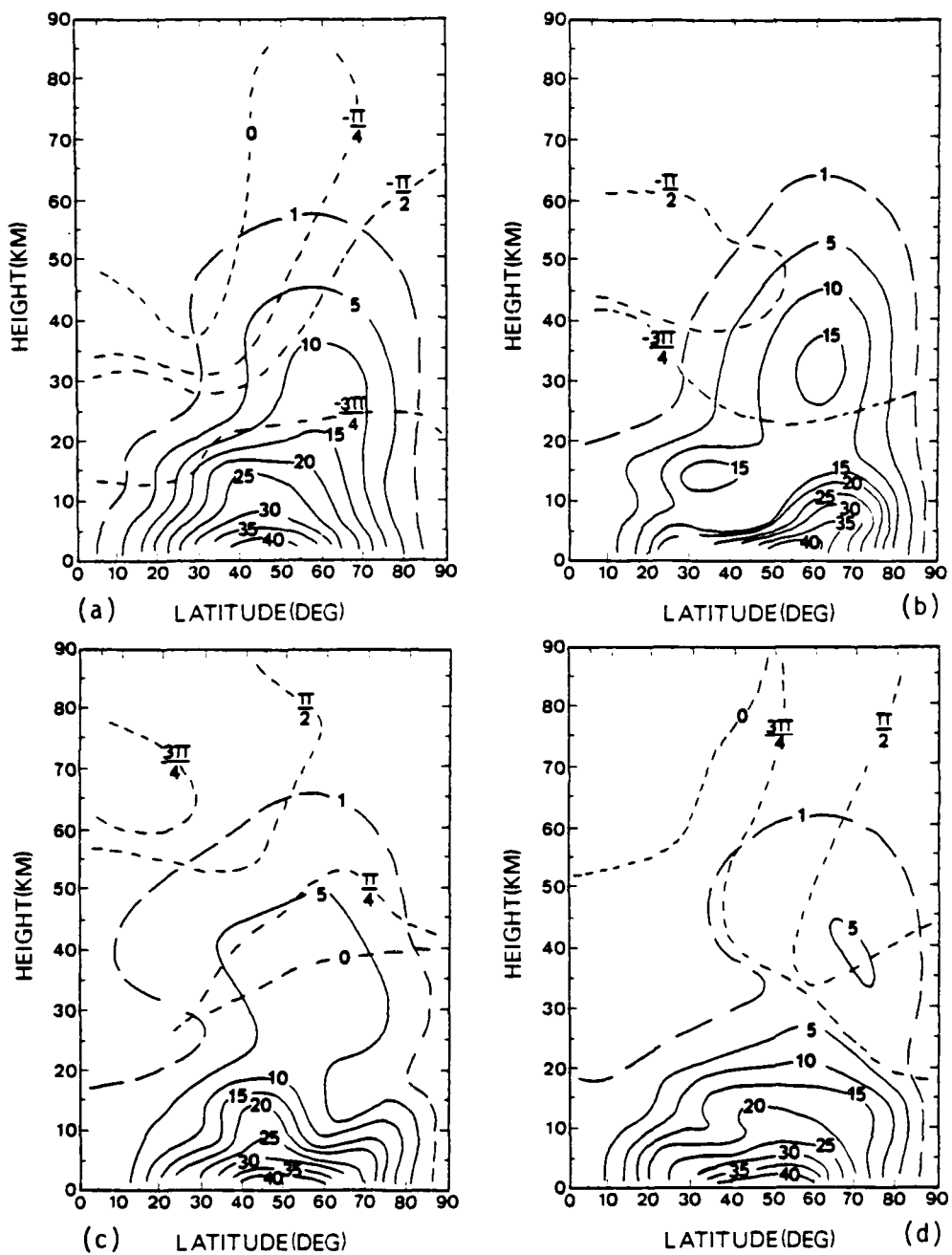


Figure 34. Same as Fig. 33 except for Φ_2 .

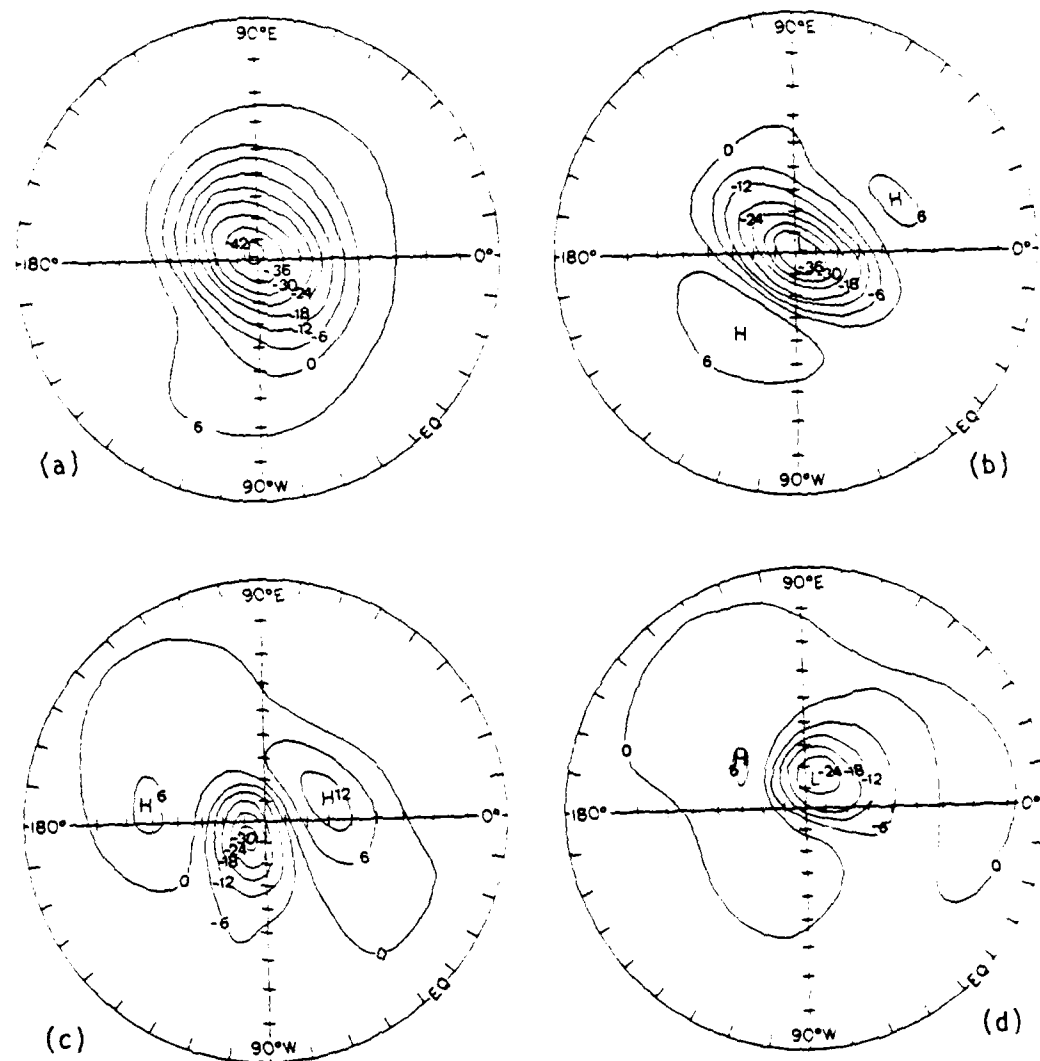


Figure 35. Polar stereographic projections of height deviations ($\times 10^2$ m) at 40.5 km for C2 on (a) day 10; (b) day 20; (c) day 30; and (d) day 40.

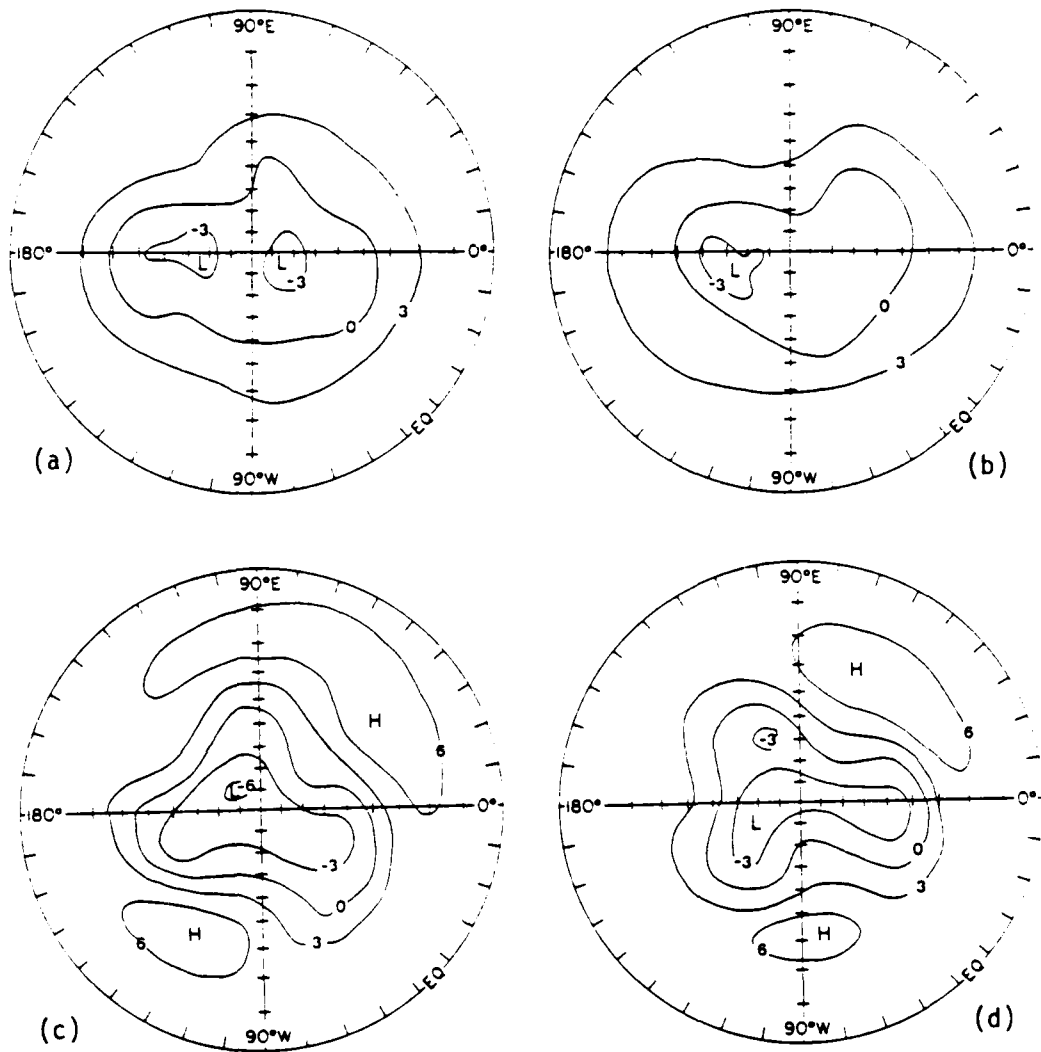


Figure 36. Polar stereographic projections of height deviations ($\times 10^2$ m) for C2 at approximately 6.7 km on (a) day 30 and (b) day 40; and at 13.5 km on (c) day 34 and (d) day 38.

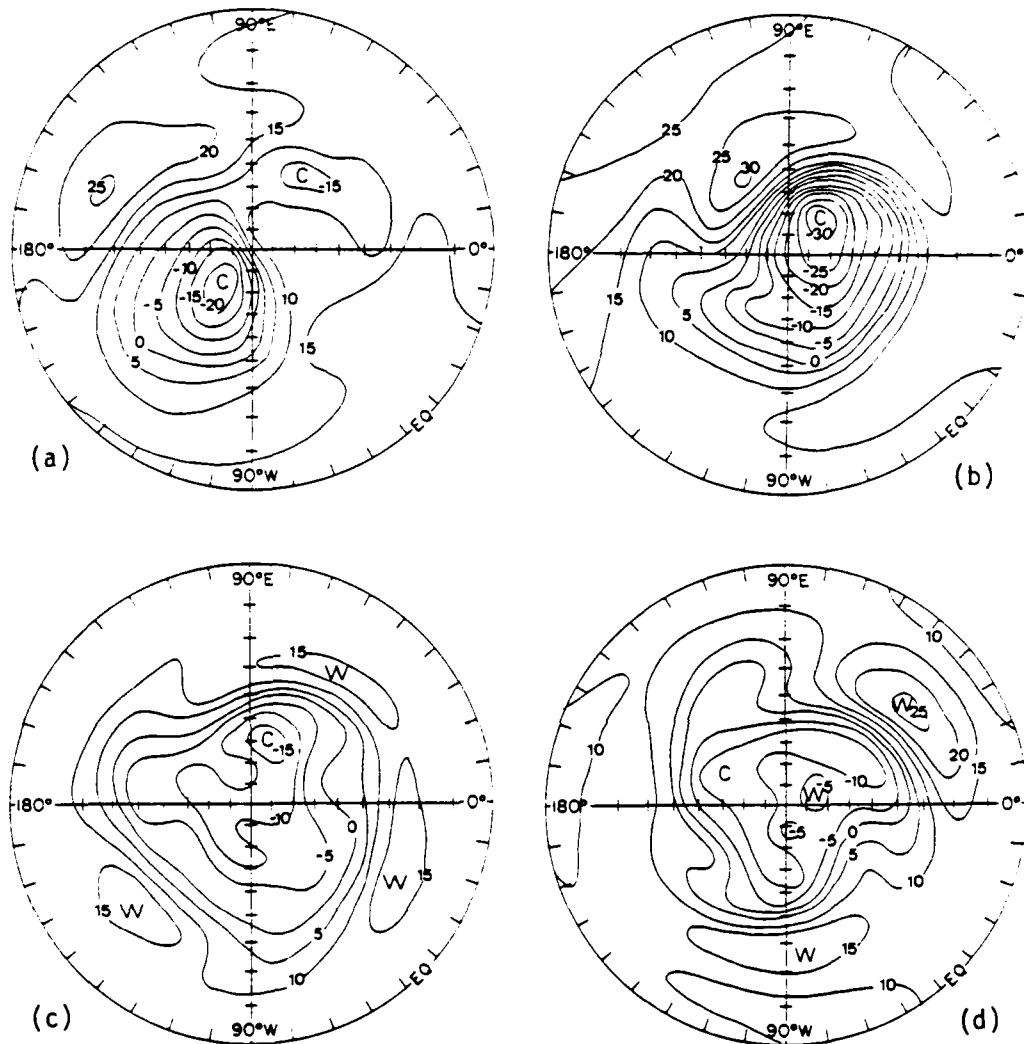


Figure 37. Polar stereographic projections of temperature deviations ($^{\circ}\text{K}$) at 40.5 km on (a) day 30 and (b) day 40; and at approximately 6.7 km on (c) day 30 and (d) day 40.

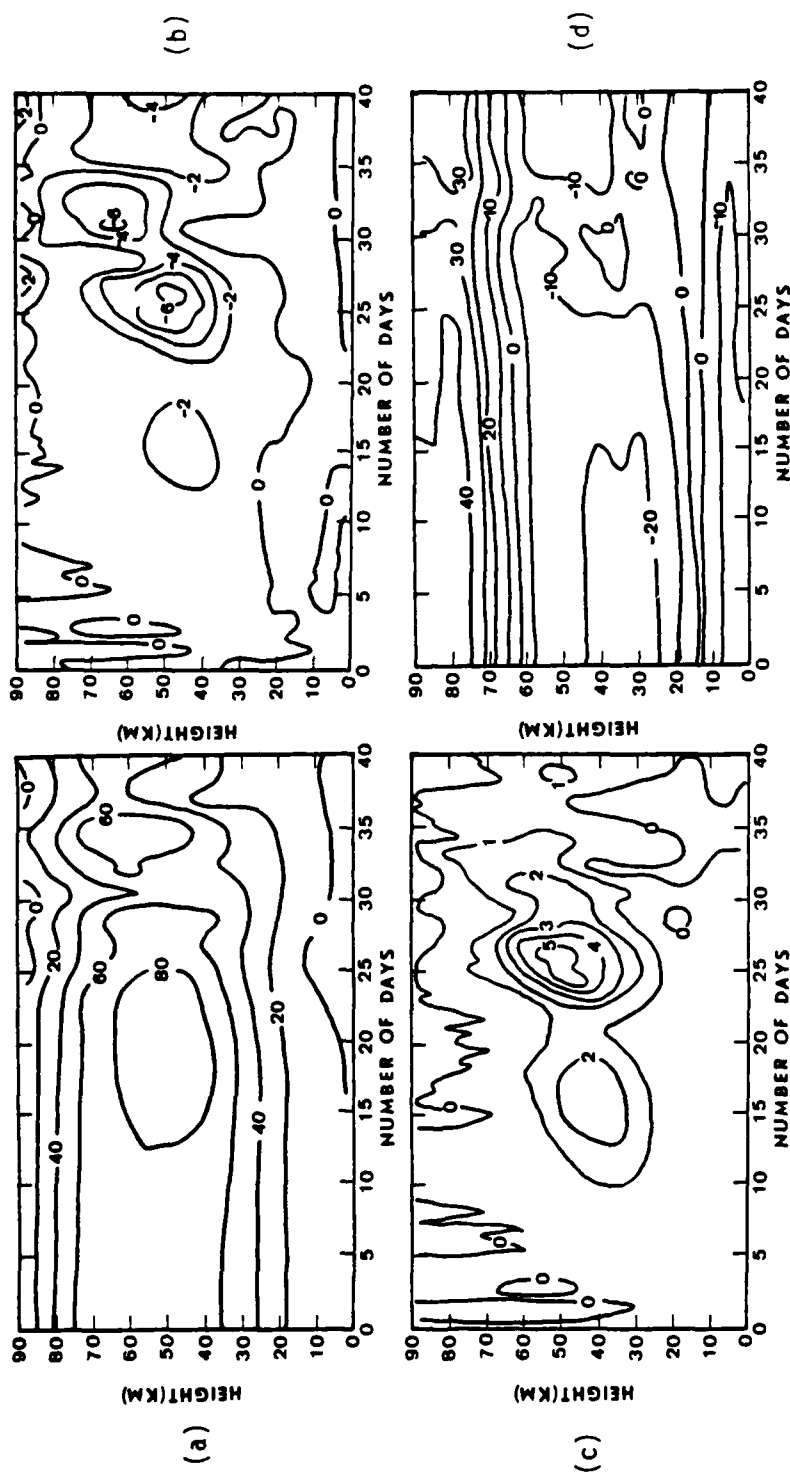


Figure 38. C2 height-time sections at 68.9 N of (a) mean zonal wind (m s^{-1}); (b) zonal mean meridional velocity component (m s^{-1}); (c) zonal mean vertical velocity ($\times 10^{-1} \text{ m s}^{-1}$); and (d) zonal mean temperature deviation ($^{\circ}\text{K}$).

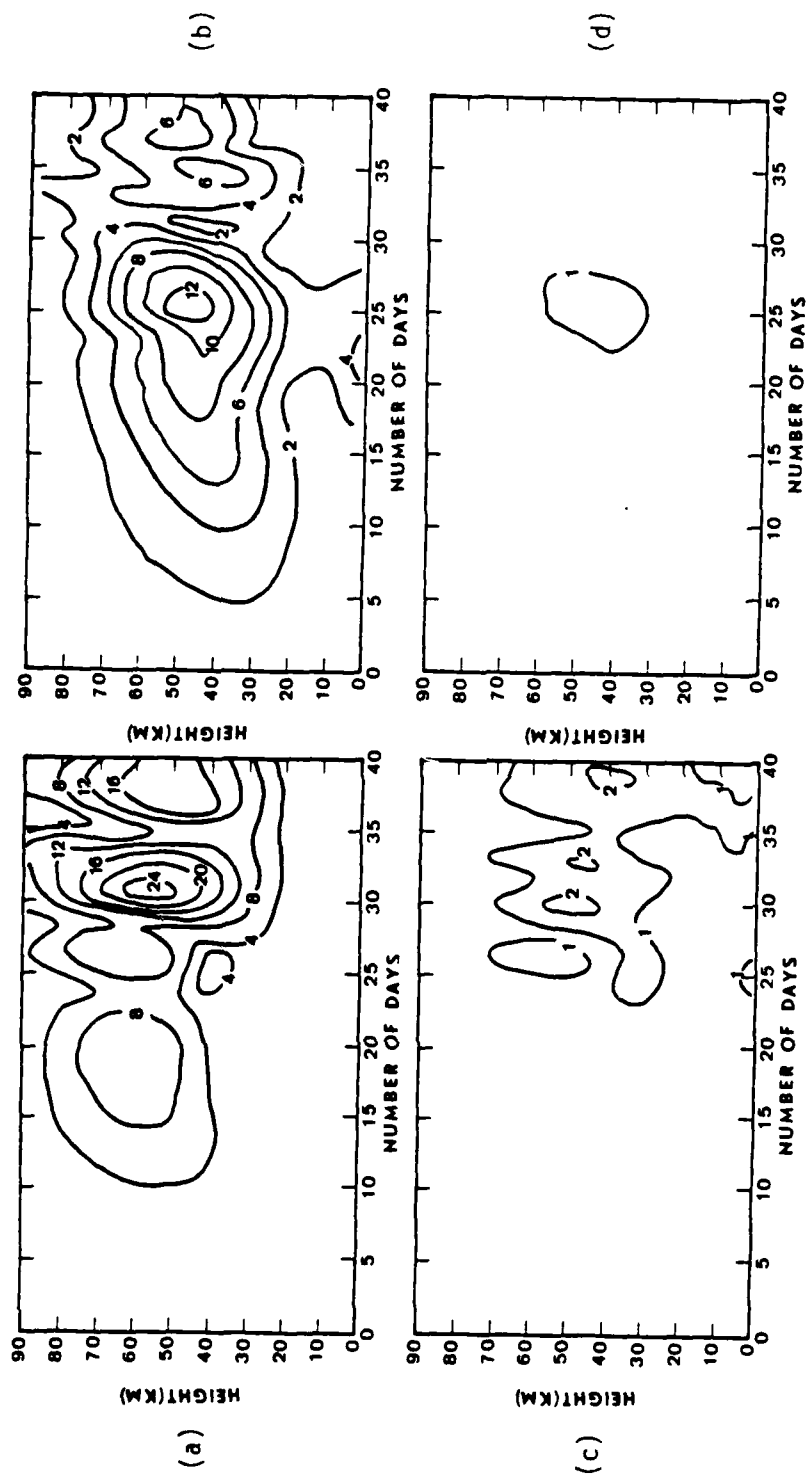


Figure 39. C2 height-time sections at 68.9 N of (a) $|\Phi_1|$; (b) $|\Phi_2|$; (c) $|\Phi_3|$; and (d) $|\Phi_4|$. Units are $10^3 \text{ m}^2 \text{ s}^{-2}$.

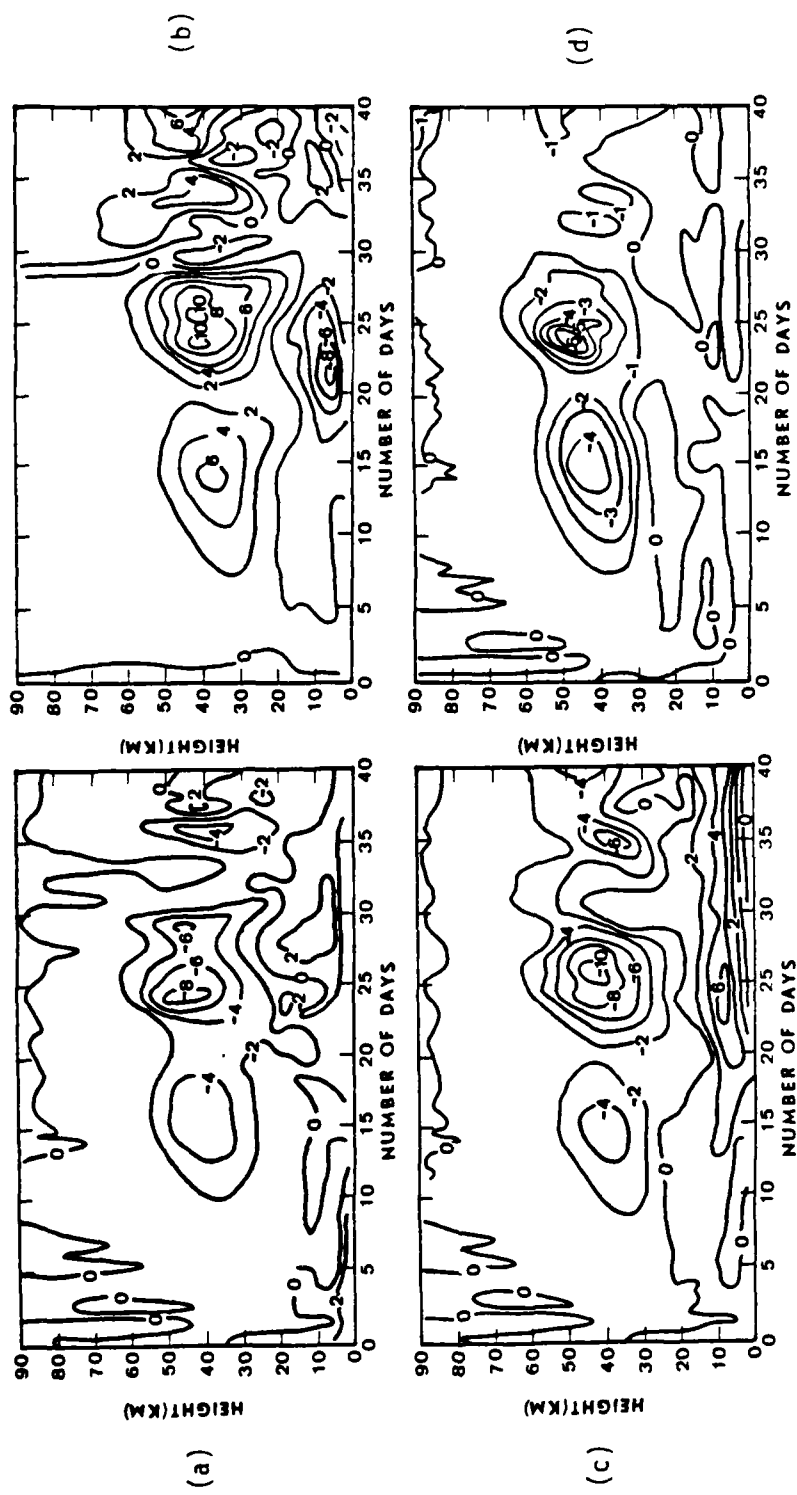


Figure 40. C2 height-time sections at 68.9 N of (a) $\partial\bar{U}/\partial t$; (b) \bar{U} ; (c) \bar{V} ; (d) \bar{V} . Units are 10^{-4} m s^{-2} .

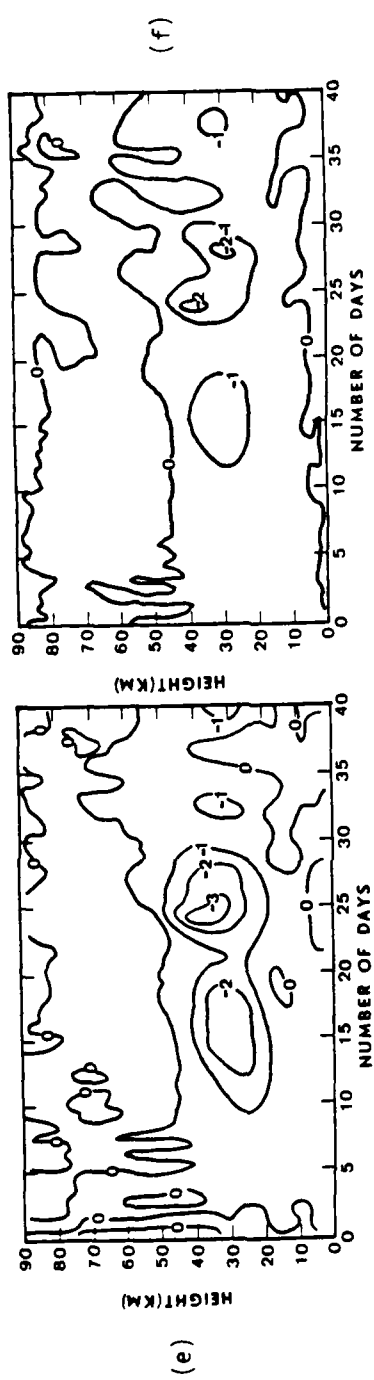


Figure 40 (continued). (e) FA; and (f) FE.

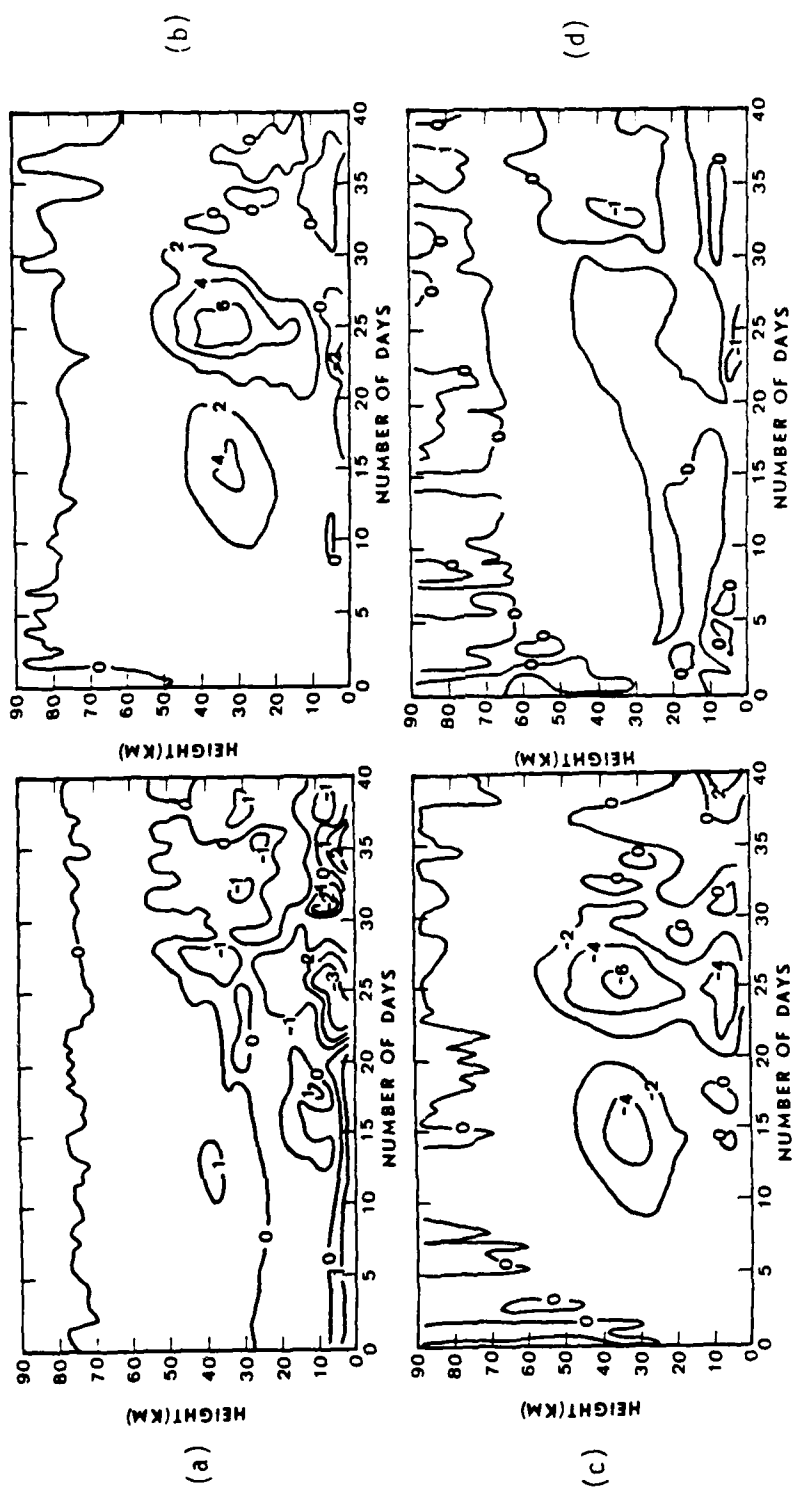


Figure 41. C2 height-time sections at 68.9°N of (a) $\partial\bar{T}/\partial t$; (b) VTP; (c) HMB; (d) VTB.

Units are $10^{-4} \text{ }^{\circ}\text{K s}^{-1}$.

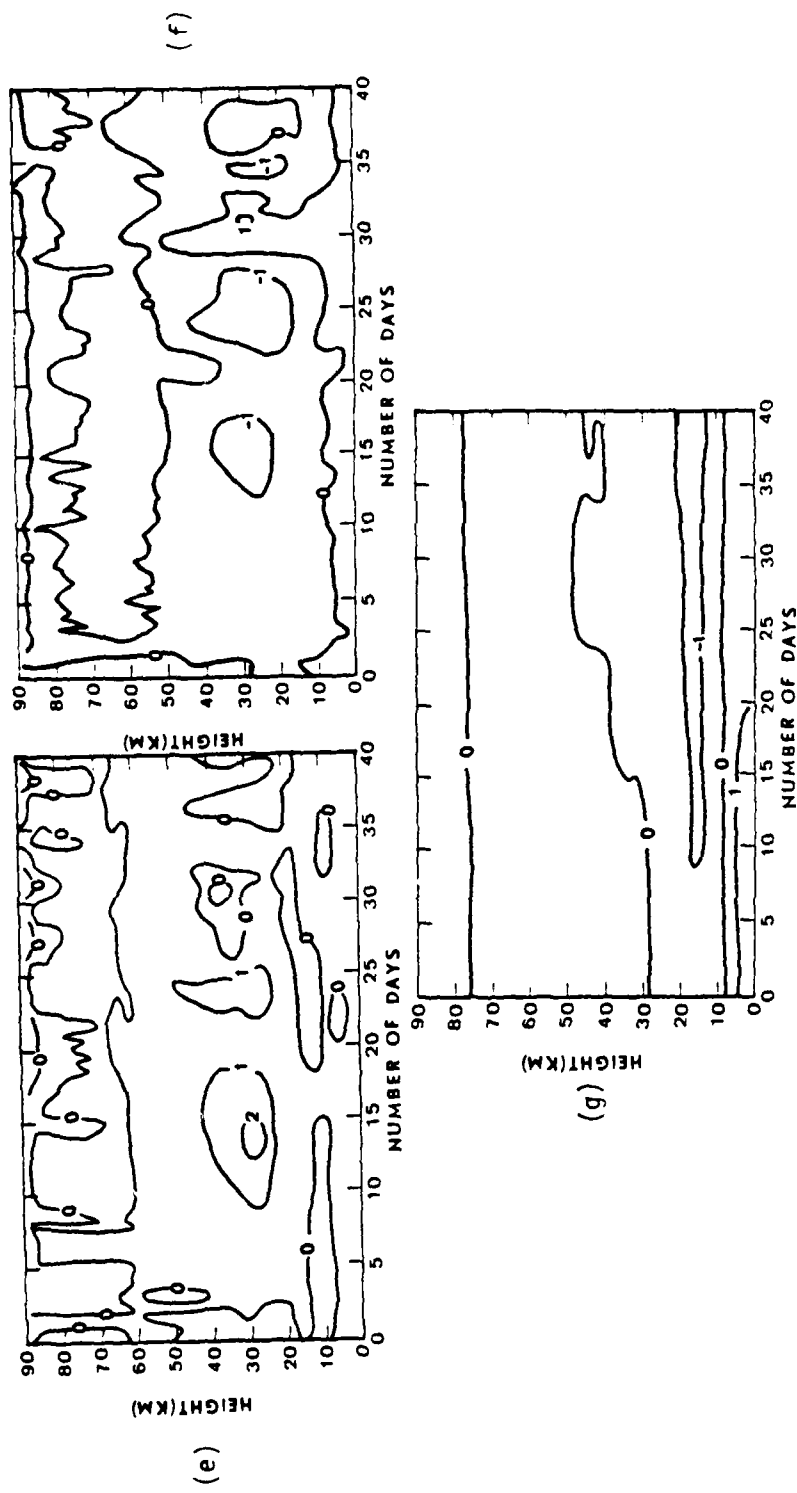


Figure 41 (continued). (e) WTB; (f) WTP; and (g) HNA.

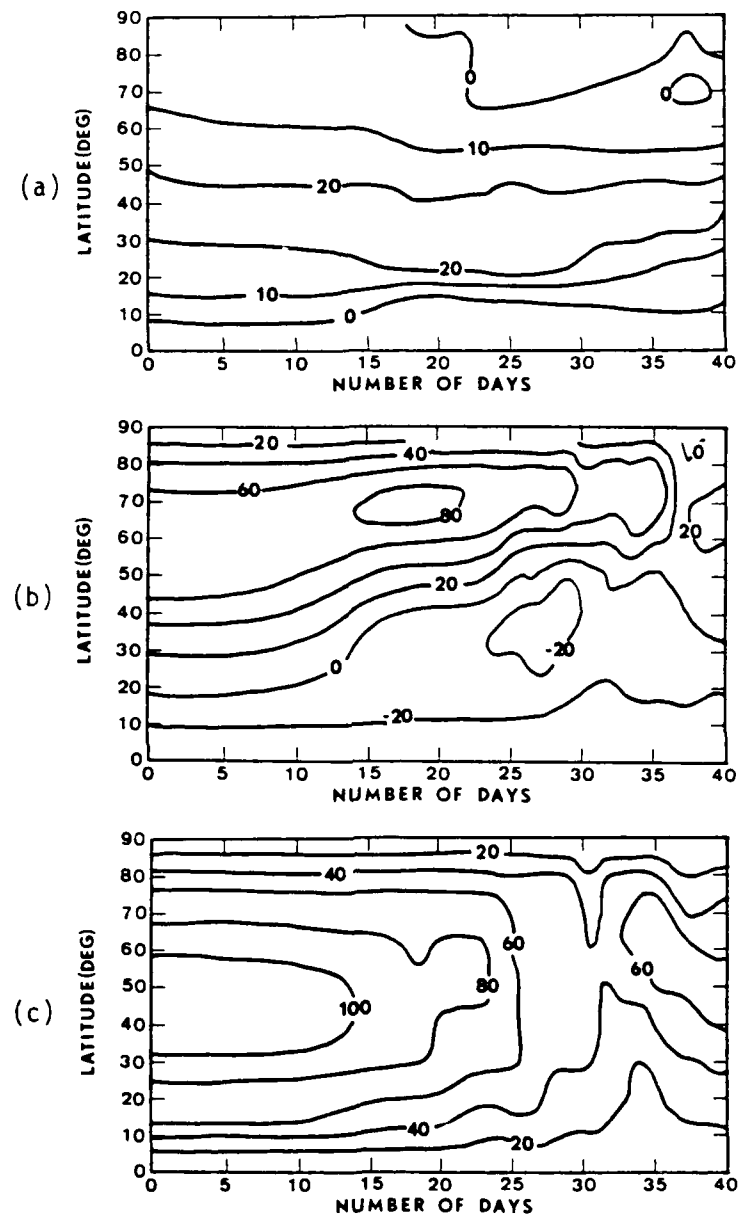


Figure 42. C2 latitude-time section of mean zonal wind (m s^{-1}) at (a) 7.5 km; (b) 40.5 km; and (c) 67.5 km.

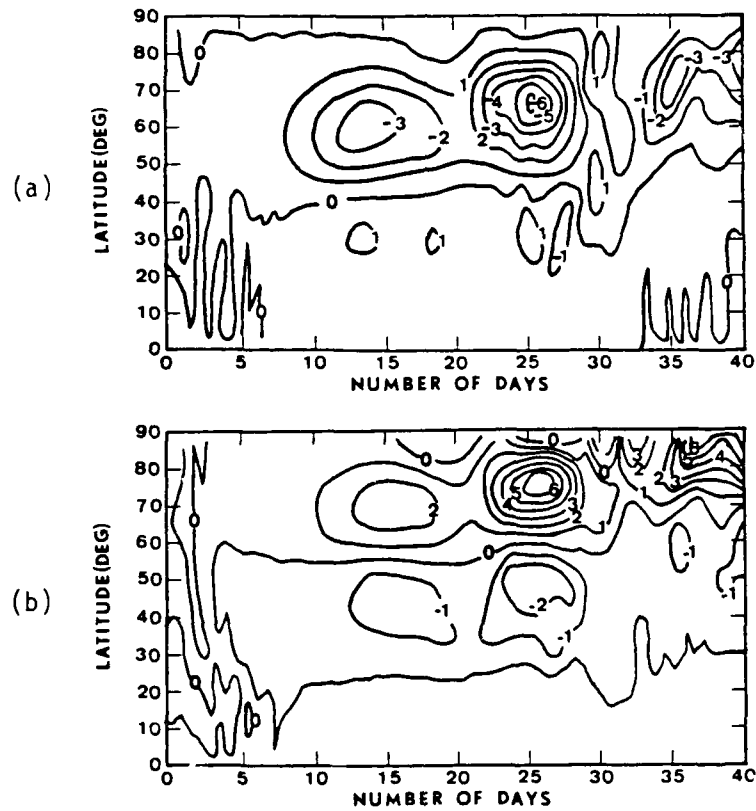


Figure 43. C2 latitude-time sections at 40.5 km of (a) the zonal mean meridional velocity component (m s^{-1}) and (b) the zonal mean vertical velocity ($\times 10^{-1} \text{ m s}^{-1}$).

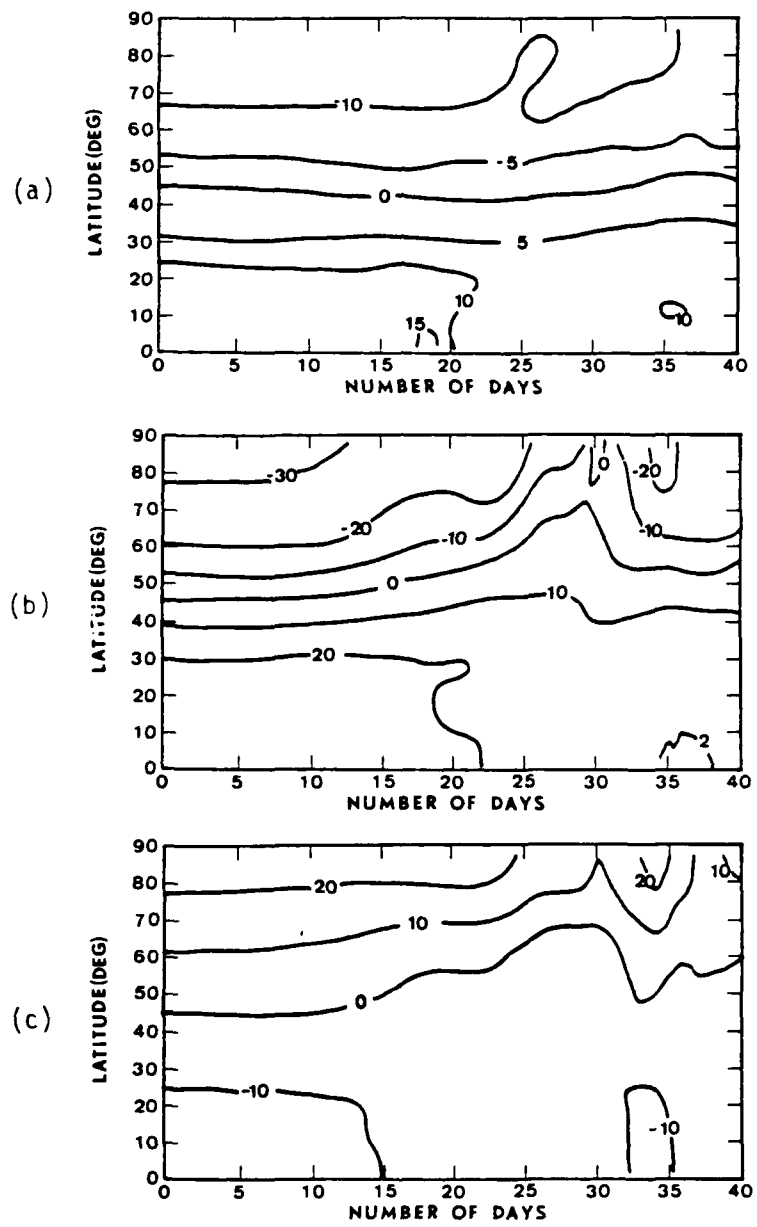


Figure 44. C2 latitude-time sections of zonal mean temperature deviation ($^{\circ}\text{K}$) at (a) 7.5 km; (b) 40.5 km; and (c) 67.5 km.

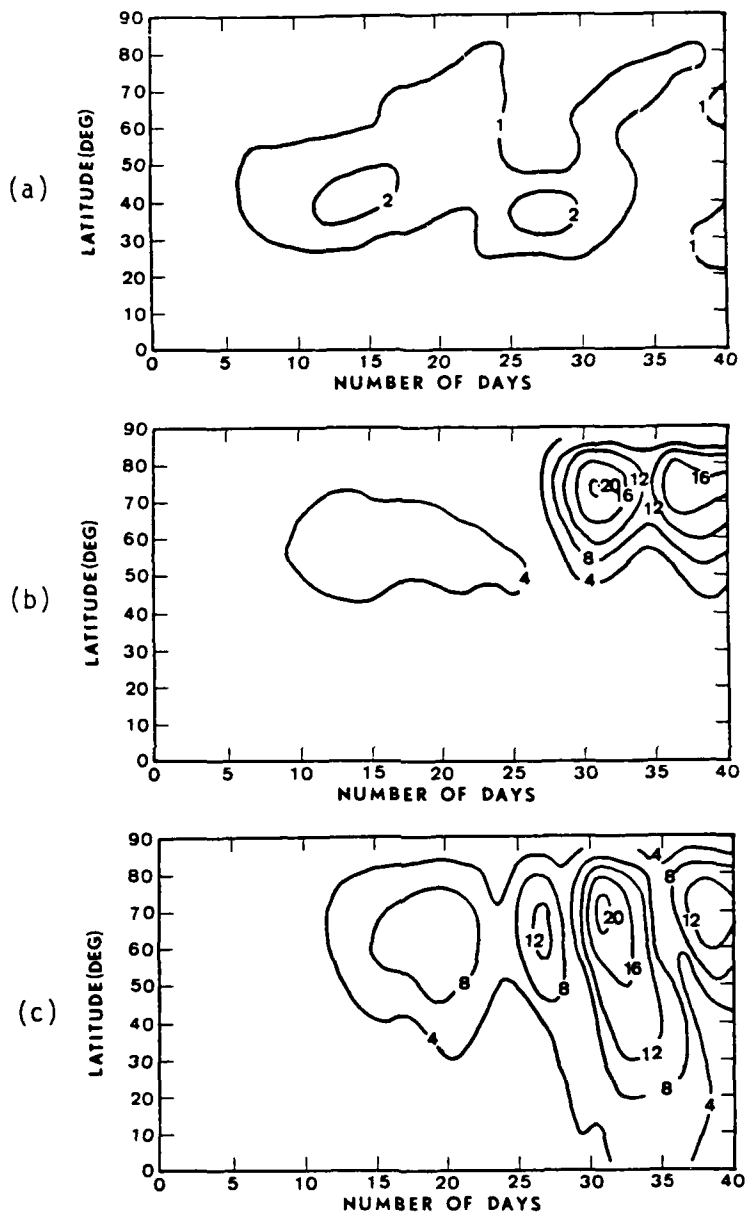


Figure 45. C2 latitude-time sections of $|\Phi_1|$ ($\times 10^3 \text{ m}^2 \text{ s}^{-2}$) at
 (a) 7.5 km; (b) 40.5 km; and (c) 67.5 km.

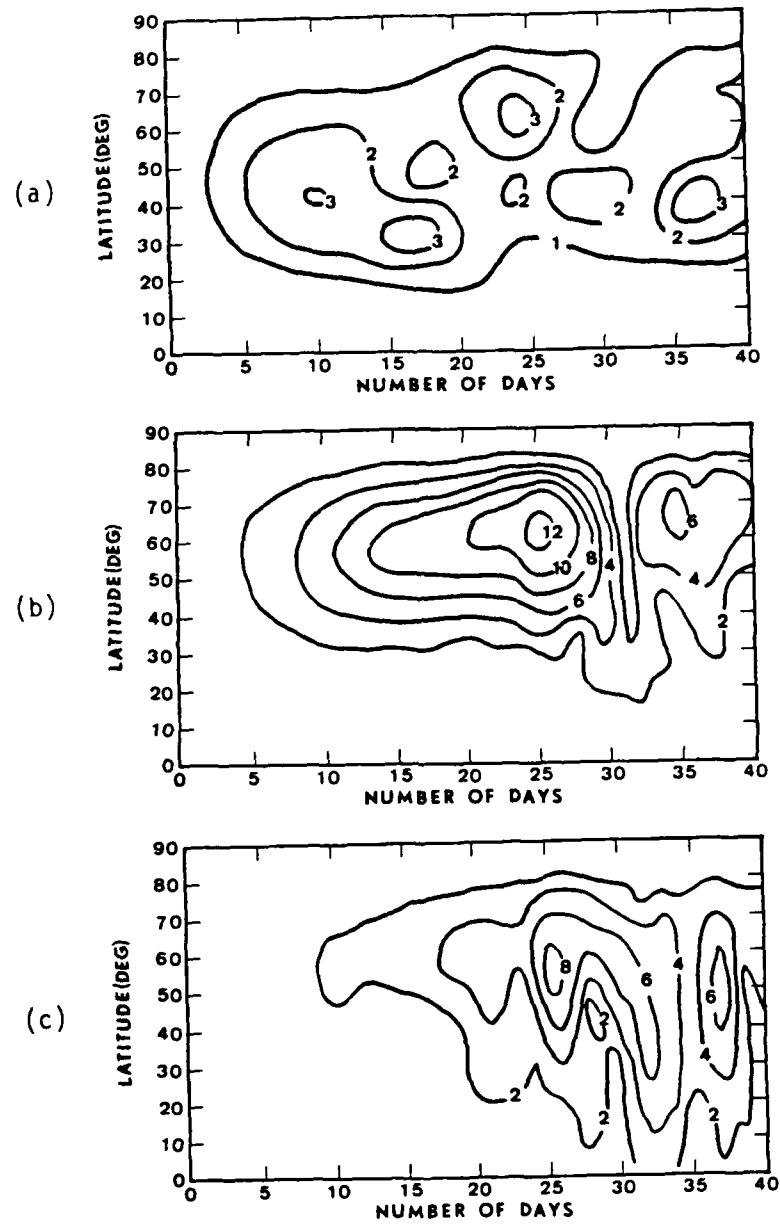


Figure 46. Same as Fig. 45 except for $|\Phi_2|$.

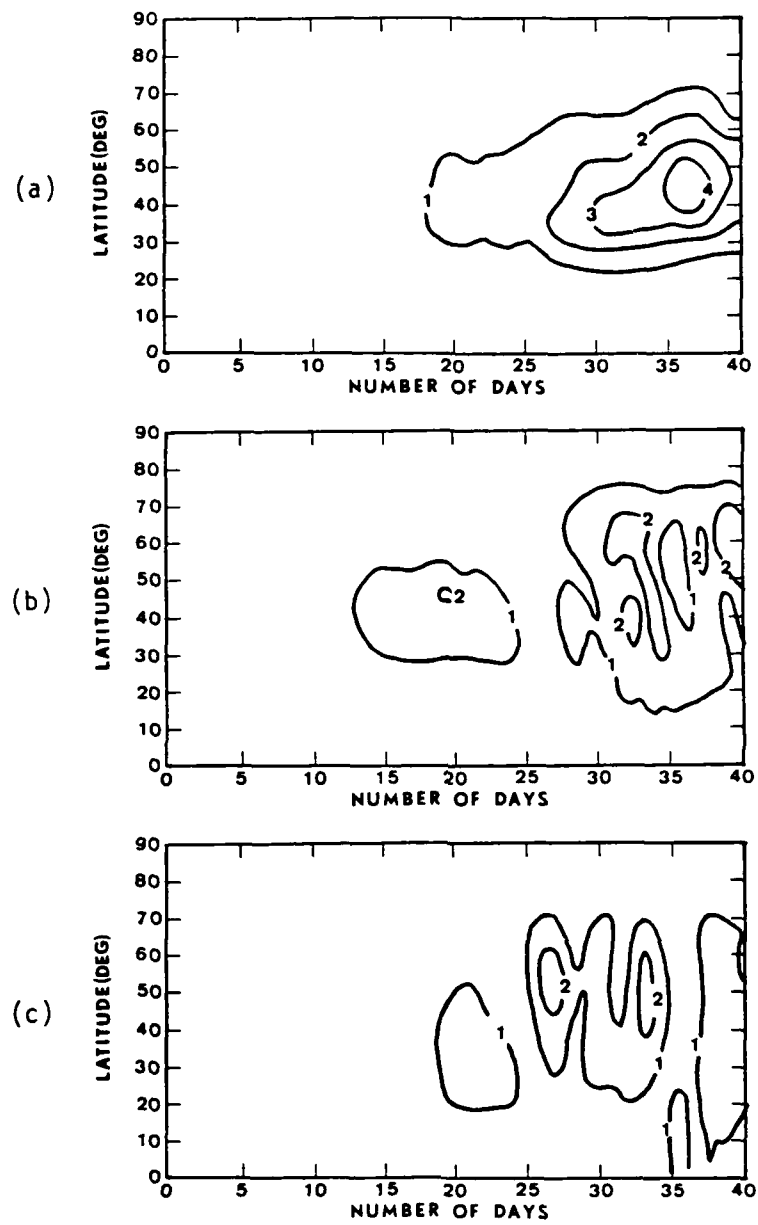


Figure 47. Same as Fig. 45 except for $|\Phi_3|$.

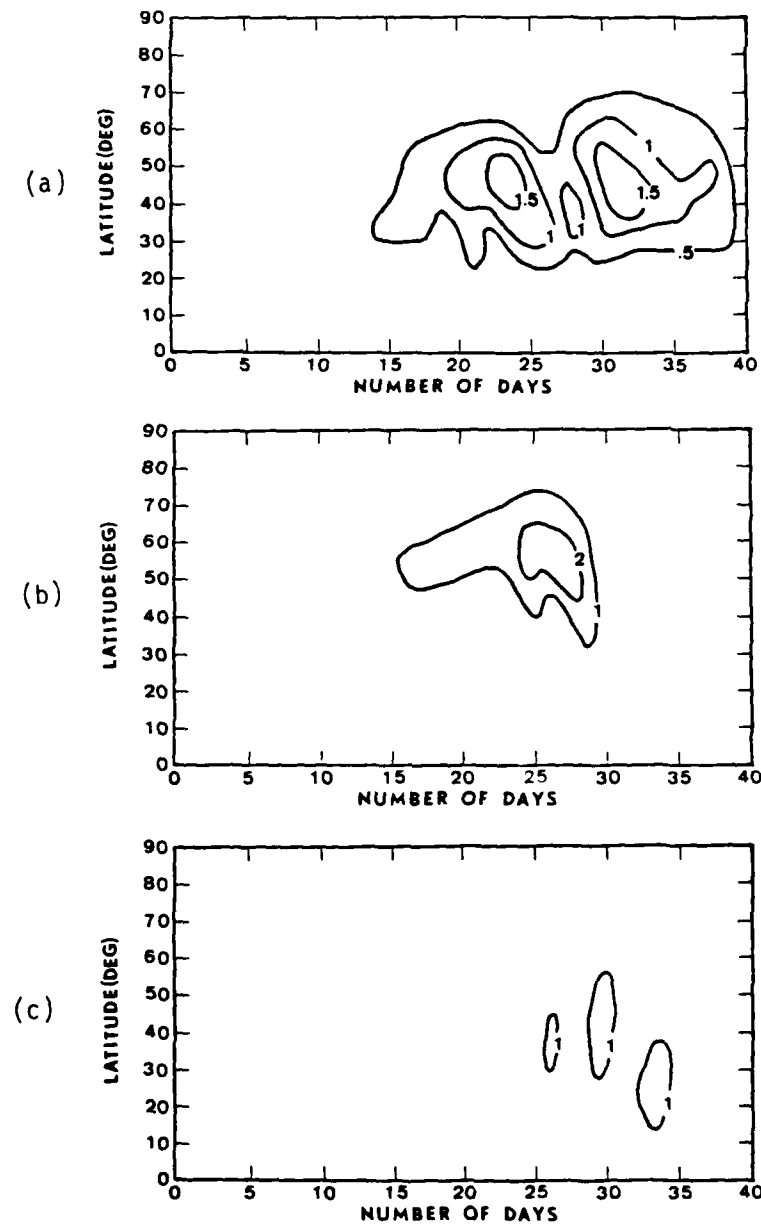


Figure 48. Same as Fig. 45 except for $|\psi_4|$.

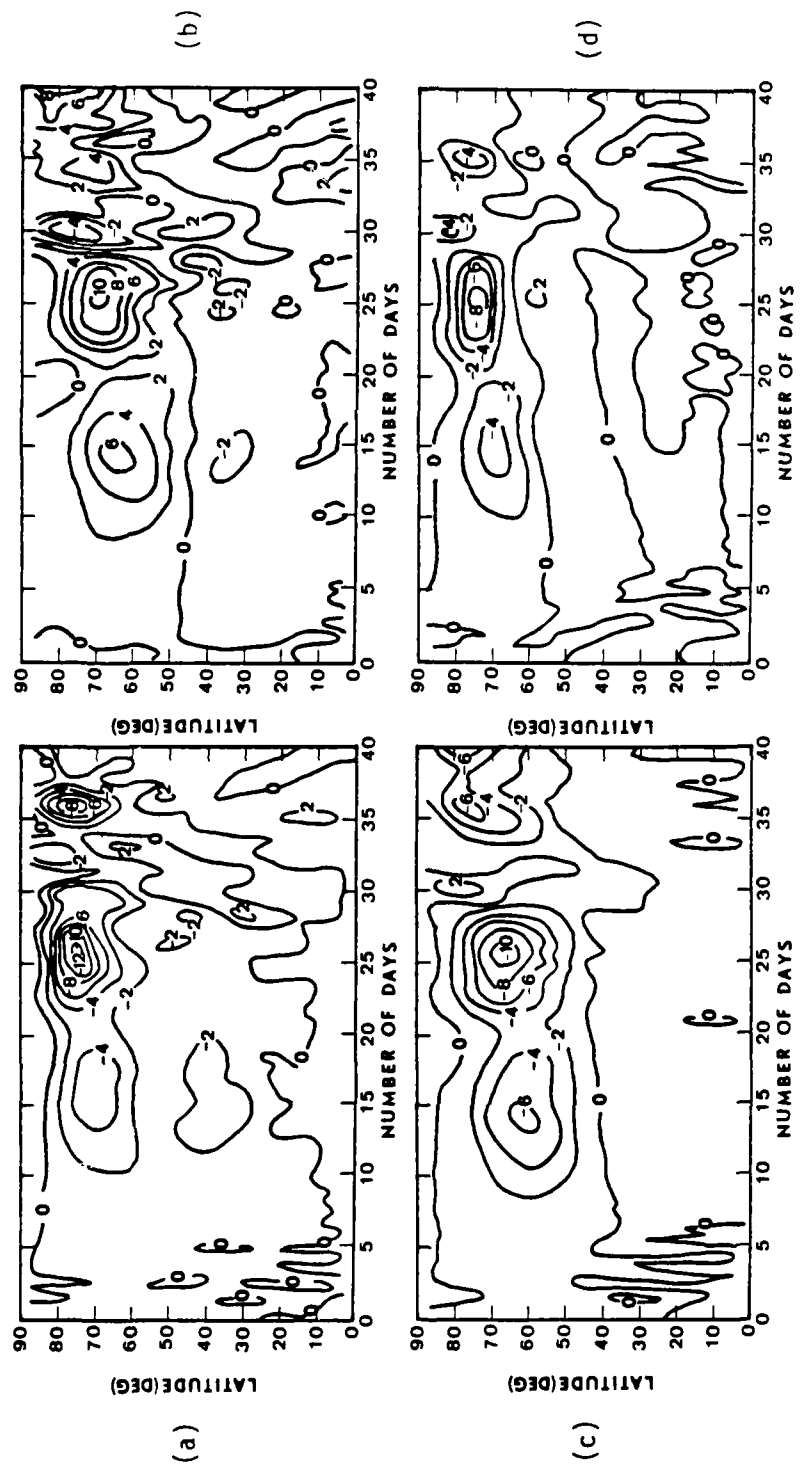


Figure 49. C2 latitude-time sections at 40.5 km of (a) $\partial \bar{u} / \partial t$; (b) FM; (c) FC; (d) FB (d) FB.
Units are 10^{-4} m s $^{-2}$.

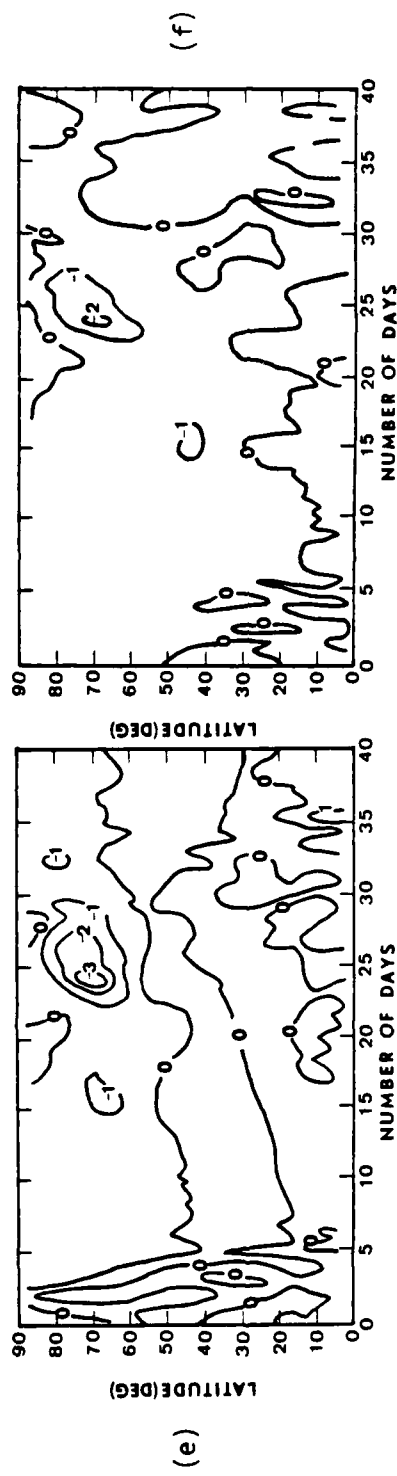


Figure 49 (continued). (e) FA; and (f) FE.

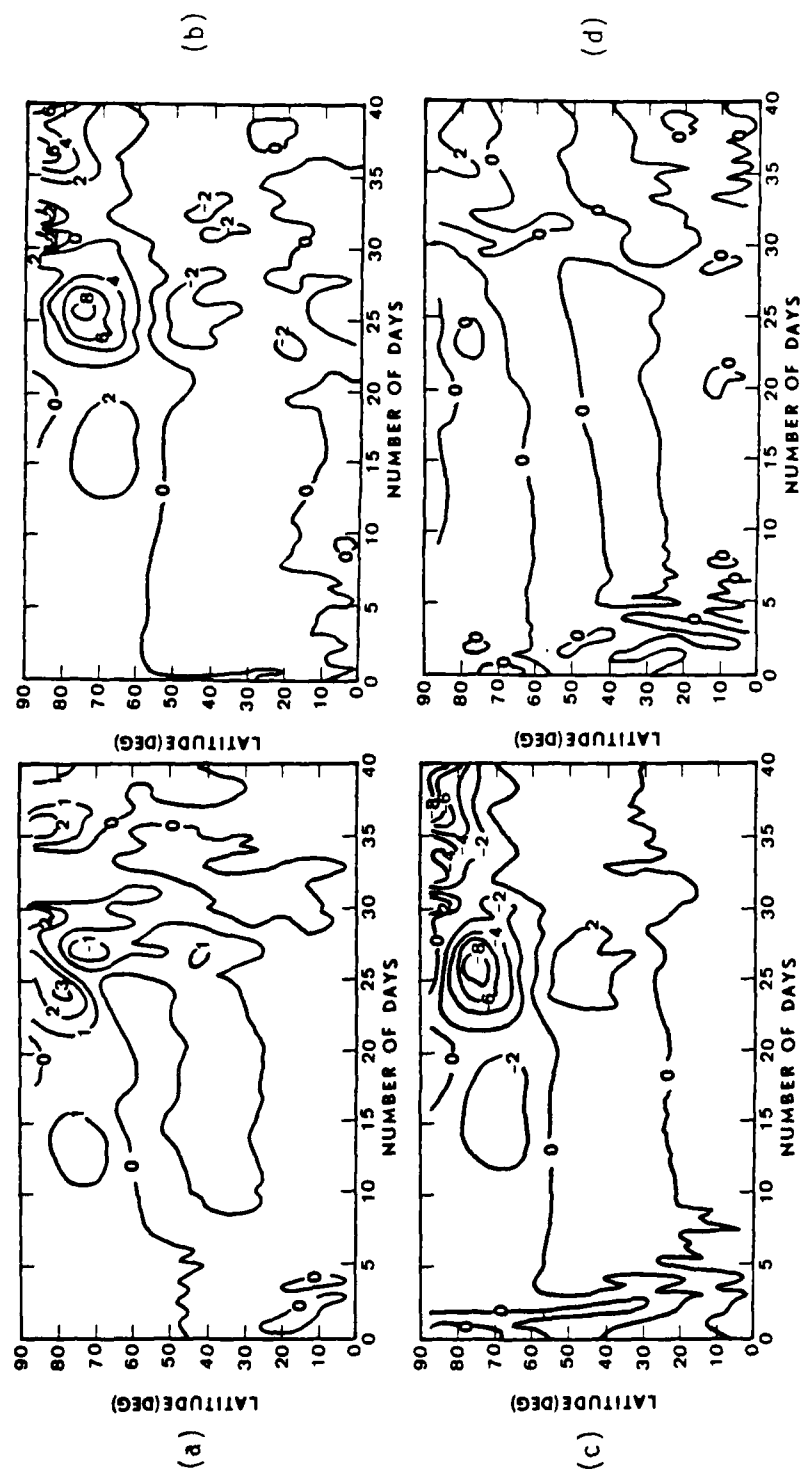
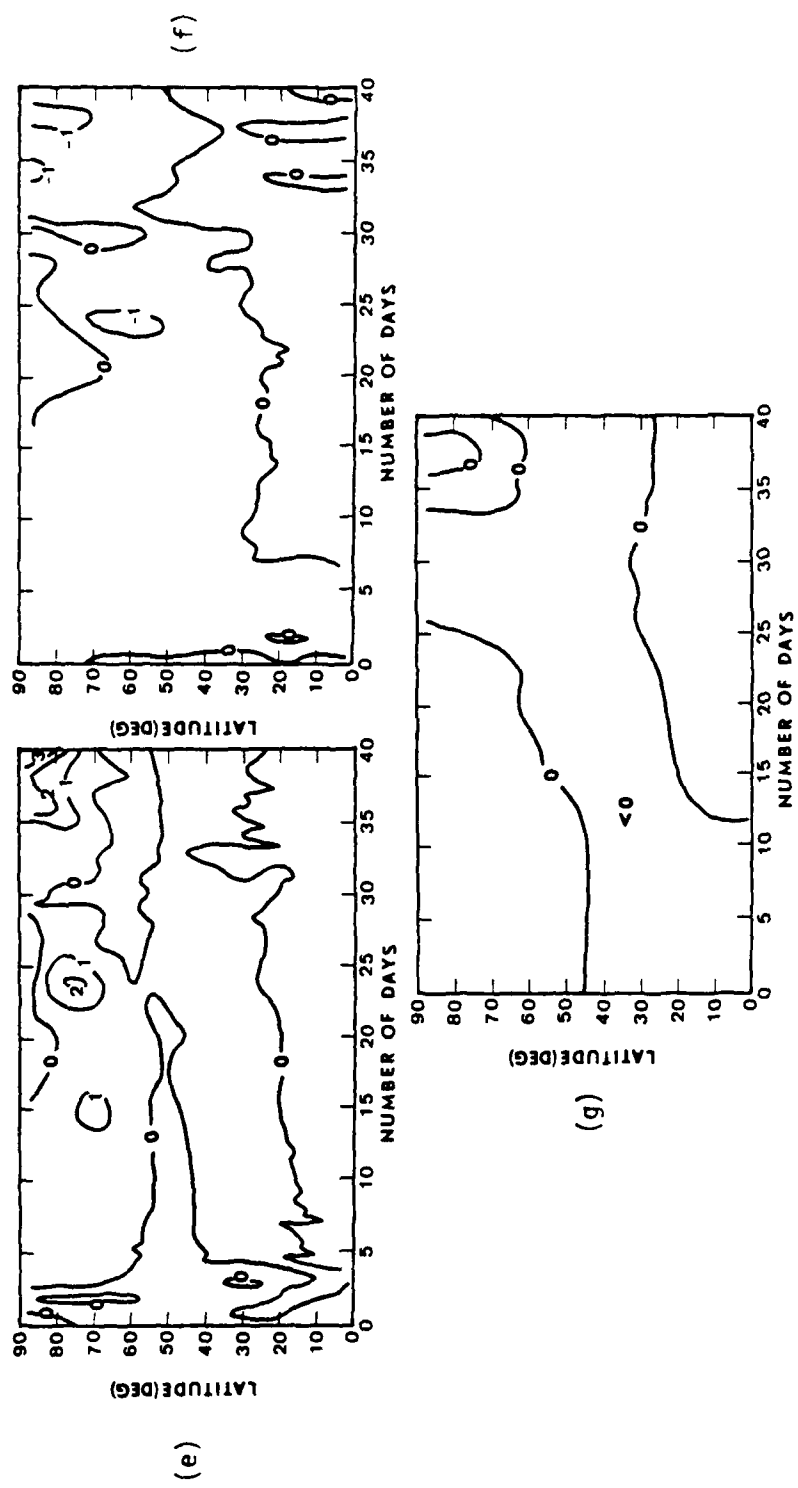


Figure 50. C2 latitude-time sections at 40.5 km of (a) $\partial\bar{T}/\partial t$; (b) VTP; (c) HMB; (d) VTB. Units are $10^{-4} \text{ }^{\circ}\text{K s}^{-1}$.



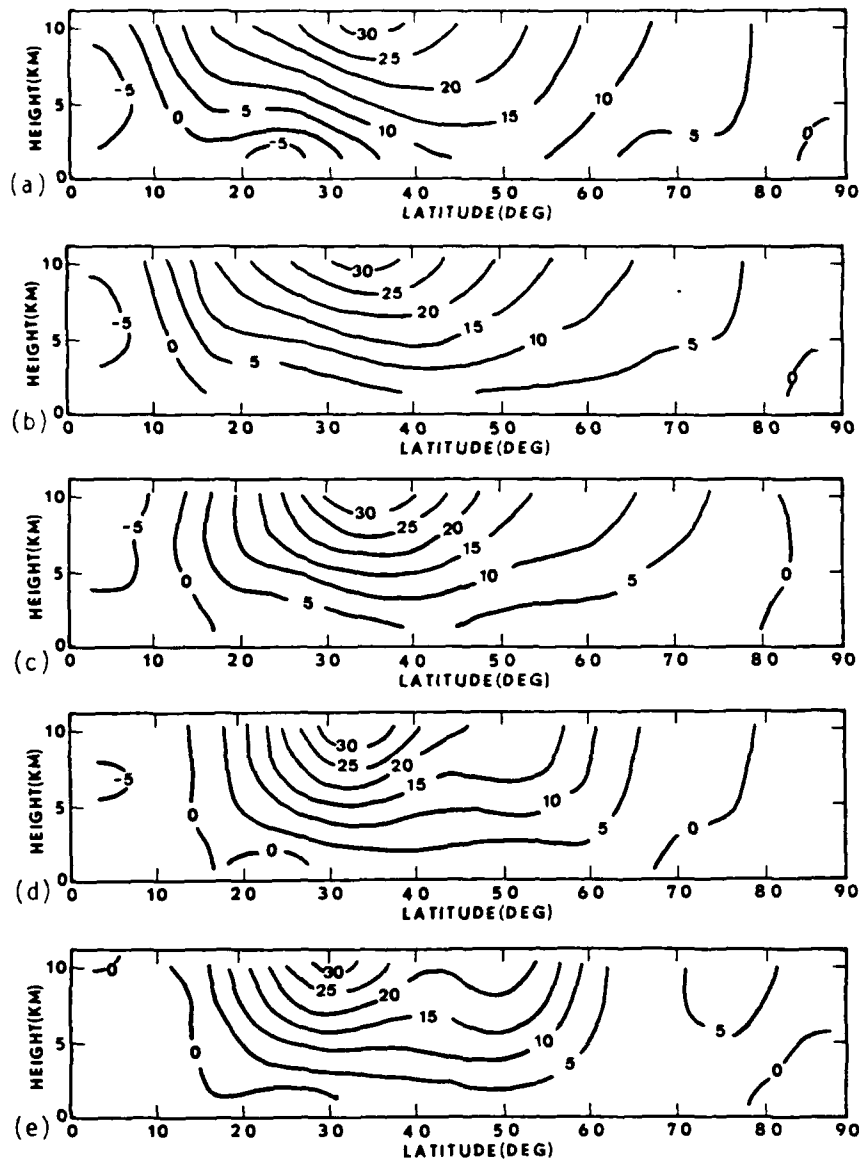


Figure 51. Latitude-height sections of the mean zonal wind ($m s^{-1}$) for C3 on (a) initial time; (b) day 10; (c) day 20; (d) day 30; and (e) day 40.

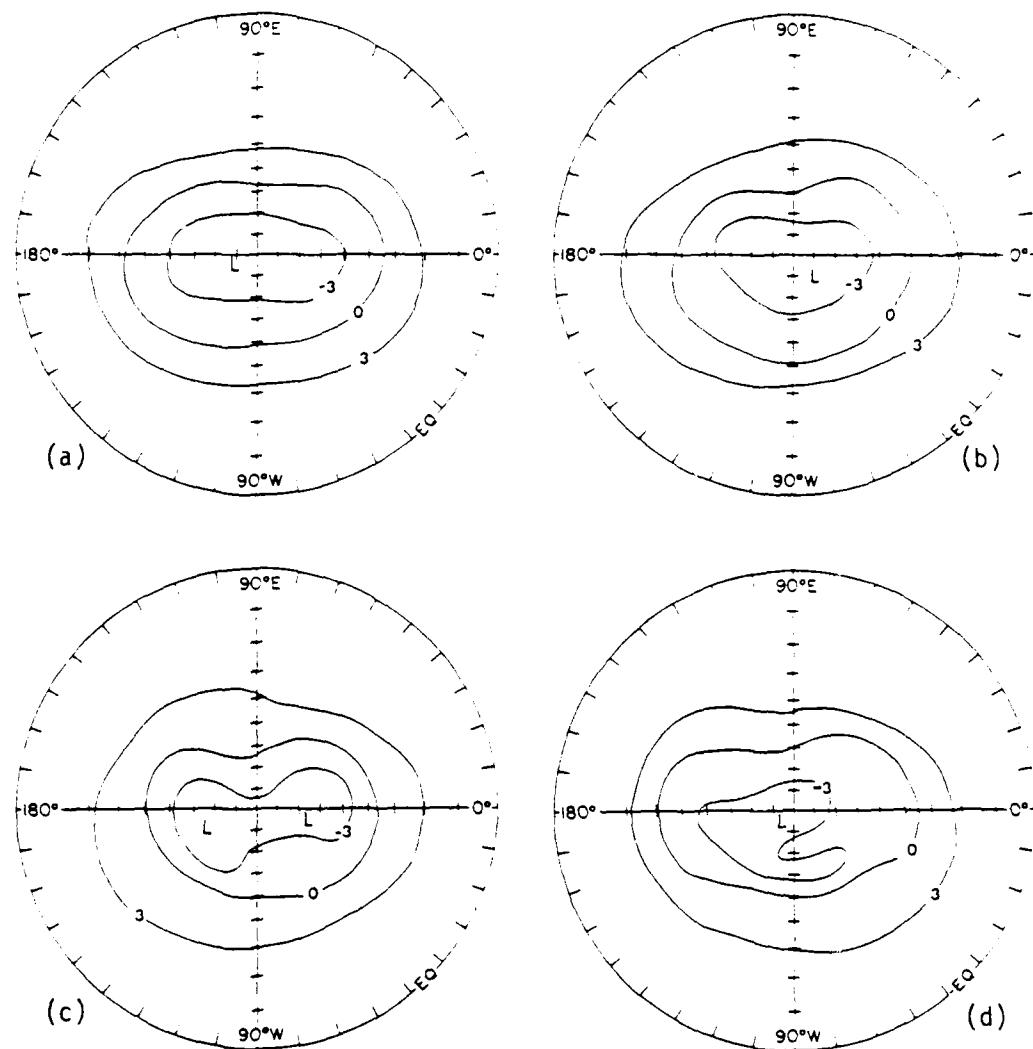


Figure 52. Polar stereographic projections of height deviations ($\times 10^2$ m) at approximately 6.7 km for C3 on (a) day 10; (b) day 20; (c) day 30; and (d) day 40.

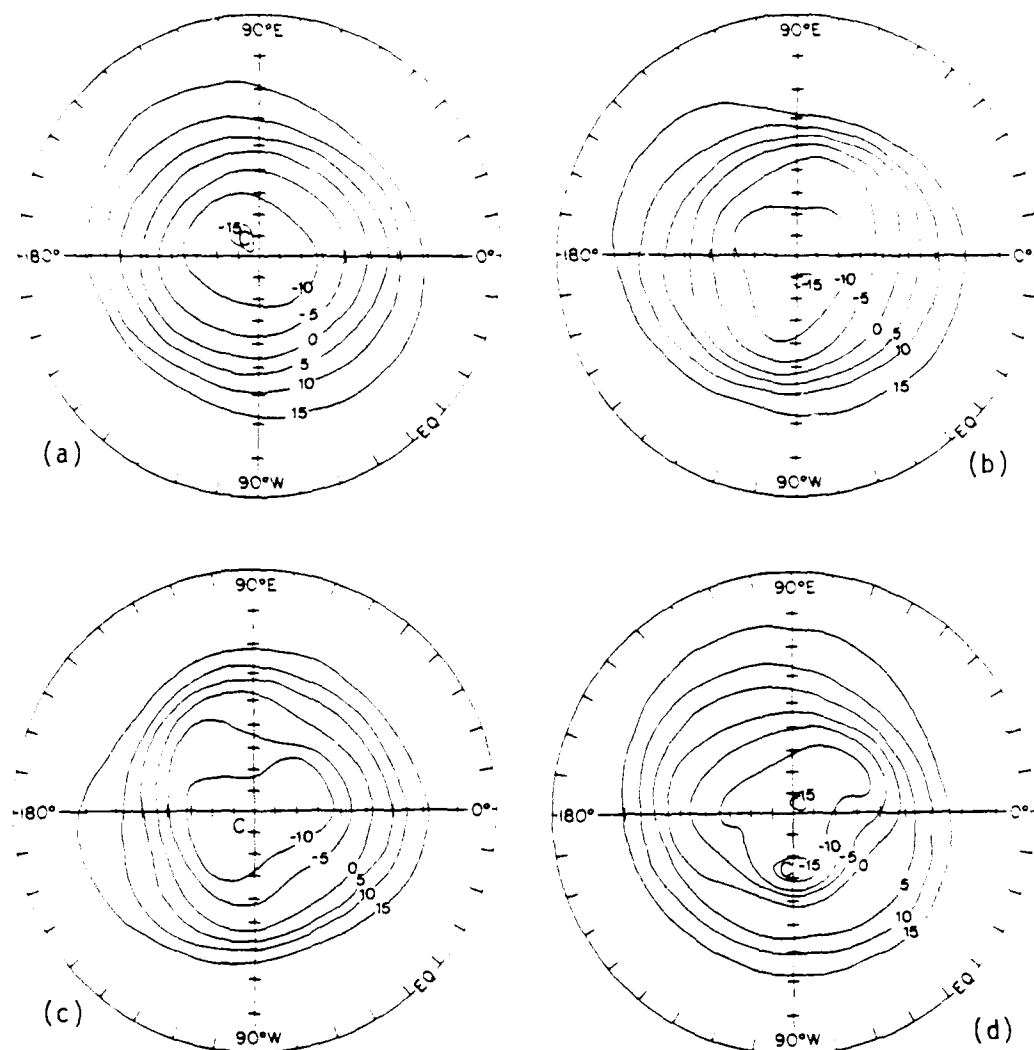


Figure 53. Polar stereographic projections of temperature deviations ($^{\circ}\text{K}$) at approximately 6.7 km for C3 on (a) day 10; (b) day 20; (c) day 30; and (d) day 40.

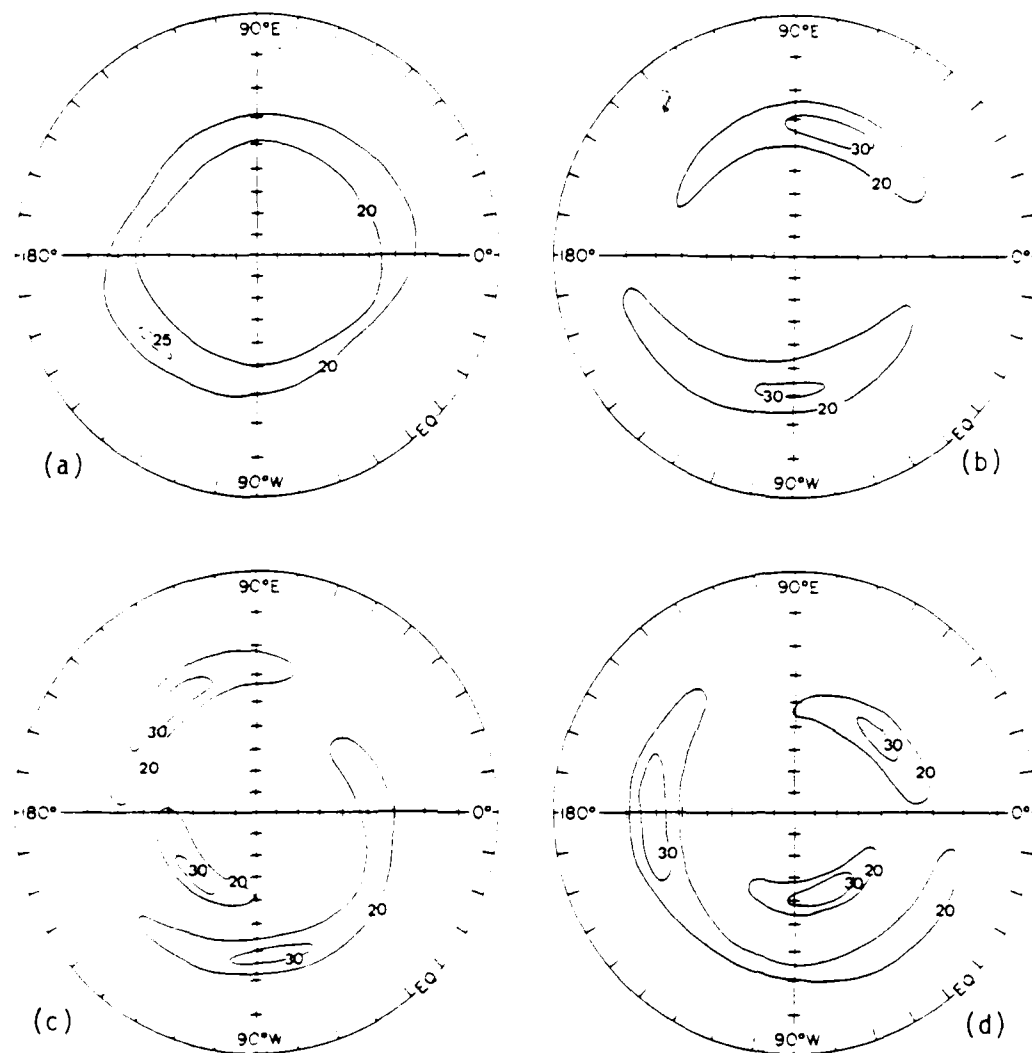


Figure 54. C3 polar stereographic projections of the zonal wind component ($m^{-1} s^{-1}$) for values greater than or equal to $20 m s^{-1}$ on (a) day 10; (b) day 20; (c) day 30; (d) day 40.

AD-A092 420

AIR FORCE INST OF TECH WRIGHT-PATTERSON AFB OH

F/G 4/2

DYNAMIC INTERACTIONS BETWEEN THE TROPOSPHERE AND STRATOSPHERE. (U)

1980

J P KOERMER

UNCLASSIFIED

AFIT-CI-80-31D

NL

3 of 3
29-420



END
DATE
FILED
81-2-
DTIC

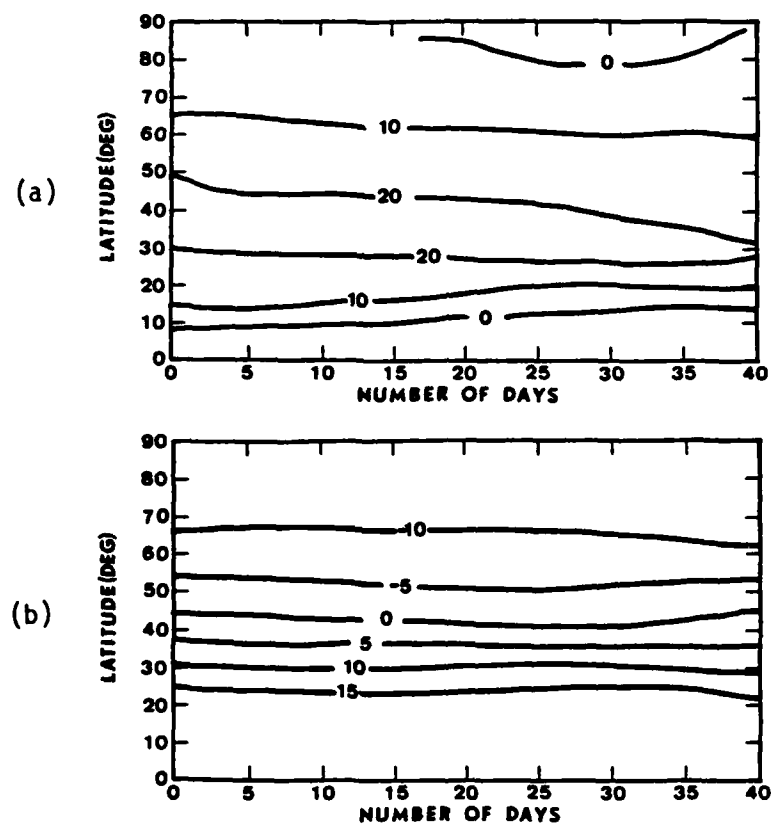


Figure 55. C3 latitude-time sections at 7.5 km of (a) mean zonal velocity (m s^{-1}) and (b) zonal mean temperature deviation ($^{\circ}\text{K}$).

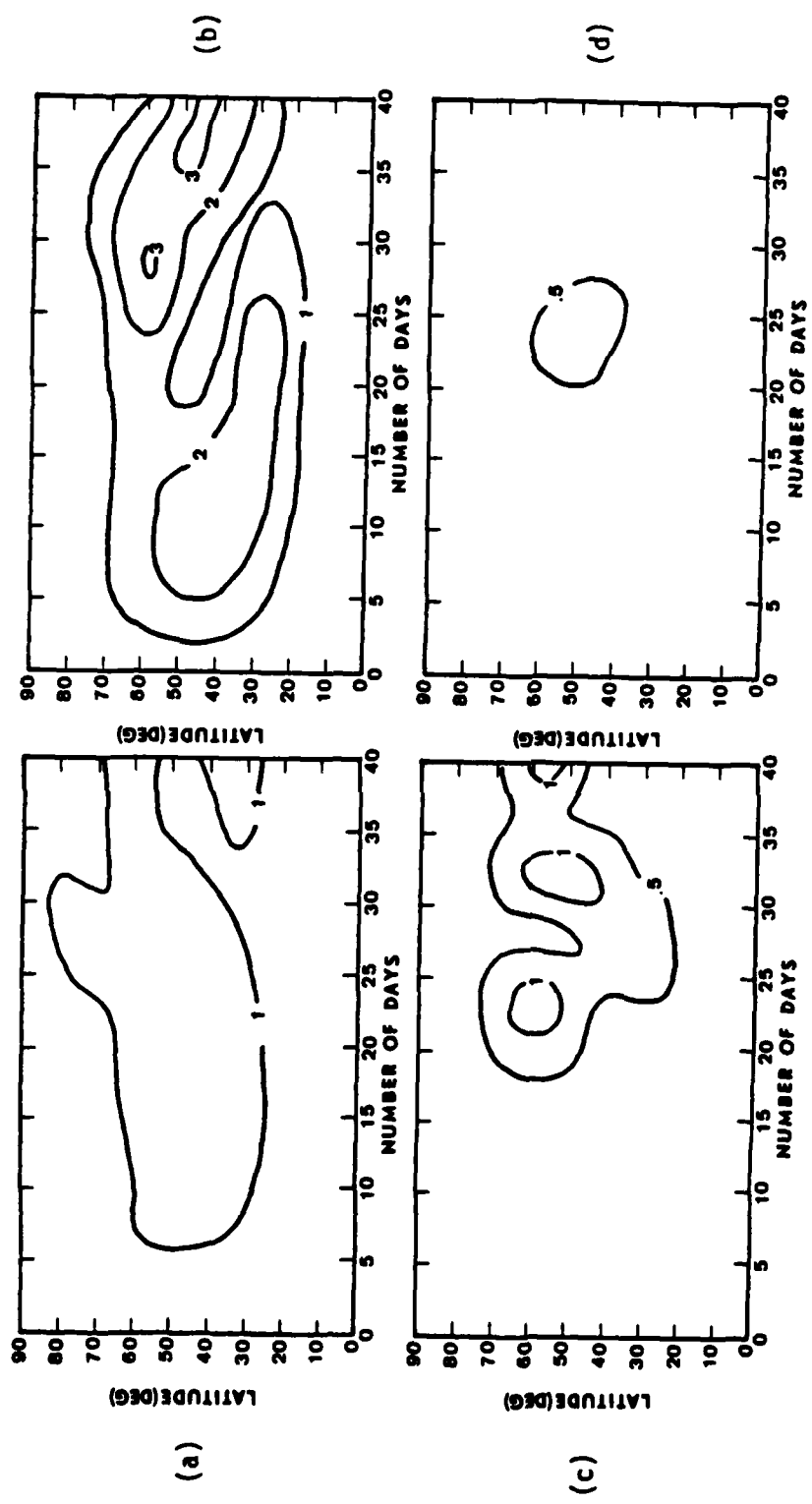


Figure 56. C3 latitude-time sections at 7.5 km of (a) $|\Phi_1|$; (b) $|\Phi_2|$; (c) $|\Phi_3|$; and (d) $|\Phi_4|$.
Units are $10^3 \text{ m}^2 \text{ s}^{-2}$.

REFERENCES

Arakawa, A., and V. R. Lamb, Computational design of the basic dynamical processes of the UCLA general circulation model, Methods in Comp. Phys., 17, 173-265 (1977).

Bourke, W., A multi-level spectral model. I. Formulation and hemispheric integrations, Mon. Wea. Rev., 102, 687-701 (1974).

Bourke, W., B. McAvaney, K. Puri, and R. Thuring, Global modeling of the atmospheric flow by spectral methods, Methods in Comp. Phys., 17, 267-334 (1977).

Charney, J. G., and P. G. Drazin, Propagation of planetary scale disturbances from the lower into the upper atmosphere, J. Geophys. Res., 66, 83-109 (1961).

Corby, G. A., A Gilchrist, and R. Newson, A general circulation model of the atmosphere, suitable for long period integrations, Quart. J. R. Meteorol. Soc., 98, 809-832 (1972).

Craig, R. A., The Upper Atmosphere, Meteorology and Physics (Academic Press, New York, 1965).

Eliassen, A., and E. Palm, On the transfer of energy in stationary mountain waves, Geofysiske Publikasjoner, 12, No. 3, 1-23 (1961).

Haltiner, G. J., Numerical Weather Prediction (John Wiley and Sons, New York, 1971).

Hirota, I., Planetary waves in the upper stratosphere in early 1966, J. Meteorol. Soc. Jap. 6, 418-430 (1968).

Hirota, I., and J. J. Barnett, Planetary waves in the winter mesosphere --Preliminary analysis of Nimbus 6 PMR results, Quart. J. Roy. Meteorol. Soc., 103, 487-498 (1977).

Holton, J. R., The dynamic meteorology of the stratosphere and mesosphere, Meteorol. Mon., No. 37 (1975), 218 pp.

Holton, J. R., A semi-spectral numerical model for wave-mean flow interactions in the stratosphere: application to sudden stratospheric warmings. J. Atmos. Sci., 33, 1639-1649 (1976).

Holton, J. R. and C. Mass, Stratospheric vacillation cycles, J. Atmos. Sci., 33, 2218-2225 (1976).

Holton, J. R., and T. Dunkerton, On the role of wave transience and dissipation in stratospheric mean flow vacillations. J. Atmos. Sci., 35, 740-744 (1978).

Hoskins, B. J., and A. J. Simmons, A multi-layer spectral model and the semi-implicit method. Quart. J. R. Meteorol. Soc., 101, 637-655 (1975).

Houghton, J. T., The stratosphere and mesosphere. Quart. J. R. Meteorol. Soc., 104, 1-29 (1978).

Iwashima, T., Observational studies of ultra-long waves in the atmosphere (II), Part 2, Ultra-long wave energy processes during a sudden warming, J. Meteorol. Soc. Jap., 52, 120-142 (1974).

Julian, P. R., and K. Labitzke, A study of atmospheric energetics during January and February 1963 stratospheric warming. J. Atmos. Sci., 22, 597-610 (1965).

Kasahara, A., Various vertical coordinate systems used for numerical weather prediction, Mon. Wea. Rev., 102, 509-664 (1974).

Kasahara, A., T. Sasamori, and W. M. Washington, Simulation experiments with a 12-layer stratospheric global circulation model. I. Dynamical effect of the earth's orography and thermal influence of continentality. J. Atmos. Sci., 30, 1229-1251 (1973).

Koermer, J. P., and S. K. Kao, Major and minor stratospheric warmings and their interactions on the troposphere. Pure and Appl. Geophys. 118, 428-451 (1980).

Kurihara, Y., On the use of implicit and iterative methods for the time integration of the wave equation, Mon. Wea. Rev., 93, 33-46 (1965).

Kurihara, Y., Note on finite difference expressions for the hydrostatic relation and pressure gradient force. Mon. Wea. Rev., 96, 654-656 (1968).

Labitzke, K., The interaction between stratosphere and mesosphere in winter, J. Atmos. Sci., 29, 1395-1399 (1972).

Labitzke, K., Interannual variability of the winter stratosphere in northern hemisphere, Mon. Wea. Rev., 105, 762-770 (1977).

Labitzke, K., On the different behavior of the zonal harmonic height waves 1 and 2 during the winters 1970/71 and 1971/72, Mon. Wea. Rev., 106, 1704-1713 (1978).

Leith, C. E., Atmospheric predictability and two-dimensional turbulence, J. Atmos. Sci., 28, 145-161 (1971).

Leovy, C. B., Simple models of thermally driven mesospheric circulations, J. Atmos. Sci., 21, 327-341 (1971).

Lordi, N. J., A primitive equation spectral model for the study of stratospheric sudden warmings, Ph.D. Thesis, University of Utah, 1978, unpublished.

Lorenz, E. N., Energy and numerical weather prediction, Tellus, 12, 364-373 (1960).

Matsuno, T., A dynamical model of the stratospheric sudden warming, J. Atmos. Sci., 28, 1479-1494 (1971).

McInturff, R. M., Stratospheric warmings: Synoptic, dynamic and general-circulation aspects. NASA Reference Publication, 1017 (1978), 166 pp.

McIntyre, M. E., Baroclinic instability of an idealized model of the polar night jet, Quart. J. Roy. Meteorol. Soc., 98, 165-174 (1972).

Miller, A. J., and K. W. Johnson, On the interaction between the stratosphere and troposphere during the warming of December 1967-January 1968. Quart. J. Roy. Meteorol. Soc., 96, 24-31 (1970).

Namais, J., Multiple Causes of the North American Abnormal Winter 1976-77, Mon. Wea. Rev., 106, 279-295 (1978).

O'Neill, A., and B. F. Taylor, A study of the major stratospheric warming of 1976/77. Quart. J. Roy. Meteorol. Soc., 105, 71-92.

Oort, A. H., and E. M. Rasmusson, Atmospheric circulation statistics. NOAA Professional Paper 5, U. S. Department of Commerce/National Oceanic and Atmospheric Administration (Rockville, Maryland, 1971). 323 pp.

Perry, J. S., Long wave energy processes in the 1963 sudden stratospheric warming. J. Atmos. Sci., 24, 537-550 (1967).

Phillips, N. A., A coordinate system having some special advantages for numerical forecasting. J. Meteor., 14, 184-185 (1957).

Puri, K., and W. Bourke, Implications of horizontal resolution in spectral model integrations, Mon. Wea. Rev., 102, 333-347 (1974).

Quiroz, R. S., The warming of the upper stratosphere in February 1966 and the associated structure of the mesosphere, Mon. Wea. Rev., 97, 541-552 (1969).

Quiroz, R. S., The determination of the amplitude and altitude of stratospheric warmings from satellite-measured radiance changes, J. Appl. Meteorol., 10, 555-574, (1971).

Quiroz, R. S., The tropospheric-stratospheric polar vortex breakdown of January 1977, Geophys. Res. Lett., 4, 151-154 (1977).

Quiroz, R. S., A. J. Miller, and R. M. Nagatani, A comparison of observed and simulated properties of sudden stratospheric warmings, J. Atmos. Sci., 32, 1723-1736 (1975).

Robert, A. J., Integration of a spectral model of the atmosphere by the implicit method. Proceedings of the WMO/IUGG Symposium on Numerical Weather Prediction, Tokyo, Japan, November 26 - December 4, 1968, 719-724 (1969).

Robert, A. J., J. Henderson, and C. Turnbull, An implicit time integration scheme for baroclinic modes of the atmosphere, Mon. Wea. Rev., 100, 329-335 (1972).

Schoeberl, M. R., Stratospheric warmings: observation and theory, Rev. of Geophys. and Space Phys., 16, 521-538 (1978).

Schoeberl, M. R., and D. F. Strobel, Numerical simulations of sudden stratospheric warmings, J. Atmos. Sci., 37, 214-236 (1980a).

Schoeberl, M. R., and D. F. Strobel, Sudden stratospheric warmings forced by mountains, Geophys. Res. Lett., 7, 149-152 (1980b).

Shapiro, R., The use of linear filtering as a parameterization of atmospheric diffusion, J. Atmos. Sci., 28, 523-531 (1971).

Scherhag, R., Die explosionsartige Stratosphärenwärme des Spätwinters 1951/52, Ber. Deut. Wetterdienstes, 6, 51-53 (1952).

Sommerville, R. C., Predictability and prediction of ultra-long planetary waves. Fourth Conference on Numerical Weather Prediction of the American Meteorological Society, October 29 - November 1, 1979, Silver Springs, Maryland, 1979.

Taylor, B. F., and J. D. Perry, The major stratospheric warming of 1976-1977, Nature, 267, 417-418 (1977).

Teweles, S., and F. G. Finger, An abrupt change in stratospheric circulation beginning in mid-January 1958, Mon. Wea. Rev., 86, 23-28 (1958).

Trenberth, K. E., Dynamical coupling of the stratosphere with the troposphere and sudden warmings, Mon. Wea. Rev., 101, 306-322 (1973).

van Loon, H., and R. L. Jenne, The zonal harmonic standing waves in the southern hemisphere, J. Geophys. Res., 77, 992-1003 (1972).

van Loon, H., R. L. Jenne, and K. Labitzke, Zonal harmonic standing waves, J. Geophys. Res., 78, 4463-4471 (1973).

Wagner, A. J., Weather and circulation of January 1977--The coldest month on record in the Ohio valley, Mon. Wea. Rev., 105, 553-560 (1977).

VITA

Name	James Paul Koerner
Birthplace	Baltimore, Maryland
Birthdate	July 22, 1947
High School	Loyola High School Towson, Maryland
Universities	University of Maryland College Park, Maryland 1964-1968
	University of Texas Austin, Texas 1968-1969
	University of Utah Salt Lake City, Utah 1971-1973; 1977-1980
Degrees	B.S. 1968, University of Maryland College Park, Maryland
	M.S. 1973, University of Utah Salt Lake City, Utah
Publications	"The Nonlinear Behavior of Atmospheric Kelvin Waves," 1974 (with V. E. Kousky), <u>J. Atmos. Sci.</u> , <u>31</u> , 1777-1783. "Major and Minor Stratospheric Warnings and their Interactions on the Troposphere," 1980 (with S. K. Kao), <u>Pure and Appl.</u> <u>Geophys.</u> , <u>118</u> , 428-451.

